Doctoral dissertation

The fundamental research on polyether-based materials for application to the next-generation secondary battery

(次世代二次電池材料へのポリエーテル誘導体の応用に向けた基礎的研究)

March 2023

Koki Yamada

Graduate School of Sciences and Technology for Innovation

Yamaguchi University

The fundamental research on polyether-based materials for application to the next-generation secondary battery

(次世代二次電池材料へのポリエーテル誘導体の応用に向けた基礎的研究)

Koki Yamada

Department of Applied Chemistry

Graduate School of Sciences and Technology for Innovation

Yamaguchi University

Ube, Japan

2023

Contents

YAMAGUCHI
UNIVERSITY

General introduction

Research background

1. Li-ion batteries

Secondary batteries, such as alkaline, Ni–Cd, lead acid, and Li-ion batteries (LIBs), are essential as energy storage devices. In particular, LIBs have the highest working voltages (~3.6 V) compared to other batteries (ranging from 1.2 to 2.0 V), higher gravimetric specific energy (~240 Wh/kg) compared to lead acid batteries (~40 Wh/kg), minimal memory effects, and fast charging.[1,2] Since LIBs were first commercialized in 1990 by SONY corporation, they have been widely used in electric devices, such as phones, laptops, and pacemakers. In addition, their use in electric vehicles (EV) and hybrid electric vehicles (HEV), which require massive amounts of energy, has attracted considerable research attention.

The replacement of gasoline-powered vehicles with EVs has aided in satisfying the demands of sustainable development goals, which are aimed at achieving a sustainable society, via the reduction of greenhouse gas emissions. Furthermore, LIBs demonstrate prospects for the storage of electricity sourced from renewable energy sources, such as solar and wind-power. These energy storage devices may be a solution for energy shortages that occur in the afternoon owing to the hourly electricity load during daytime.

Typically, LIBs mainly consist of four components: an anode, a cathode, a separator, and an electrolyte (**Figure 1**). During the charging process, Li^+ and an electron (e^-) move from the cathode to the anode through the electrolyte and are intercalated into layered graphite.[3,4] The discharging process is the inverse of the charging process. Because Li is present as an ion

during both the charging and discharging processes in the battery, it is called an LIB and can be distinguished from Li-metal batteries.

$$(-)\ xLi^{+} + xe^{-} + 6C \rightarrow Li_xC_6$$

$$(+)\ LiCoO_2 \rightarrow Li1{-}xCoO_2 + xLi^{+} + xe^{-}$$

Recently, carbon materials such as graphite have been used as active materials for the anode owing to their low working potentials (0.25 V_{Li}).[5] By contrast, transition metal oxides have been mainly employed as the cathode, and herein, $LiCoO_2$,[6] $LiMn_2O_4$,[7] and $LiFePO_4$[8] are the most commonly used materials.

The most widely used electrolytes comprise a mixture of an organic solvent and Li salt; for instance, they may contain ethylene carbonate (EC) or dimethyl carbonate (DMC) as the organic solvent and $LiPF_6$ as the Li salt.[9] Polyolefin films are used as separators to prevent direct contact between the two electrodes, which is known as an internal short-circuit.[10]

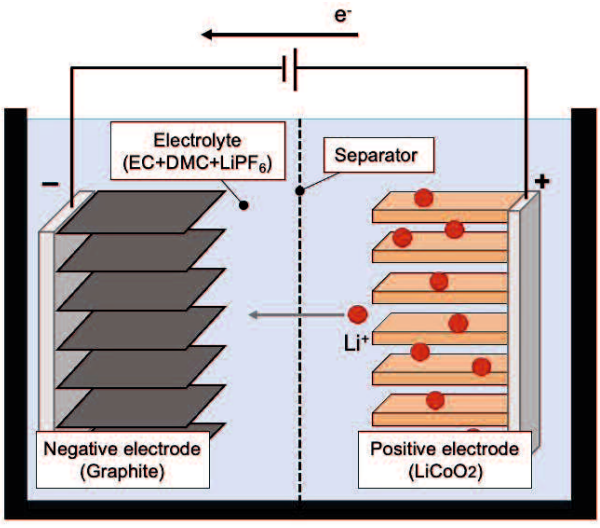

Figure 1. Schematic of the working principle of an LIB during the charging process.

2. Roadblocks in the realization of better LIBs (1)

2.1 Safety concerns associated with LIBs

One of the most significant problems associated with LIBs is their safety concern, i.e., fires and explosions. The number of accidents caused by LIBs has recently increased owing to the thermal runaway of LIBs (**Figure 2**).[11,12] The fire and explosion risks of LIBs can often be attributed to the use of flammable organic electrolytes, the rate of charge and discharge, and failure of battery packaging.[10,13] The foregoing risks may lead to catastrophic accidents when LIBs are used in large-scale devices, such as EVs and HEVs. In particular, the thermal runaway of LIBs occurs when the internal reaction is out of control; this increases the cell temperature and accelerates the reaction, which further increases the cell temperature and may result in potential cell explosions.[14,15] Such thermal runaway can occur at >80 °C owing to the break-up of solid electrolyte interphase (SEI) films.[16] To suppress the overheating of batteries, current LIBs have a self-clogging polyolefin separator, which melts at ~130 °C.[17,18] Typically, commonly used cathode materials can be broken down and can emit oxygen gas, which cause of both the electrolyte and other gases in the battery. In particular, charged cathode active materials can breakdown at elevated temperatures; for example, an $LiCoO_2$ electrode may breakdown as described below.[19,20,21] The involved reaction emits a large amount of heat, reaching ~1000 J g^{-1} based on the cathode weight.[22] This reaction occurs at ~120 °C and increases the cell temperature up to 230 °C. Furthermore, the liberated oxygen gas further reacts with the solvent, such as EC, as follows:[12,23]

$$Li_xCoO_2 \rightarrow xLiCoO_2 + 1/3\ (1-x)Co_3O_4 + 1/3\ (1-x)\ O_2$$

$$Co_3O_4 \rightarrow 3CoO + 1/2O_2$$

$$2.5O_2 + C_3H_4O_3\ (EC) \rightarrow 3CO_2 + 2H_2O$$

Under these circumstances, several researchers have devoted considerable efforts to reduce the danger of fire and explosions by devising various strategies, such as using flame retardant additives in the electrolyte,[24,25] coating the cathode with non-reactive materials,[26,27] and modifying the anode surface via mid oxidation or polymer coating.[28,29] However, a completely safe electrolyte containing an organic solvent is yet to be discovered. Thus, the most reliable material for the safe operation of LIBs is a solid based electrolyte.

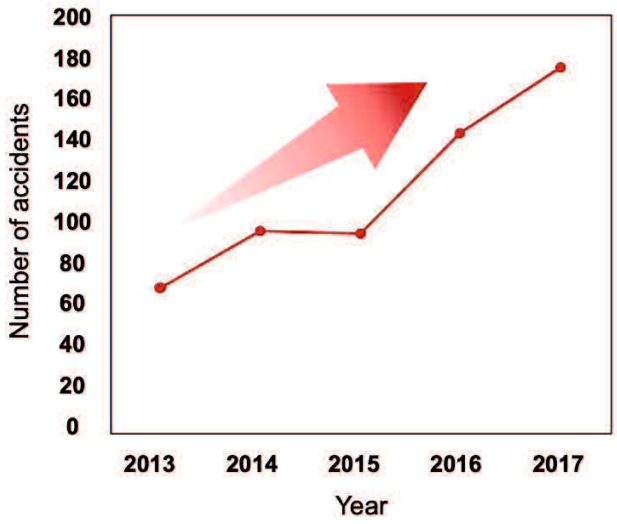

Figure 2. Number of accidents caused by LIBs used in mobile devices reported over the past few years.

3. Roadblocks in the realization of better LIBs (2)

3.1 Electrochemical reaction at the electrode/electrolyte interface

Notably, recent studies on LIBs have focused on understanding and controlling the electrochemical reaction occurring at the electrode/electrolyte interface. Here, one of the most important interfacial reactions is the formation of an SEI film on the anode. Dey *et al*. first reported the formation of a passivation layer on Li in an organic electrolyte in 1970,[30] which was followed by the SEI concept proposed by Peled *et al*.[31] In LIBs, the SEI film formed during the first charging process is the result of a reduction reaction involving the solvent, anion, and impurities, which provide an electrically insulating and ionically conductive interface (the SEI image is shown in **Figure 3**).[32] The formation of the SEI layer occurs when the redox potential of the electrode used in the electrolyte exceeds the electrochemical window of the electrolyte itself, which is shown schematically in **Figure 4**.[13] When the lowest unoccupied molecular orbital (LUMO) of the electrolyte is lower than the Fermi energy level of the anode, the electrolyte can be reduced. As the LUMOs of most organic solvents lie beyond the Fermi energy level of graphite, organic solvents are reduced to form the SEI layer and passivate the graphite surface. On the contrary, if the highest occupied molecular orbital of the electrolyte is higher than the Fermi energy level of the cathode, the electrolyte can be expected to undergo oxidation. In this scenario, the resulting decomposition products settle on the cathode and create an interface known as the cathode–electrolyte interphase (CEI). An ideal SEI hinders further degradation reactions of the electrolyte, such as the Li-ion consuming reaction.[33,34] Therefore, the SEI is considered a key

factor in improving battery performance not only in terms of its safety but also in terms of other crucial properties, such as the capacity and cycle life.[35,36]

Owing to the importance of the components and surface morphology of the SEI to the battery performance, significant research efforts have been devoted toward the analysis of the SEI formed at the anode/conventional organic electrolyte (such as EC, DMC, and EMC) interface. Correspondingly, various techniques have been used to analyze the SEI components; these include X-ray photoelectron spectroscopy (XPS), nuclear magnetic (NMR) spectroscopy, Fourier transform infrared (FT-IR) spectroscopy, and gas chromatography. The corresponding results reveal that the SEI is composed of mosaic structures, such as Li alkyl carbonate, ROLi, Li_2CO_3, and LiF, with a thickness of several tens of nanometers.[37,38, 39,40,41]

3.2 Electrode/solid polymer electrolyte interface

The reaction occurring at the electrode/electrolyte interface in solid polymer electrolytes (SPEs), which are an alternative to conventional organic electrolytes owing to their higher electrochemical stability and non-flammability, is also important for battery performance. The details of SPEs will be discussed in the following section. Some research efforts have also been dedicated to reveal the morphology and components of the SEI at the anode/SPE interface. Peled *et al*. confirmed the formation of an SEI layer on the Li surface in a PEO-based composite electrolyte using electrochemical impedance spectroscopy (EIS); and this was found to be stable at 120 °C.[42] Their subsequent research revealed that the SEI resistance approaches the range of 10 to 100 Ω cm^{-2} at 30 °C.[43] Kong *et al*. performed ellipsometry measurements on an Li/PEO–LiTFSA interface, which detected a resistive SEI with a

thickness of ~12 nm prior to cycling and ~37 nm after the discharging process.[44] One of the most widely used methods to reveal the components of the SEI in SPEs is ex-situ XPS owing to its high surface sensitivity. Several studies using ex-situ XPS have detected the components of the SEI formed on the anode surface; these include Li_2O, LiF, and LiOH, which are produced by the reduction of the Li salt and impurities.

However, ex-situ measurements cannot detect the soluble species and intermediates on the electrode surface, limiting their precise characterization and our understanding of the SEI formation mechanism.

Operando measurements are ideal to probe the reactions occurring at the electrode surface during operation. In particular, *operando* attenuated total reflection–infrared (ATR–IR) measurements have been considered effective for the analysis of surface reactions owing to their high sensitivity toward covalent bonds and the inherent non-destructive character of infrared irradiation, which enables one to capture the degradation of the electrolyte within the vicinity of the electrode.[45,46] Scherson *et al*. detected some reduction products, such as ROLi, during the cathodic process on an Au/PEO-based electrolyte surface using *operando* ATR–IR measurements.[47,48] However, the reduction mechanism of PEO on the electrode still remains unclear.

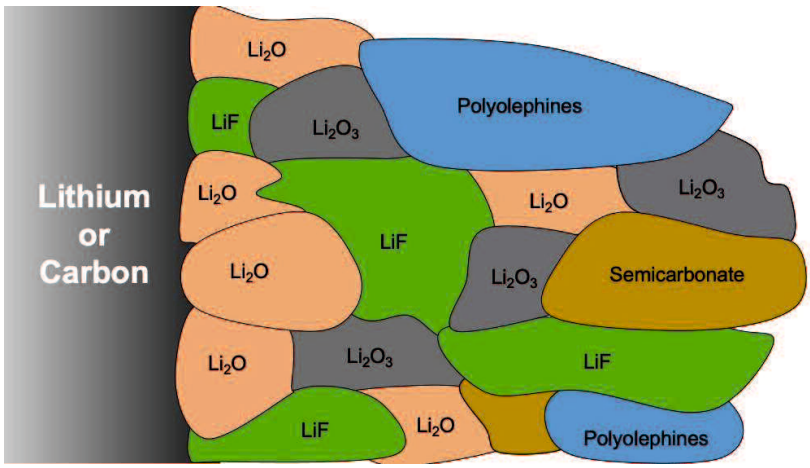

Figure 3. Schematic of the SEI formed on the anode (Li or carbon) surface in an organic electrolyte.[32]

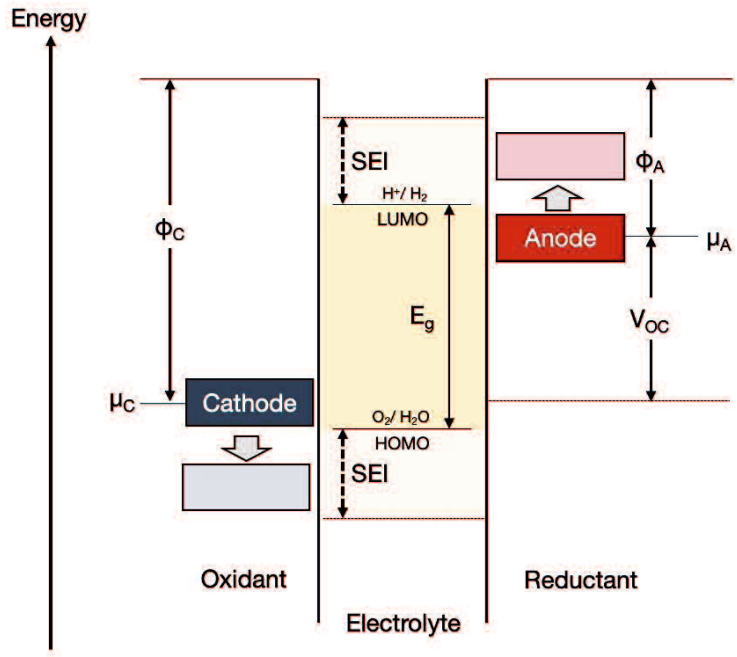

Figure 4. Schematic of the energy diagram of an electrolyte. Here, ΦA, ΦC, E_g, μ_A, and μ_C denote the anode and cathode work functions, the electrolyte's electrochemical stability window, and the redox potential of the anode and cathode, respectively.[13]

4. Roadblocks in the realization of better LIBs (3)

4.1 Insufficient energy density for EVs

For better performing secondary batteries, several approaches can be adopted to improve the battery performance, particularly in terms of the energy density and specific energy. Although LIBs have relatively high energy densities when compared to conventional lead acid, Ni–MH, and Ni–Cd batteries, their energy densities are not sufficient to cover long-driving distances, as shown in **Figure 5**.[49] **Figure 6** presents the energy densities of various next-generation batteries.[2,50]

Figures 5 and **6** indicate the need for the development of next-generation secondary batteries with high energy densities.

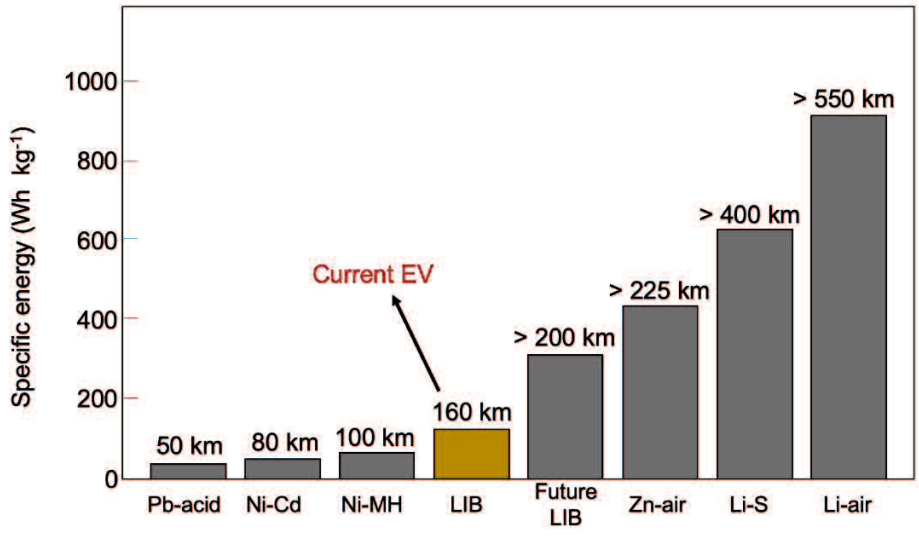

Figure 5. Comparison of the specific energies of several batteries in terms of the estimated driving distance of an EV.

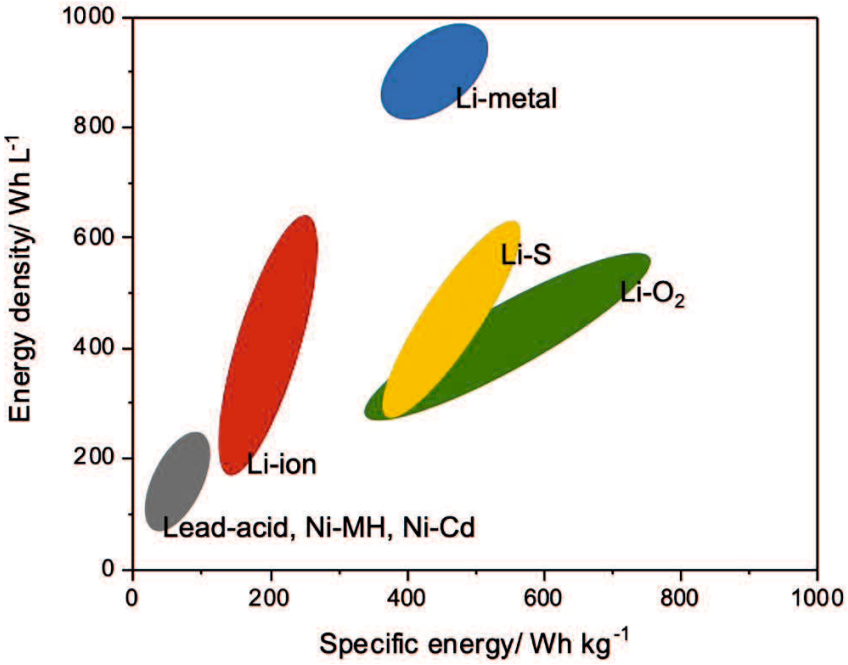

Figure 6. Comparison between different battery types in terms of their volumetric and gravimetric energy densities.

5. Next-generation secondary batteries (beyond LIBs)

5.1 Li–air (Li–O_2) batteries

Typically, Li-O_2 batteries consist of an Li-metal anode and catalyst (for the electrochemical reduction of the active material under a flow of oxygen) with porous carbon, as shown in **Figure 7**. Oxygen is electrochemically reduced to LiO_2 and Li_2O_2 via the cathodic reaction in a non-aqueous electrolyte, which proceeds via the following reactions. Considering the mass of Li, Li-O_2 batteries have an exceptionally high energy density of 11586 Wh kg^{-1}.

$$O_2 + e^- \rightarrow O_2^-$$

$$O_2^- + Li^+ \rightarrow LiO_2$$

$$2LiO_2 \rightarrow Li_2O_2 + O_2$$

However, the applications of Li-O_2 batteries encounter several challenges (**Figure 8**): (i) The unexpected reduction reaction of CO_2 and H_2O in ambient air on the cathode, resulting in the formation of Li_2CO_3 and LiOH instead of Li_2O_2, and (ii) the degradation of the electrolyte components, such as propylene carbonate in the presence of O_2, forming ($C_3H_6(OCO_2Li)_2$), Li_2CO_3, HCO_2Li, CH_3CO_2Li, CO_2, and H_2O.[51] These challenges prevent the commercialization of Li-O_2 batteries with organic carbonate electrolytes and sustainable cycling (up to 100 cycles) performance.[52] In this context, the design of Li-O_2 batteries is primarily focused on the following aspects: (i) covering the outer surface of the cathode to block CO_2 and H_2O[53] and (ii) designing a stable electrolyte to ensure the solubility and diffusion of O_2 while avoiding evaporation at the cathode.[54 55,56]

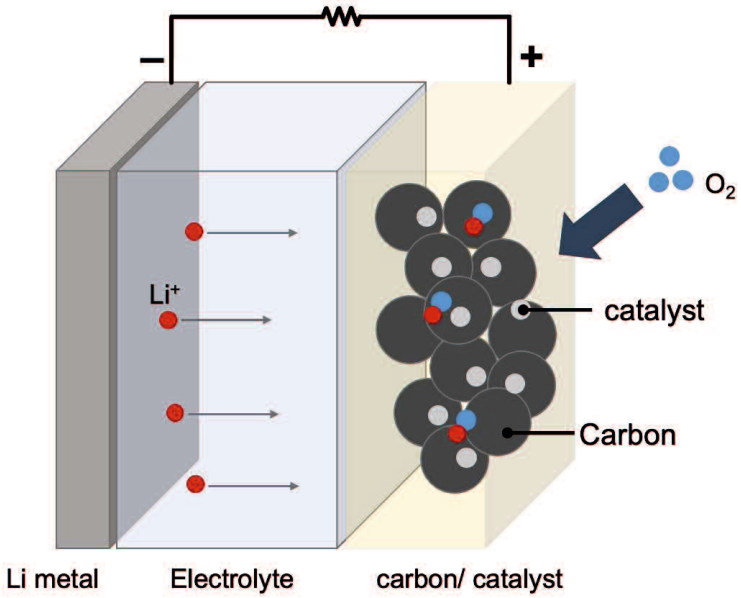

Figure 7. Schematic of the working principle of Li-O_2 batteries during the discharge process.

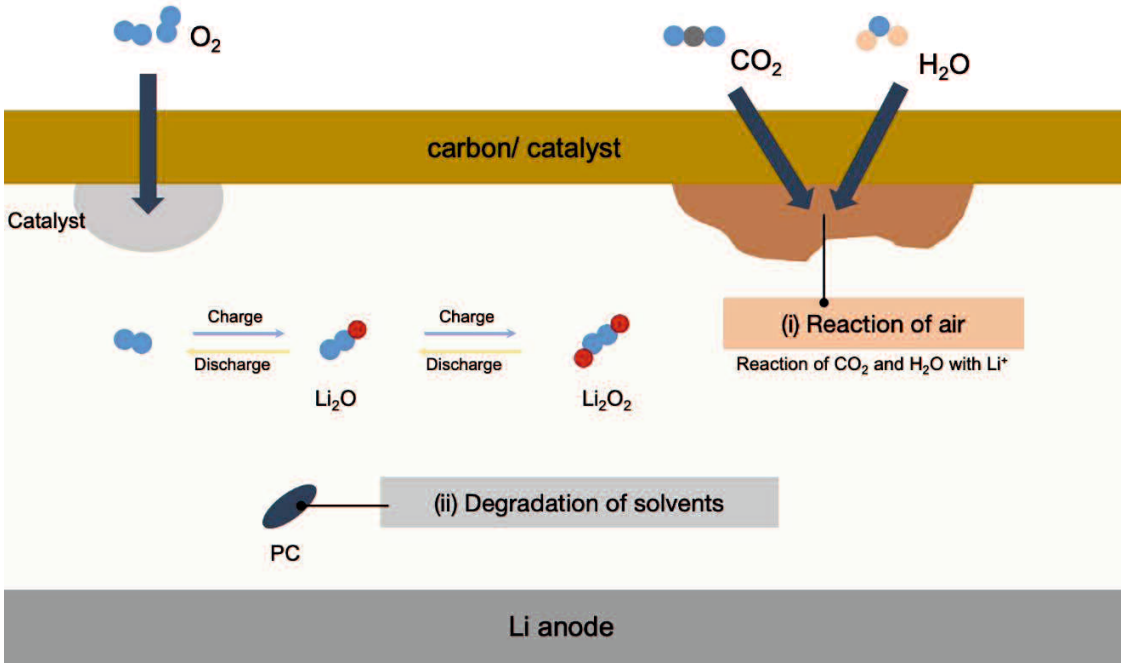

Figure 8. Schematic of the challenges associated with Li-O_2 batteries during the charge/discharge process.

5.2 Li–sulfide (Li–S) batteries

Li-S batteries are composed of an Li anode and porous carbon-based cathode containing S_8, as shown in **Figure 9**. Li-S batteries present several advantages owing to the abundance of sulfide in nature and their exceptionally high theorical energy density. These features of Li-S batteries are necessary for manufacturing inexpensive and long-driving distance EVs. During Li-S battery operation, S_8 undergoes multiple electrochemical reactions as follows:[57]

$S_8 + 2Li^+ + 2e^- \rightleftarrows Li_2S_8$ > 2.3 V vs. Li/Li^+

$Li_2S_8 + 2Li^+ + 2e^- \rightleftarrows 4Li_2S_6$ > 2.3 V vs. Li/Li^+

$Li_2S_6 + 2Li^+ + 2e^- \rightleftarrows 3Li_2S_4$ 2.3 V to 2.1 V vs. Li/Li^+

$Li_2S_4 + 2Li^+ + 2e^- \rightleftarrows 2Li_2S_2$ 2.1 V to 1.9 V vs. Li/Li^+

$Li_2S_4 + 6Li^+ + 6e^- \rightleftarrows 4Li_2S_2$ 2.1 V to 1.9 V vs. Li/Li^+

$Li_2S_2 + 2Li^+ + 2e^- \rightleftarrows 2Li_2S$ < 1.9 V vs. Li/Li^+

In the entire reaction during the charging process, 16 electrons can be obtained, which contribute to the high theorical capacity (1675 mAh g^{-1}). Despite their great potential as alternatives to LIBs, Li-S batteries have yet to be commercialized as power sources for EVs. This is because several problems still remain unresolved, as shown in **Figure 10**. For example, (i) the low-rate capability and poor rechargeability resulting from the low electronic conductivity of S_8, Li_2S, and Li_2S_2, (ii) capacity fading during initial cycles owing to the high solubility of the polysulfide intermediates in the electrolyte, and (iii) the uncontrolled reaction of polysulphide intermediates.[58,59,60] Typically, electrochemically reduced polysulphides at the cathode are transported to the Li anode, after which they are reduced to shorter polysulphides at the Li anode and reoxidized on the cathode, which is known as the redox shuttle; on the anode surface, if the polysulphides are reduced to Li_2S and Li_2S_2 on the Li anode or elsewhere during the redox shuttle, these compounds with low electronic conductivity lead to a highly resistive surface, and (iv) the significant volume change of sulfur during the charge/discharge process causes the destruction of the electrode and low capacity, which is a significant problem.[61,62,63,64]

Extensive efforts have been dedicated to solve the above-mentioned issues associated with Li-S batteries; these involve using a solid electrolyte or ionic liquid electrolyte[65,66,67,68] and designing new carbon materials. In particular, the use of porous carbon materials is considered the most efficient method owing to the high electric conductivities[64] and large surface areas of such materials. Various carbon materials, including carbon nanotubes,[69] mesoporous carbon,[70,71] graphene,[63,72] and hollow carbon,[73] exhibit high specific capacities of >1000 mAh g^{-1}. However, maintaining the high initial discharge capacity remains a pivotal challenge for such carbon materials. An ideal carbon material that not only has a large surface area but also presents tolerance to the volume expansion of sulfur during the charge/discharge process to achieve excellent cycle life has not been found to date.

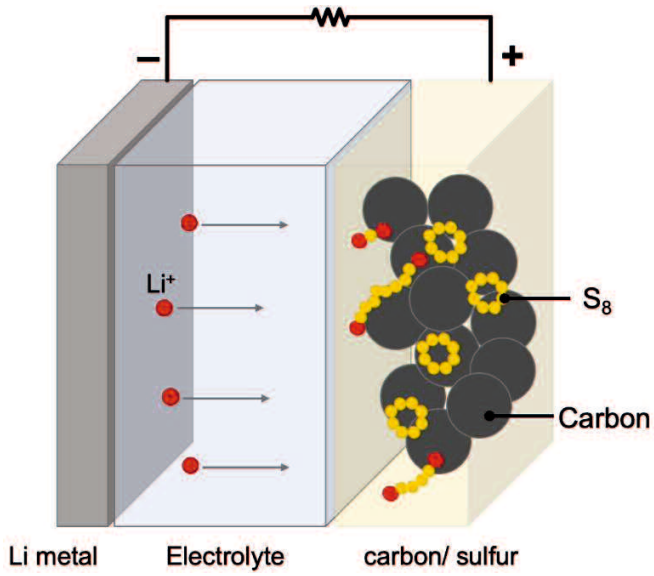

Figure 9. Schematic of the working principle of Li-S batteries during the discharging process.

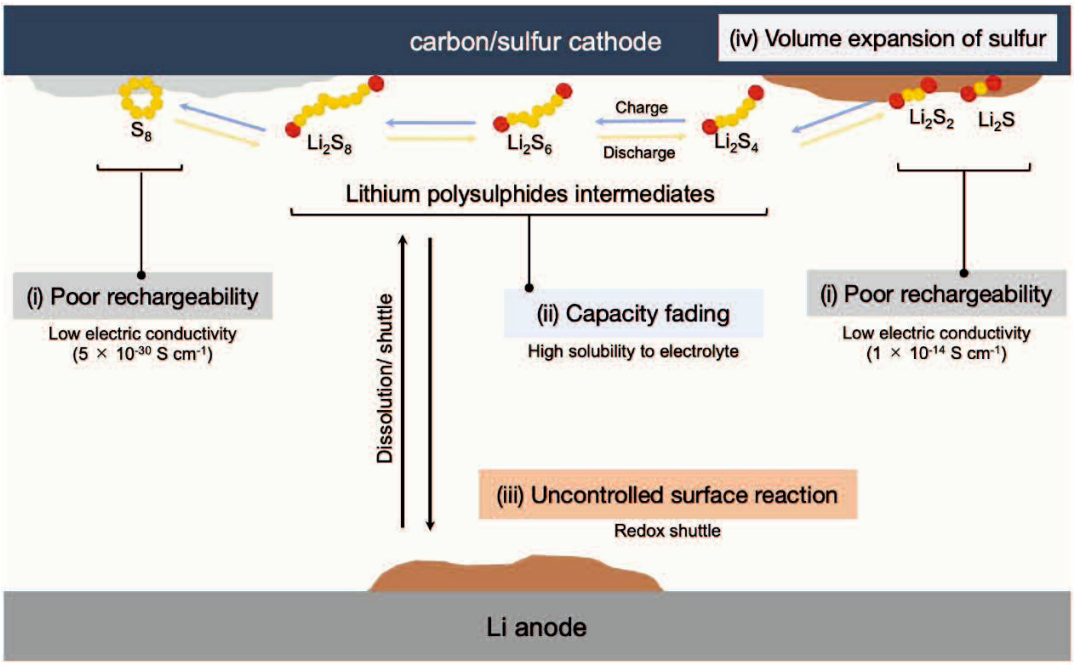

Figure 10. Summary of the disadvantages of Li–S batteries during the charge/discharge process.

6. Polymeric materials in LIBs

Polymeric materials play a vital role in current LIBs owing to their inherent mechanical and electrochemical stability and flexibility.[74] Moreover, polymeric materials with ions present ionic conductivity, which does not allow electrical conduction. These features have attracted considerable research attention aimed at improving battery performance by using polymers in LIBs.

6.1 Electrode binders

In conventional LIBs, both electrodes usually contain a polymeric binder, conductive additive, and active material, as shown in **Figure 11**.[75] The polymeric binder is used to retain the structure of the electrode and ensure cohesion between the active material and conductive additive.[76,77] Therefore, the characteristics of the polymeric binder affect the electrode properties, including the cycling performance, tolerance to volume expansion, rate capability, and morphology.[78] Thus, owing to the impact of polymeric binders on the battery performance, the following criteria must be satisfied.[75]

- Good adhesion to the current collector.
- High wettability to the electrolyte.
- High thermal and electrochemical stability (from 0 to 5 V_{Li}).
- Superior mechanical properties

Polymeric binders can be divided into three types of polymers: Synthetic polymers, natural polymers, and conductive polymers.

Polyvinylidene fluoride (PVDF) is the most widely used synthetic polymeric binder on both the laboratory and industrial scales, and it can be used with various active materials owing to its high electrochemical stability (0 to 5 V_{Li}) and high adhesion to the current collector.[75,79,80] Various synthetic polymers have been studied to further improve the electrode properties; these include the styrene butadiene block copolymer (SBR),[81] poly(vinylidenefluoride-co-hexafluoropropylene) (PVDF-HFP),[82] and poly(styrene-butene/ethylene-styrene) polymer binder (SEBS).[83] However, these polymeric binders are often prepared using N-methyl-2-pyrrolidone (NMP), which is highly toxic.[84]

Carboxymethyl cellulose (CMC) and cellulose are the most commonly known natural polymeric binders.[75] Natural polymers are considered as environmentally friendly binders. Moreover, they do not require NMP during their preparation.

Poly(3,4-ethylenedioxythiophene):polystyrene sulfonate (PEDOT:PSS) is a conductive polymer, which can improve electron transfer and prevent polysulfide dissolution in Li-S batteries.[75] Owing to its high electronic conductivity, the conductive materials can be replaced, leading to cheaper and lighter electrodes.[75]

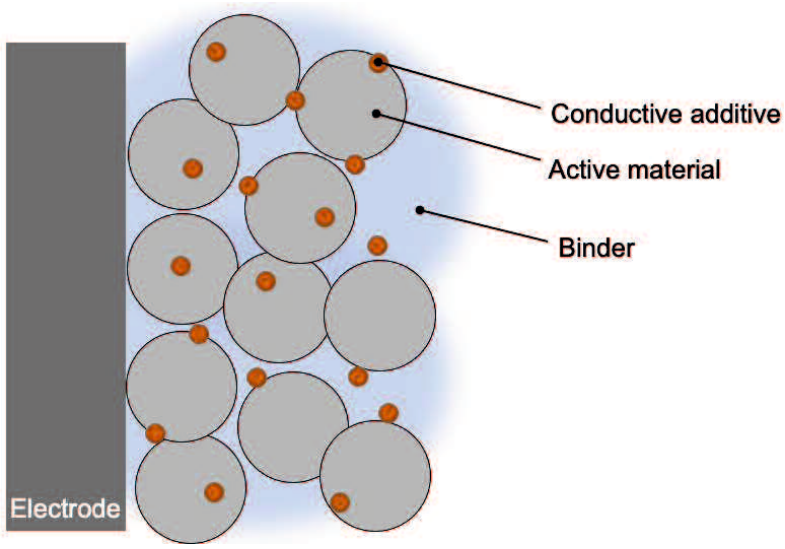

Figure 11. Schematic of the construction of electrodes.

6.2 Separators

Solid polymers are used as separators in current LIBs. The major roles of the separators in LIBs are shown in **Figure 12**. The separator physically separates the two electrodes to prevent their direct contact while permitting Li-ion diffusion. In addition, the separator can physically retard dendrite growth, which often results in catastrophic accidents.[85] Although separators do not electrochemically react in the battery, their characteristics, such as ionic conductivity, physical properties, and morphology, determine the battery performance. For example, their thickness is also a crucial factor determining the safety and volumetric energy density. A thicker separator can protect the battery from puncture and/or dendrite growth while increasing the total volume of battery and thus decrease the volumetric energy density. Other factors that impact the battery performance are shown below:[75]

- Porosity.
- Tortuosity.
- Structural stability.
- Mechanical stability.
- Wettability of the electrolyte.
- Thermal/chemical stability.
- Ionic conductivity.
- Electrical resistivity.

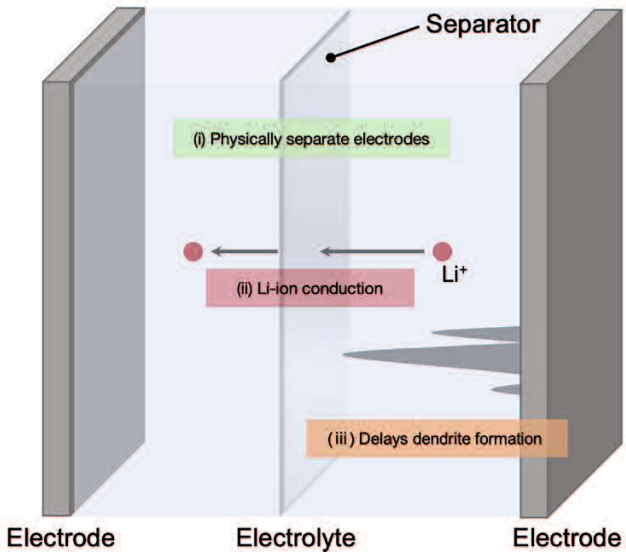

Figure 12. Schematic of the basic role of the separator in LIB

6.3 Polymer electrolytes (PEs)

Polymers are expected to be commercialized as solid-state electrolytes (known as PEs) owing to their high mechanical stability for retarding dendrite growth and low flammability, which contribute to the safe operation of LIBs.[75,86,87] Owing to their high mechanical stability, PEs can also act as separators, which contribute to lighter and cheaper LIBs. Furthermore, PEs can be used in various shaped batteries because of their high flexibility. Typically, PEs can be divided into two types of electrolytes: Gel polymer electrolytes (GPEs) containing non-aqueous solvents and SPEs.

6.3.1 Gel PEs

Various polymer materials have been employed as the host polymers of GPEs since Feuillade and Perch first prepared a GPE using the combination of poly(acrylonitrile) (PAN) with an aprotic solution containing an alkali metal salt in 1975.[88] Their construction is shown in **Figure 13**. It is accepted that the mechanical stability of GPEs is highly related to the nature of the host polymer used.[89] However, the properties of GPEs, including Li^+ transport, thermal stability, and electrochemical stability, depend on the solvent and Li salt used.[89,90] Li-ions diffuse through the liquid electrolyte, not through the polymer phase in GPEs. Although GPEs exhibit relatively high conductivities, some safety issues may arise owing to the use of flammable and volatile non-aqueous electrolytes. The absence of a non-aqueous electrolyte is the ultimate goal for achieving highly safe batteries.

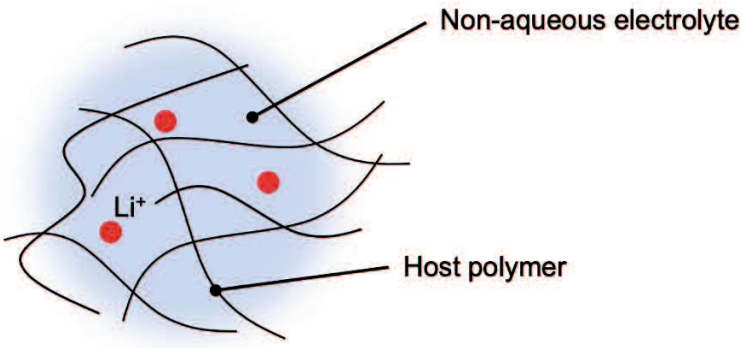

Figure 13. Schematic of a gel polymer electrolyte.

6.3.2 Solid polymer electrolyte

The replacement of conventional flammable electrolytes by SPEs has contributed to the completely safe operation of LIBs owing to their low flammability and solid nature. Thus, they are considered as next-generation electrolytes. The most widely studied polymeric material used for SPEs is poly(ethylene oxide) (PEO) (**Figure 14**), which was first proposed by Wright in 1975.[91] However, the ionic conductivity of SPEs is two orders of magnitude lower than that of a non-aqueous electrolyte at room temperature; the PEO and Li bis(trifluoromethane-sulfonyl)amide system (PEO/LiTFSA) has an ionic conductivity of ~0.05 mS cm^{-1}.[92,93] An improvement in the ionic conductivity of SPEs is urgently required for their commercialization.

It is accepted that the ionic conductivity is determined by the number of dissociated ions and their mobility within the polymer, as follows:[94]

$$\sigma = n \times \mu$$

where σ, n, and μ are the ionic conductivity, number of ions, and ion mobility, respectively.

To prepare an electrolyte with high ionic conductivity, (i) high salt dissociability and (ii) fast ion conduction are necessary. Slow ion exchange and hindered ionic conduction in the crystalline phase are typically responsible for the low ionic conductivity of SPEs.[95] Most ions flow through the conductive non-crystalline phase of the polymer. The Li^+ conduction mechanism in the non-crystalline phase of SPEs, such as PEO:LiX, is shown in **Figure 15**. The ether group in PEO initially interacts with Li^+, followed by separate Li^+ and X^-, forming an Li^+ solvating structure composed of four or five ether oxygens with one Li^+. The solvated Li^+ is then transported via an intra-chain/inter-chain ion exchange mechanism, which is induced by the segmental motion of the polymer chain. The segmental mobility of the polymer chain is represented by the glass transition temperature (T_g), at which the segmental motion is initiated. Considering the Li^+ conduction mechanism, the high dielectric constant of the polymer for high salt dissociability and high segmental mobility of the polymer for fast ion conduction are crucial for the high ionic conductivity of SPEs. SPEs suffer from the dilemma between salt dissociability and segmental mobility. Although a polymer with a high dielectric constant can dissolve a decent amount of the salt, its polar group is prone to form strong intramolecular/intermolecular interactions, hindering the segmental mobility of the polymer (lower T_g). For instance, PAN is expected to exhibit high salt dissociability due to the relatively high dielectric constant of the nitrile group, while it has a high T_g of 87 °C when compared to –130 °C for polyethylene without nitrile group in its polymer structure.[96,97] Consequently, many approaches have been employed for the past three decades to achieve comparable ionic conductivity to a non-aqueous electrolyte and sufficient mechanical strength.[94]

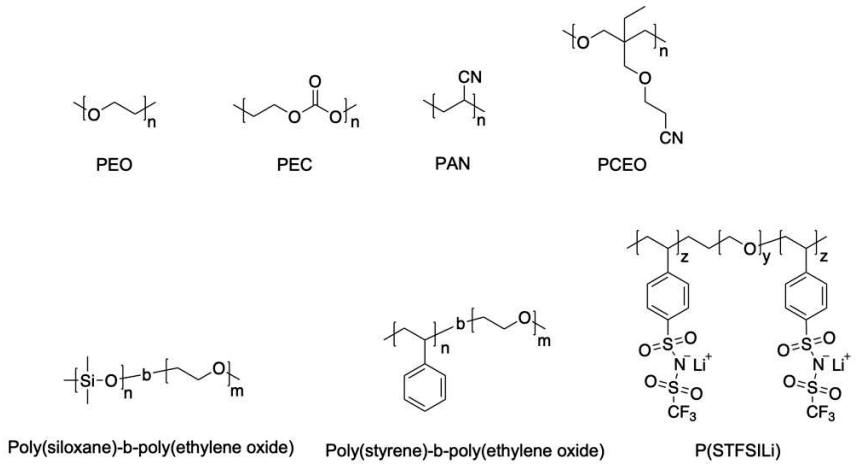

Figure 14. Structure of the host polymers used for SPEs.

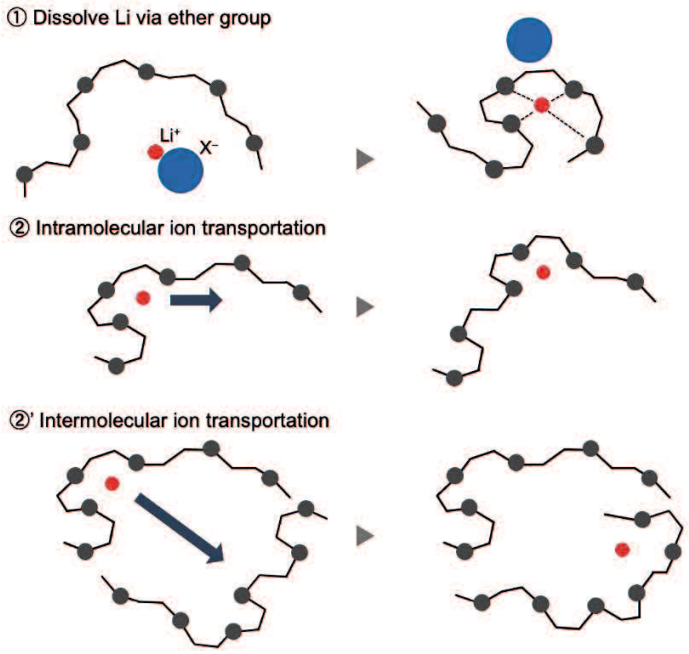

Figure 15. Schematic of the Li-ion transport mechanism in ether-based polymers.

Addition of an inorganic filler

Inorganic fillers such as TiO_2, Al_2O_3, and SiO_2 are added into the polymer to not only improve the ionic conductivity but also facilitate the mechanical stability of the polymer.[98,99,100,101,102,103,104] It is known that >6 GPa stability in terms of the rigidity is necessary to suppress Li dendrite growth, which is far from that of PEO (~200 MPa).[105,106,107] A PEO-based SPE exhibited improved mechanical stability above 100 °C when 10 vol% of Al_2O_3 was added.[104] The composite polymer prepared with 10 wt.% acidic Al_2O_3 nanoparticles showed an improved ionic conductivity of 5.61×10^{-5} S cm^{-1} when compared to that of without filler (7.03×10^{-6} S cm^{-1}) at room temperature.[108] The improved ionic conductivity has been attributed to the increased amorphous phase of PEO formed after adding the inorganic filler and/or the ion conduction pathways formed on the filler surface, as shown in **Figure 16**.[108,109] Furthermore, the interfacial properties were also improved upon the addition of an inorganic filler. Composite SPEs composed of an PEO-based SPE and $LiAlO_2$ exhibit a lower interfacial resistance on the Li/SPEs interface than those without filler.[110] The evolution of the interfacial resistance of filler composite SPEs and pure SPEs was compared and the inorganic filler found to clearly suppresses the growth of the SEI, which was attributed to the scavenging effect of the inorganic filler against residual water and other impurities.

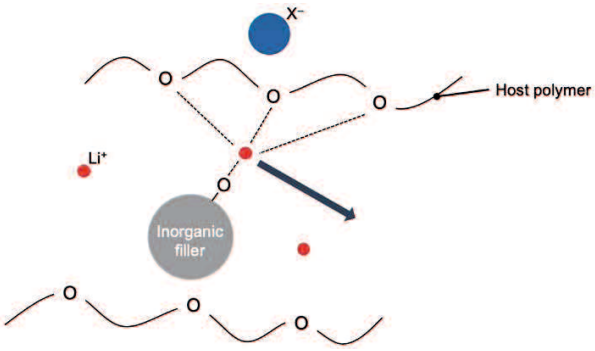

Figure 16. Schematic of the Li-ion transport mechanism in a composite polymer electrolyte.[108,109]

Block copolymers

Designing a block copolymer is an ideal approach to improve the electrolytic properties of SPEs since it can tune the properties by combining more than two polymers with different characteristics.[111] For example, combining PEO with poly(siloxane), which has high flexibility (T_g: −123 °C) and good thermal and mechanical stability, presents 3.0×10^{-4} S cm^{-1} at room temperature together with high cathodic stability up to 5.0 V_{Li}.[112,113] To improve the mechanical stability, PEO and polystyrene block copolymers have been studied and found to improve the mechanical strength; however, the resulting ionic conductivity is low due to the introduction of a non-ionic conductive polystyrene phase.[114] Furthermore, single ion conducting SPEs have been developed by combining a single ion conducting polymer with PEO to improve the Li^+ transfer number of conventional PEO-based electrolytes (~0.2).[115] For example, the combination of Li poly(4-styrenesulfonyl(trifluoromethyl sulfonyl)imide) (P(STFSILi)) leads to single ion conduction due to the incorporated Li^+. The Li^+ transfer number is high (>0.85), as expected, while the ionic conductivity is very low (1.3×10^{-5} S

cm^{-1} at 60 °C) due to the strong interaction between Li^+ and the polyanion backbone as well as the reduction in the contribution from the anion to the overall conductivity.[116,117] The structure of these block copolymers are shown in **Figure 14**.

Designing host polymer structures

Several studies utilizing alternative polymers to PEO have been reported to date. Polycarbonate is a promising polymer owing to its large number of dissociated ions. Polyethylene carbonate (PEC) (**Figure 14**) accommodates an extremely large number of salts (up to 180 wt.%).[118] Moreover, the segmental mobility of PEC increases upon the addition of an Li salt, in contrast to PEO, where the segmental mobility decreases with the addition of Li salt. This is because the intermolecular interactions in PEC are released by alternating the interaction between the polar group and Li^+ after adding Li salt. This is opposite to the case for PEO, where a strong interaction between the ether group and Li^+ occurs. PEC-based SPEs display a high Li^+ transfer number of 0.4 when compared to PEO. Similar trends with PEC-based SPEs were observed for PAN-based SPEs (**Figure 14**). The interaction between the nitrile groups relax after adding the Li salt, increasing segmental mobility.[119] PAN-based SPEs can transport Li^+ at around the T_g, where segmental mobility does not occur, which is considered as decoupled ion transportation.[120]

Tuning the sidechains of polymers

Tuning the sidechain structure of the polymer potentially allows the precise tuning of key factors to improve the ionic conductivity, including the polymer segmental mobility and salt dissociability.

One of the most well-known sidechain modifications the preparation of comb-like polymers, which has a functional sidechain along its backbone.[121,122,123,124,125] Watanabe *et al.* first implemented a comb-like polymer electrolyte bearing an EO sidechain, which revealed the introduction of the sidechain effectively inhibited the crystallization of the polymer, improving the ionic conductivity.[121] The longer sidechain in the peptoid polymer backbone showed high polymer mobility and ionic conductivity when compared to the shorter sidechain.[126]

Our group previously reported poly(3-(2-cyanoethoxymethyl)-3-ethyloxetane) (PCEO) (**Figure 14**) bearing ether and nitrile groups on the sidechain, which exhibits a high ionic conductivity of 7.3×10^{-4} S cm^{-1} at 70 °C and high salt concentration.[127] The high ionic conductivity of PCEO can be attributed to the moderate interaction of Li with the ether and nitrile groups.[128,129] Although a non-polar alkyl sidechain does not directly contribute to Li^+ conduction, the existence of an alkyl sidechain clearly changes the ionic conductivity. In addition, the length of the alkyl sidechain also has an impact on Li^+ conduction by altering the Li^+ solvated structure.[130] However, the complicated synthesis procedure used to prepare the polymer limits the variety and tunability of the sidechain used.

Research purpose

The aim of this work is to overcome the obstacles to improving LIBs using polymers and evaluate the effects of polymeric materials on the battery performance. In chapter 1, we prepare polymers using an amidation reaction, which can simply modify the sidechain, to improve the ionic conductivity of SPEs. As a characteristic sidechain we chose a multiple cyanoethoxy sidechain, which is expected to exhibit high ionic conductivity, and analyzed the effect of the amide group and cyanoethoxy sidechain on the mobility and ionic transportation. In chapter 2, we have focused on revealing the electrochemical reaction of a PEO-based electrolyte against the anode (the formation of the SEI) by combining *operando* ATR–IR and *ex-situ* XPS measurements. Moreover, the correlation between the obtained decomposed products and surface resistance was also investigated using EIS measurements. In chapter 3, for good rechargeability and the enhanced cycle life of Li-S batteries, we prepared new polymer-anchored carbon materials bearing different flexible polymers (PEG or PPG), which aim to accommodate the volume expansion of sulfur during the charge/discharge process. The contribution from the anchored polymer was evaluated upon comparison with some conventional carbon materials, which confirmed the anchored polymer plays an important role to improve the battery performance.

Research outline

Chapter 1

To verify the effect of the amide group with the cyanoethoxy group on ionic transportation, we synthesized a series of poly(oxetane)-based polymers bearing different branched sidechains [i.e., methyl (PtBuOA) and bulky cyanoethoxy group (P3CEOA)] via an amidation reaction. Spectro(electro)chemical analysis verified that the large steric hindrance of the cyanoethoxy sidechain effectively breaks the hydrogen bond network and dipole interactions within the polymer, both of which decrease the polymer segmental mobility, leading to better long-range Li^+ conduction. Furthermore, the unique Li^+ coordination structure consists of a cyano group, ether/carboxyl oxygen, and TFSA anion in the P3CEOA electrolyte, which has moderate stability and effectively promotes the short-range Li^+ conduction. The amide group with a relatively high dielectric constant improves the dissociability of the Li salt. We confirmed that over three orders of magnitude improvement in the ionic conductivity was observed upon introducing the cyanoethoxy sidechain when compared to the PtBuOA electrolyte bearing a methyl sidechain. This study provides a holistic picture of the effect of the sidechain structure on the intermolecular interactions and establishes a new design strategy for PEs, which enables the precise tuning of the molecular interactions using the sidechain structure.

Chapter 2

This paper describes studies on the SEI formed by SPEs using a combination of operando-IR, ex-situ XPS, and EIS measurements. We have studied the electrochemical reaction occurring between the Cu electrode and most common SPEs containing poly(ethylene oxide)

with bis(trifluoromethanesulfonyl)amide (LiTFSA) as a function of the potential. We reveal that the SEI at Cu/PEO–LiTFSA was formed via several reduction reactions, i.e., the reduction of PEO, LiTFSA, and impurities. The most resistive SEI is observed at 0.8 V_{Li}, which consists of ROLi, alkyl vinyl ether, LiOH, Li_2CO_3, and a small amount of LiF. Moreover, alkyl vinyl ether is further reduced to form other alkyl ethers via radical propagation, which leads to a relatively low SEI resistance.

Chapter 3

We propose sulfur-inserted polymer-anchored edge exfoliated graphite as a positive electrode to accommodate the conflicting requirement of physically restraining sulfur dissolution, while maintaining structural flexibility to cope with the volume expansion observed upon charging/discharging. The introduction of sulfur between the flexible polymer-anchored graphene layers was achieved using a simple chemical reaction at ambient temperature. The obtained sulfur–carbon composite demonstrates superior sulfur efficiency and cyclability when compared to its mesoporous carbon-based counterparts. The strong interfacial attraction between sulfur and the highly conductive graphene sheets at the confined interlayer space enables rapid charge transfer and effectively inhibits polysulfide dissolution, resulting in improved redox reaction reversibility and sulfur efficiency. More importantly, the structural flexibility of the layered structure derived from the polymer-anchor guarantees stable cycling by accommodating the significant volume expansion of sulfur active materials.

1 L. Long, S. Wang, M. Xiao and Y. Meng, *J. Mater. Chem. A*, 2016, **4**, 10038–10039.

2 J. M. Tarascon and M. Armand, *Nature*, 2001, **414**, 359–367.

3 M. Wakihara, *Mater. Sci. Eng. R Reports*, 2001, **33**, 109–134.

4 J. B. Goodenough and K. S. Park, *J. Am. Chem. Soc.*, 2013, **135**, 1167–1176.

5 J. Asenbauer, T. Eisenmann, M. Kuenzel, A. Kazzazi, Z. Chen and D. Bresser, *Sustain. Energy Fuels*, 2020, **4**, 5387–5416.

6 K. Ozawa, *Solid State Ionics*, 1994, **69**, 212–221.

7 M. M. Thackeray, *J. Am. Ceram. Soc.*, 1999, **82**, 3347–3354.

8 A. K. Padhi, K. S. Nanjundaswamy and J. B. Goodenough, *Electrochem. Soc.*, 1997, **144**, 1188–1194.

9 K. Xu, *Chem. Rev.*, 2004, **104**, 4303–4417.

10 P. G. Balakrishnan, R. Ramesh and T. Prem Kumar, *J. Power Sources*, 2006, **155**, 401–414.

11 Ministry of Economy, Trade and Industry in Japan, 2016, Status of Product Accidents, etc.

12 Q. Wang, P. Ping, X. Zhao, G. Chu, J. Sun and C. Chen, *J. Power Sources*, 2012, **208**, 210–224.

13 J. B. Goodenough and Y. Kim, *Chem. Mater.*, 2010, **22**, 587–603.

14 R. M. Spotnitz, J. Weaver, G. Yeduvaka, D. H. Doughty and E. P. Roth, *J. Power Sources*, 2007, **163**, 1080–1086.

15 B. K. Mandal, A. K. Padhi, Z. Shi, S. Chakraborty and R. Filler, *J. Power Sources*, 2006, **161**, 1341–1345.

16 G. L. Woods, K. L. White, D. K. Vanderwall, G. P. Li, K. I. Aston, T. D. Bunch, L.

N. Meerdo and B. J. Pate, *Science*, 2003, **301**, 1063.

17 Q. Wang and J. Sun, *Mater. Lett.*, 2007, **61**, 3338–3340.

18 G. Venugopal, *J. Power Sources*, 2001, **101**, 231–237.

19 Q. Wang, J. Sun, X. Chen, G. Chu and C. Chen, *Mater. Res. Bull.*, 2009, **44**, 543–548.

20 Y. Shigematsu, M. Ue and J. Yamaki, *J. Electrochem. Soc.*, 2009, **156**, A176.

21 S. Y. Lee, S. K. Kim and S. Ahn, *J. Power Sources*, 2007, **174**, 480–483.

22 J. I. Yamaki, Y. Baba, N. Katayama, H. Takatsuji, M. Egashira and S. Okada, *J. Power Sources*, 2003, **119–121**, 789–793.

23 R. Spotnitz and J. Franklin, *J. Power Sources*, 2003, **113**, 81–100.

24 E. G. Shim, T. H. Nam, J. G. Kim, H. S. Kim and S. I. Moon, *Electrochim. Acta*, 2007, **53**, 650–656.

25 H. F. Xiang, H. W. Lin, B. Yin, C. P. Zhang, X. W. Ge and C. H. Chen, *J. Power Sources*, 2010, **195**, 335–340.

26 H. J. Kweon, J. J. Park, J. W. Seo, G. B. Kim, B. H. Jung and H. S. Lim, *J. Power Sources*, 2004, **126**, 156–162.

27 L. X. Yuan, Z. H. Wang, W. X. Zhang, X. L. Hu, J. T. Chen, Y. H. Huang and J. B. Goodenough, *Energy Environ. Sci.*, 2011, **4**, 269–284.

28 L. J. Fu, H. Liu, C. Li, Y. P. Wu, E. Rahm, R. Holze and H. Q. Wu, *Solid State Sci.*, 2006, **8**, 113–128.

29 X. G. Sun and S. Dai, *J. Power Sources*, 2010, **195**, 4266–4271.

30 A. N. Dey, *J. Electrochem. Soc.*, 1970, **117**, C248.

31 E. Peled, *J. Electrochem. Soc.*, 1979, **126**, 2047.

32 P. Verma, P. Maire and P. Novák, *Electrochim. Acta*, 2010, **55**, 6332–6341.

33 R. Yazami and Y. F. Reynier, *Electrochim. Acta*, 2002, **47**, 1217–1223.

34 A. Wang, S. Kadam, H. Li, S. Shi and Y. Qi, *Npj Comput. Mater.*, 2018, **4**, 1–26.

35 P. Novák, J. C. Panitz, F. Joho, M. Lanz, R. Imhof and M. Coluccia, *J. Power Sources*, 2000, **90**, 52–58.

36 K. Zaghib, G. Nadeau and K. Kinoshita, *J. Electrochem. Soc.*, 2000, **147**, 2110.

37 H. Yang and P. N. Ross, *Electrochem. Solid-State Lett.*, 2005, **8**, A441–A445.

38 G. Gachot, P. Ribière, D. Mathiron, S. Grugeon, M. Armand, J. B. Leriche, S. Pilard and S. Laruelle, *Anal. Chem.*, 2011, **83**, 478–485.

39 S.-K. Jeong, M. Inaba, T. Abe and Z. Ogumi, *J. Electrochem. Soc.*, 2001, **148**, A989–A993.

40 Q. Ye, T. S. Zhao, H. Yang and J. Prabhuram, *Electrochem. Solid-State Lett.*, 2005, **8**, 1–4.

41 R. Dedryvère, H. Martinez, S. Leroy, D. Lemordant, F. Bonhomme, P. Biensan and D. Gonbeau, *J. Power Sources*, 2007, **174**, 462–468.

42 E. Peled, D. Golodnitsky, G. Ardel and V. Eshkenazy, *Electrochim. Acta*, 1995, **40**, 2197–2204.

43 E. Peled, D. Golodnitsky and G. Ardel, *J. Electrochem. Soc.*, 1997, **144**, L208–L210.

44 F. Kong and F. McLarnon, *J. Power Sources*, 2000, **89**, 180–189.

45 Y. Zhang, Y. Katayama, R. Tatara, L. Giordano, Y. Yu, D. Fraggedakis, J. G. Sun, F. Maglia, R. Jung, M. Z. Bazant and Y. Shao-Horn, *Energy Environ. Sci.*, 2020, **13**, 183–199.

46 Y. Yu, P. Karayaylali, Y. Katayama, L. Giordano, M. Gauthier, F. Maglia, R. Jung,

I. Lund and Y. Shao-Horn, *J. Phys. Chem. C*, 2018, **122**, 27368–27382.

47 G. Zhuang, K. Wang, G. Chottiner, R. Barbour, Y. Luo, I. T. Bae, D. Tryk and D. A. Scherson, *J. Power Sources*, 1995, **54**, 20–27.

48 T. Ichino, B. D. Cahan and D. A. Scherson, *J. Electrochem. Soc.*, 1991, **138**, L59–L61.

49 P. G. Bruce, S. A. Freunberger, L. J. Hardwick and J. M. Tarascon, *Nat. Mater.*, 2012, **11**, 19–29.

50 P. Tobias, K. Richard, D. Simon and W. Martin, *J. Solid State Electrochem.*, 2017, **21**, 1939–1964.

51 S. A. Freunberger, Y. Chen, Z. Peng, J. M. Griffin, L. J. Hardwick, F. Bardé, P. Novák and P. G. Bruce, *J. Am. Chem. Soc.*, 2011, **133**, 8040–8047.

52 F. MIZUNO, S. NAKANISHI, Y. KOTANI, S. YOKOISHI and I. Hideki, *Electrochemistry*, 2010, **78**, 403–405.

53 C. O. Laoire, S. Mukerjee, K. M. Abraham, E. J. Plichta and M. A. Hendrickson, *J. Phys. Chem. C*, 2010, **114**, 9178–9186.

54 C. Ó. Laoire, S. Mukerjee, E. J. Plichta, M. A. Hendrickson and K. M. Abraham, *J. Electrochem. Soc.*, 2011, **158**, A302.

55 J. G. Zhang, D. Wang, W. Xu, J. Xiao and R. E. Williford, *J. Power Sources*, 2010, **195**, 4332–4337.

56 W. Xu, J. Xiao, D. Wang, J. Zhang and J. G. Zhang, *Electrochem. Solid-State Lett.*, 2010, **13**, A48–A51,.

57 L. Zhou, D. L. Danilov, R. A. Eichel and P. H. L. Notten, *Adv. Energy Mater.*, 2021, **11**, 1–49.

58 S.-E. Cheon, K.-S. Ko, J.-H. Cho, S.-W. Kim, E.-Y. Chin and H.-T. Kim, *J. Electrochem. Soc.*, 2003, **150**, A800.

59 Y. J. Choi, K. W. Kim, H. J. Ahn and J. H. Ahn, *J. Alloys Compd.*, 2008, **449**, 313–316.

60 H. S. Ryu, Z. Guo, H. J. Ahn, G. B. Cho and H. Liu, *J. Power Sources*, 2009, **189**, 1179–1183.

61 B. Jin, L. Yang, J. Zhang, Y. Cai, J. Zhu, J. Lu, Y. Hou, Q. He, H. Xing, X. Zhan, F. Chen and Q. Zhang, *Adv. Energy Mater.*, 2019, **9**, 1–10.

62 H. Yao, K. Yan, W. Li, G. Zheng, D. Kong, Z. W. Seh, V. K. Narasimhan, Z. Liang and Y. Cui, *Energy Environ. Sci.*, 2014, **7**, 3381–3390.

63 H. Wang, Y. Yang, Y. Liang, J. T. Robinson, Y. Li, A. Jackson, Y. Cui and H. Dai, *Nano Lett.*, 2011, **11**, 2644–2647.

64 J. Shim, K. A. Striebel and E. J. Cairns, *J. Electrochem. Soc.*, 2002, **149**, A1321.

65 J. Hassoun and B. Scrosati, *Angew. Chem. Int. Ed.*, 2010, **49**, 2371–2374.

66 D. Marmorstein, T. H. Yu, K. A. Striebel, F. R. Mclarnon, J. Hou and E. J. Cairns, *J. Power Sources*, 2000, **89**, 219–226.

67 Y. Yang, G. Zheng and Y. Cui, *Chem. Soc. Rev.*, 2013, **42**, 3018–3032.

68 J. H. Shin and E. J. Cairns, *J. Power Sources*, 2008, **177**, 537–545.

69 L. Yuan, H. Yuan, X. Qiu, L. Chen and W. Zhu, *J. Power Sources*, 2009, **189**, 1141–1146.

70 G. He, X. Ji and L. Nazar, *Energy Environ. Sci.*, 2011, **4**, 2878–2883.

71 R. Demir-Cakan, M. Morcrette, F. Nouar, C. Davoisne, T. Devic, D. Gonbeau, R. Dominko, C. Serre, G. Férey and J. M. Tarascon, *J. Am. Chem. Soc.*, 2011, **133**,

16154–16160.

72 S. Evers and L. F. Nazar, *Chem. Commun.*, 2012, **48**, 1233–1235.

73 G. Zheng, Y. Yang, J. J. Cha, S. S. Hong and Y. Cui, *Nano Lett.*, 2011, **11**, 4462–4467.

74 A. Saal, T. Hagemann and U. S. Schubert, *Adv. Energy Mater.*, 2021, **11**, 1–40.

75 C. M. Costa, E. Lizundia and S. Lanceros-Méndez, *Prog. Energy Combust. Sci.*, 2020, **79**, 100846.

76 A. Cholewinski, P. Si, M. Uceda, M. Pope and B. Zhao, *Polymers*, 2021, **13**, 1–20.

77 H. Zheng, R. Yang, G. Liu, X. Song and V. S. Battaglia, *J. Phys. Chem. C*, 2012, **116**, 4875–4882.

78 B. Lestriez, *Comptes Rendus Chim.*, 2010, **13**, 1341–1350.

79 L. A. Riley, S. H. Lee, L. Gedvilias and A. C. Dillon, *J. Power Sources*, 2010, **195**, 588–592.

80 N. Dietz Rago, J. Bareño, J. Li, Z. Du, D. L. Wood, L. A. Steele, J. Lamb, S. Spangler, C. Grosso, K. Fenton and I. Bloom, *J. Power Sources*, 2018, **385**, 148–155.

81 L. Wang, Y. Fu, V. S. Battaglia and G. Liu, *RSC Adv.*, 2013, **3**, 15022–15027.

82 A. V. Le, M. Wang, D. J. Noelle, Y. Shi, Y. Shirley Meng, D. Wu, J. Fan and Y. Qiao, *Int. J. Energy Res.*, 2017, **41**, 2430–2438.

83 R. Gonçalves, J. Oliveira, M. P. Silva, P. Costa, L. Hilliou, M. M. Silva, C. M. Costa and S. Lanceros-Méndez, *ACS Appl. Energy Mater.*, 2018, **1**, 3331–3341.

84 M. Zackrisson, L. Avellán and J. Orlenius, *J. Clean. Prod.*, 2010, **18**, 1519–1529.

85 S. Choi, S. Mugobera, J. M. Ko and K. S. Lee, *Colloids Surfaces A Physicochem.*

Eng. Asp., 2021, **631**, 127722.

86 L. Long, S. Wang, M. Xiao and Y. Meng, *J. Mater. Chem. A*, 2016, **4**, 10038–10039.

87 A. Arya and A. L. Sharma, *Ionics*, 2017, 23, 497–540.

88 G. Feuillade and P. Perche, *J. Appl. Electrochem.*, 1975, **5**, 63–69.

89 F. Baskoro, H. Q. Wong and H. J. Yen, *ACS Appl. Energy Mater.*, 2019, **2**, 3937–3971.

90 K. Xu, *Chem. Rev.*, 2014, **114**, 11503–11618.

91 P. V. Wright, *Br. Polym. J.*, 1975, **7**, 319–327.

92 A. VALLBE, S. BESNER and J. PRUD'HOMME, *Electrochim. Acta* 1992, **37**, 1579–1583.

93 K. Pożyczka, M. Marzantowicz, J. R. Dygas and F. Krok, *Electrochim. Acta*, 2017, **227**, 127–135.

94 J. Lopez and D. G. Mackanic, *Nat. Rev. Mater.*, 2019, **4**, 312–330.

95 Q. Yang, A. Wang, J. Luo and W. Tang, *Chinese J. Chem. Eng.*, 2022, **43**, 202–215.

96 W. H. Howard, *J. Appl. Polym. Sci.*, 1961, **5**, 303–307.

97 O. H. Fred-Ahmadu, G. Bhagwat, I. Oluyoye, N. U. Benson, O. O. Ayejuyo and T. Palanisami, *Sci. Total Environ.*, 2020, **706**, 1-12.

98 F. Croce, G. B. Appetecchi, L. Persi and B. Scrosati, *Nat. Lett.*, 1998, **394**, 456–458.

99 M. Wetjen, M. A. Navarra, S. Panero, S. Passerini, B. Scrosati and J. Hassoun, *ChemSusChem*, 2013, **6**, 1037–1043.

100 K. Vignarooban, M. A. K. L. Dissanayake, I. Albinsson and B. E. Mellander, *Solid State Ionics*, 2014, **266**, 25–28.

101 G. B. Appetecchi, F. Croce, J. Hassoun, B. Scrosati, M. Salomon and F. Cassel, *J.*

Power Sources, 2003, **114**, 105–112.

102 A. S. Best, J. Adebahr, P. Jacobsson, D. R. MacFarlane and M. Forsyth, *Macromolecules*, 2001, **34**, 4549–4555.

103 I. W. Cheung, K. B. Chin, E. R. Greene, M. C. Smart, S. Abbrent, S. G. Greenbaum, G. K. S. Prakash and S. Surampudi, *Electrochim. Acta*, 2003, **48**, 2149–2156.

104 J. E. Weston and B. C. H. Steele, *Solid State Ionics*, 1982, **7**, 75–79.

105 G. Homann, L. Stolz, J. Nair, I. C. Laskovic, M. Winter and J. Kasnatscheew, *Sci. Rep.*, 2020, **10**, 2–10.

106 R. Khurana, J. L. Schaefer, L. A. Archer and G. W. Coates, *J. Am. Chem. Soc.*, 2014, **136**, 7395–7402.

107 J. Lopez, D. G. Mackanic, Y. Cui and Z. Bao, *Nat. Rev. Mater.*, 2019, **4**, 312–330.

108 P. A. R. D. Jayathilaka, M. A. K. L. Dissanayake, I. Albinsson and B. E. Mellander, *Electrochim. Acta*, 2002, **47**, 3257–3268.

109 C. W. Nan, L. Fan, Y. Lin and Q. Cai, *Phys. Rev. Lett.*, 2003, **91**, 1–4.

110 F. Croce, L. Persi, F. Ronci and B. Scrosati, *Solid State Ionics*, 2000, **135**, 47–52.

111 W. S. Young, W. F. Kuan and T. H. Epps, *J. Polym. Sci. Part B Polym. Phys.*, 2014, **52**, 1–16.

112 Z. Zhang, D. Sherlock, R. West, R. West, K. Amine and L. J. Lyons, *Macromolecules*, 2003, **36**, 9176–9180.

113 C. P. Fonseca and S. Neves, *J. Power Sources*, 2002, **104**, 85–89.

114 I. Gurevitch, R. Buonsanti, A. A. Teran, B. Gludovatz, R. O. Ritchie, J. Cabana and N. P. Balsara, *J. Electrochem. Soc.*, 2013, **160**, 1611–1617.

115 W. Gorecki, C. Roux, M. Clémancey, M. Armand and E. Belorizky,

ChemPhysChem, 2002, **3**, 620–625.

116 R. Bouchet, S. Maria, R. Meziane, A. Aboulaich, L. Lienafa, J. Bonnet, T. N. T. Phan, D. Bertin, D. Gigmes, D. Devaux, R. Denoyel and M. Armand, *Nat. Mater.*, 2013, **12**, 1–6.

117 S. W. Ryu, P. E. Trapa, S. C. Olugebefola, J. A. Gonzalez-Leon, D. R. Sadoway and A. M. Mayes, *J. Electrochem. Soc.*, 2005, **152**, 158–163.

118 Y. Tominaga and K. Yamazaki, *Chem. Commun.*, 2014, **50**, 4448–4450.

119 Z. Florjańczyk, E. Zygadło-Monikowska, W. Wieczorek, A. Ryszawy, A. Tomaszewska, K. Fredman, D. Golodnitsky, E. Peled and B. Scrosati, *J. Phys. Chem. B*, 2004, **108**, 14907–14914.

120 M. Forsyth, D. R. MacFarlane and A. J. Hill, *Electrochim. Acta*, 2000, **45**, 1243–1247.

121 M. Watanabe and A. Nishimoto, *Solid State Ionics*, 1995, **79**, 306–312.

122 A. Nishimoto, K. Agehara, N. Furuya, T. Watanabe and M. Watanabe, *Macromolecules*, 1999, **32**, 1541–1548.

123 Y. Ikeda, Y. Wada, Y. Matoba, S. Murakami and S. Kohjiya, *Electrochim. Acta*, 2000, **45**, 1167–1174.

124 J. Karo and D. Brandell, *Solid State Ionics*, 2009, **180**, 1272–1284.

125 X. Ji, L. L. Xiao, Y. Zhang, K. Yue, X. Zhou and Z. H. Guo, *ACS Appl. Energy Mater.*, 2022, **5**, 8410–8418.

126 J. Sun, G. M. Stone, N. P. Balsara and R. N. Zuckermann, *Macromolecules*, 2012, **45**, 5151–5156.

127 R. Sai, K. Ueno, K. Fujii, Y. Nakano, N. Shigaki and H. Tsutsumi, *Phys. Chem.*

Chem. Phys., 2017, **19**, 5185–5194.

128 R. Sai, K. Ueno, K. Fujii, Y. Nakano and H. Tsutsumi, *RSC Adv.*, 2017, **7**, 37975–37982.

129 R. Matsuoka, M. Shibata, K. Matsuo, R. Sai, H. Tsutsumi, K. Fujii and Y. Katayama, *Macromolecules*, 2020, **53**, 9480−9490.

130 R. Sai, S. Hirata, H. Tsutsumi and Y. Katayama, *Front. Chem.*, 2022, **10**, 1–12.

YAMAGUCHI
UNIVERSITY

Chapter 1

Improved ionic conductivity for amide-containing electrolytes by tuning intermolecular interaction: the effect of branched side-chains with cyanoethoxy groups

1.1 Introduction

An ideal polymer structure for SPE has been explored for several decades, in order to achieve the safety operation of LIBs. Although side-chain modification of polymer is considered as one of the most effective ways to find ideal polymer, the synthesis of side-chain modified polymer is complicated and limits the tunability of side-chain. In this context, we focus on the amidation reaction enabling easy modification of side-chain due to one step reaction process. The high dielectric constant of amide group can facilitate the salt dissociation, improving ionic conductivity. However, the hydrogen-bonding network among the amide group suppresses the polymer mobility, leading low ionic conductivity. Motivated this advantage and disadvantage of amide group, two polymers with and without bulky sidechain next to the amide group were synthesized to clarify the effect of bulky side chain next to amide group on the performance of electrolyte. The segmental mobility of the polymer (T_g) of each polymer and electrolyte was evaluated by differential scanning calorimetry (DSC) measurement. Infrared spectroscopy was conducted to reveal the detailed intermolecular interaction occurring in both polymers and corresponding electrolytes. The ionic conductivity of both electrolytes was determined by the AC impedance

spectroscopy, and VTF fitting provides the detail information of ion transportation mechanism in both electrolytes.

1.2 Experimental

Monomer synthesis

The monomer of poly(3-ethyl-3-cyanoethoxymethyloxetaneamide) (P3CEOA), 3-ethyl-3-cyanoethoxymethyloxetaneamide (3CEOA) was synthesized through the condensation reaction of 3-ethyl-3-cyanoethoxymethyloxetanecarbonyl (EOC) and 3,3'-((2-amino-2-((2-cyanoethoxy)methyl)propane-1,3-diyl)bis(oxy))dipropanenitrile (3CE) by following procedure.

Jones reagent was prepared by mixing chromium oxide VI (Wako Pure Chemical Co., 53.45 g), sulfuric acid (Sigma-Aldrich Co. LLC, 46 mL) and water (so as total volume to 200 mL). 3-ethyl-3oxetanemethanol (EHO, Tokyo Chemical Industry Co., Ltd, 24.84 g) acetone solution was added dropwise over a period of 30 min to Jones reagent (200 mL) dissolved in acetone (Wako Pure Chemical Co., 700 mL), subsequently stirred at 0°C for 2 h. The reaction mixture was quenched by adding isopropyl alcohol (Wako Pure Chemical Co.). After extracting the solution with dichloromethane (Wako Pure Chemical Co.) and water, volatile dichloromethane was removed using a rotary evaporator. The EOC was obtained by distilling the residue under reduced pressure (160°C, 0.02 mmHg), Yield: 40 %.

^{1}H NMR (δ, ppm from trimethylsilane (TMS) in $CDCl_3$): 0.89 (t, 3H, –$CH_2C\underline{H}_3$), 2.02 (q, 2H, –$C\underline{H}_2CH_3$), 4.44, 4.90 (dd, 4H, –$C\underline{H}_2$–O–$C\underline{H}_2$–) 9.09 (s, 1H, –COO$\underline{H}$)

40 wt% KOH (Wako Pure Chemical Co.) aqueous solution, tris(hydroxymethyl) aminomethane (THAM, Tokyo Chemical Industry Co., Ltd, 12.2 g), dioxane (Wako Pure

Chemical Co., 100 mL) and acrylonitrile (Wako Pure Chemical Co., 39.3 mL) was mixed and stirred for 24 h at room temperature, then the solution was neutralized with 1 M HCl (Wako Pure Chemical Co., 100 mL). After extracting the solution with dichloromethane and water, volatile dichloromethane was removed using a rotary evaporator, subsequently purified via column chromatography (methanol (Wako Pure Chemical Co.): ethyl acetate (Wako Pure Chemical Co.) = 1: 4). Yield: 31%

^{1}H NMR (δ, ppm from trimethylsilane (TMS) in $CDCl_3$): 2.62 (t, 2H, –C$\underline{H}_2$CN), 3.46 (s, 2H, C–C$\underline{H}_2$–O), 3.70 (t, 2H, –C$\underline{H}_2$$CH_2$CN)

3CEOA was synthesized by following procedure. EOC (6.72 g), 3CE (14.46 g), 1-ethyl-3-(3-dimethylaminopropyl)carbodiimide hydrochloride (EDC·HCl, Tokyo Chemical Industry Co., Ltd, 11.87 g), and 4-dimethylaminopyridine (DMAP, Wako Pure Chemical Co., 25.90 g) was dissolved into dichloromethane (250 mL), subsequently stirred at room temperature for 24 h. After condensation reaction, the solution was neutralized with 1 M HCl (100 mL) then washed with saturated $NaHCO_3$ (Wako Pure Chemical Co.) aqueous solution. Remained dichloromethane was removed with a rotary evaporator. The obtained solution was purified via re-crystallization. Yield: 58 %

^{1}H NMR (δ, ppm from trimethylsilane (TMS) in $CDCl_3$): 0.93 (t, 3H, –CH_2C$\underline{H}_3$), 2.02 (q, 2H, –C$\underline{H}_2$$CH_3$), 2.61 (t, 6H, –$CH_2C\underline{H}_2$CN), 3.70 (t, 6H, –C$\underline{H}_2$$CH_2$CN), 3.88 (s, 6H, C–C$\underline{H}_2$–O), 4.43, 4.84 (dd, 4H, –C$\underline{H}_2$–O–C$\underline{H}_2$–)

The monomer of poly(3-ethyl-3-*tert*-butyloxetaneamide) (PtBuOA), 3-ethyl-3-*tert*-butyloxetaneamide (tBuOA) was synthesized through the condensation reaction of EOC and *tert*-butylamine (Tokyo Chemical Industry Co., Ltd).

ECO (8.07 g), *tert*-butylamine (6.91 g), EDC·HCl (15.45 g), and DMAP (3.28 g) was

dissolved into dichloromethane (200 mL), then stirred at room temperature for 24 h. The solution was neutralized and purified following the same procedure as 3CEOA. Yield: 51 %

^{1}H NMR (δ, ppm from trimethylsilane (TMS) in $CDCl_3$): 0.91 (t, 3H, –$CH_2C\underline{H}_3$), 1.38 (s, 9H, –C–($C\underline{H}_3$)$_3$), 1.99 (q, 2H, –$C\underline{H}_2CH_3$), 4.40, 4.83 (dd, 4H, –$C\underline{H}_2$–O–$C\underline{H}_2$–), 5.21 (s, 1H, –N$\underline{H}$)

Polymer synthesis

poly(N-(tri((2-cyanoethoxy)methyl)methyl)-3-ethyloxetane-3-carboxamide) (P3CEOA) and poly(N-(tert-butyl)-3-ethyloxetane-3-carboxamide) (PtBuOA) were synthesized via ring-opening cationic polymerization using boron trifluoride diethyl etherate (BF_3・Et_2O, Wako Pure Chemical Co.) as an initiator. The molar ratio of the monomer to the initiator was adjusted to 20:1. Corresponding monomer, N-(tri((2-cyanoethoxy)methyl)methyl)-3-ethyloxetane-3-carboxamide (3CEOA) for P3CEOA and N-(tert-butyl)-3-ethyloxetane-3-carboxamide (tBuOA) for PtBuOA were synthesized through the condensation reaction of 3-ethyloxetane-3-carboxylic acid (EOC) with 3,3'-((2-amino-2-((2-cyanoethoxy)methyl)propane-1,3-diyl)bis(oxy))dipropanenitrile (3CE) and *tert*-butylamine (Tokyo Chemical Industry Co., Ltd), respectively, following reported procedure[1] (see Supporting Information). The initiator was added to the solution of monomer (1.0 g for tBuOA and 4.0 g for 3CEOA) dissolved in dichloroethane (6.0 mL for tBuOA and 4 mL for 3CEOA) and

stirred for 72 h. The polymerization was performed under Ar atmosphere at room temperature. The reaction was quenched using 4 M NaCl/ 1 M NaOH (Wako Pure Chemical Co.) aqueous solution. The solution was extracted with dichloromethane and water, and volatile dichloromethane was removed using a rotary evaporator. The residual viscous solution was dissolved into 10 mL of dichloromethane for each polymer and the solution was slowly poured into 500 mL of hexane for PtBuOA and ethanol for P3CEOA to precipitate the polymerized tBuOA and 3CEOA. The final products were obtained after dried at 100°C under vacuum for over 48 h (Yield: 21 % for PtBuOA and 22 % for P3CEOA). The chemical structures and ^{1}H NMR spectra of PtBuOA and P3CEOA are shown in **Figures 1.1** and **1.2**, respectively. The molecular weight of PtBuOA and P3CEOA were obtained by a gel permeation chromatography, confirming comparable molecular weight for these two polymers (**Table 1.1**).

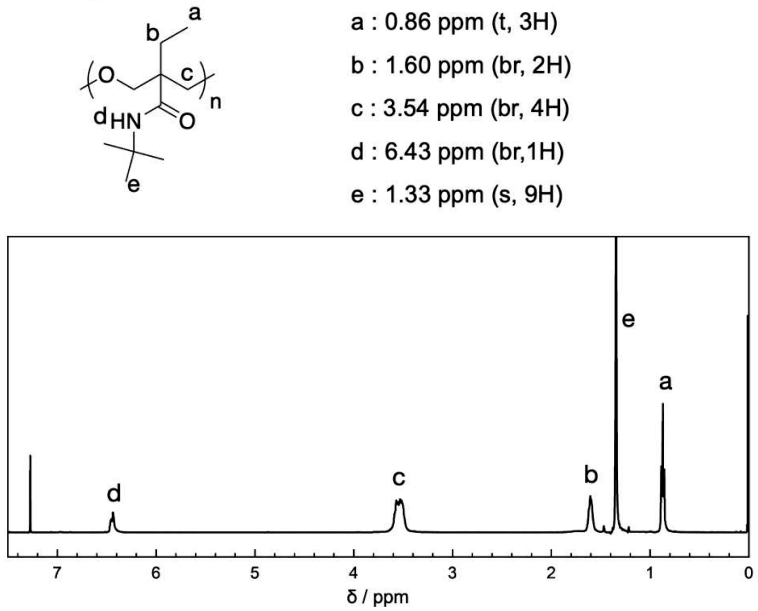

Figure 1.1 ^{1}H NMR spectra of PtBuOA in deuterated dichloromethane.

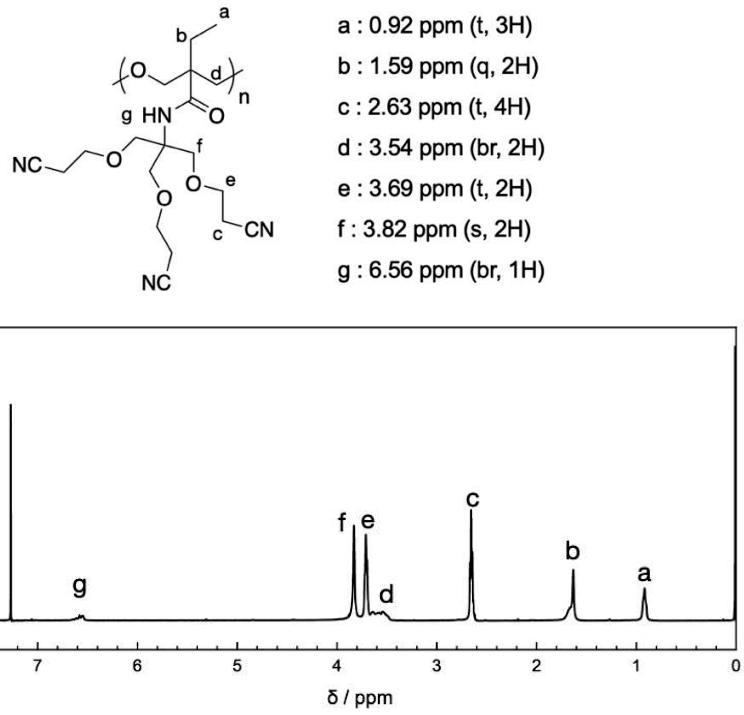

Figure 1.2 ^{1}H NMR spectra of P3CEOA in deuterated dichloromethane.

Table 1.1 Molecular weights (M_n and M_w) and polydispersity index (M_w/M_n) of PtBuOA and P3CEOA.

Polymer	Molecular weight		
	M_n /kg mol^{-1}	M_w /kg mol^{-1}	M_n/M_w /-
PtBuOA	12.6	23.0	1.83
P3CEOA	10.1	23.6	2.34

Electrolyte preparation

Polymer electrolytes were prepared by mixing PtBuOA or P3CEOA and 1 M lithium bis(trifluoromethanesulfonyl)amide (LiTFSA, Tokyo Chemical Industry Co., Ltd.) in tetrahydrofuran (THF). The mixtures were subsequently heated under a vacuum to remove the THF. The molar ratio of LiTFSA to the number of polar groups per unit is represented as x (x = 64, 32, 16, 8, 2.4, and 0.8) for PtBuOA$_x$LiTFSA and P3CEOA$_x$LiTFSA.

Characterization Methods

Proton nuclear magnetic resonance (^{1}H NMR) spectra of the synthesized polymers were obtained by a Fourier transform NMR spectrophotometer (JNM-LA500, JEOL). The molecular weight of the polymer was identified by a gel permeation chromatography (GPC) system (CBM-20A, LC-20AD, DGU-20A, CTO-20A, and RID-10A, Shimadzu) using THF as the elution solvent and polystyrene standards to calibrate the columns. A differential scanning calorimeter (DSC7020, HITACHI) was

used to obtain the glass transition temperature (T_g) of pure polymers and corresponding electrolytes. Approximately 10 mg of polymer materials were hermetically sealed in an aluminum DSC pan inside an Ar-filled glovebox. The samples were first heated to 100°C, and then cooled to –50 °C, and re-heated to 100°C at a rate of 10°C min^{-1}. The second heating scan was recorded as the DSC thermogram of the samples.

Attenuated total reflection infrared (ATR-IR) spectra of the pure polymers and the corresponding electrolytes were obtained using a Nicolet iS50 (Thermo Fisher Scientific) spectrometer equipped with a single-reflection ATR accessory (Smart iTX, Thermo Fisher Scientific) with a ZnSe prism at an incident angle of 45°. Samples were dropped on the ZnSe prism and hermetically sealed by a glass plate with a rubber spacer (thickness, 5 mm) in an Ar-filled glovebox to avoid moisture absorption. The measurements were performed in the 4000 – 600 cm^{-1} spectral range at a 4 cm^{-1} resolution; 32 scans were averaged. The obtained spectra were deconvoluted by PeakFit software (version 4.12, SYSTAT) using a pseudo-Voigt function.

Electrochemical Measurements

The ionic conductivity of the polymer electrolytes was obtained by electrochemical impedance spectroscopy (EIS) using a potentio-galvanostat (SP-150, Bio-Logic) in the frequency range of 1 Hz to 500 kHz. The conductivity cell (Swagelok two-electrode cell) was consisted of polymer electrolyte inserted between two stainless steel electrodes, separated by a poly(tetrafluoroethylene) ring spacer. The cell was

thermally equilibrated in the temperature cabinet at each temperature (50 – 150°C) for at least 1 h before the measurements. The conductivity was calculated by equation (1).

$$\sigma = l / (R_2 \cdot A) \qquad (1)$$

Here, l is the thickness of the electrolyte, R_2 is the bulk resistance obtained from the Nyquist plot, and A is the surface area of the electrolyte calculated from the inner diameter of the ring spacer.

1.3 Results and discussion

Segmental mobility

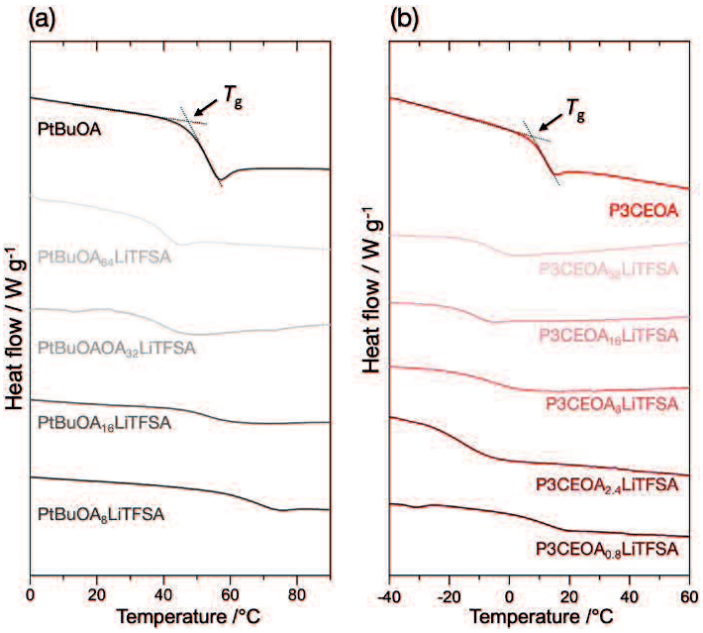

Figure 1.3 Differential scanning calorimetry (DSC) curves for PtBuOA and P3CEOA and the corresponding electrolyte, PtBuOA$_x$LiTFSA and P3CEOA$_x$LiTFSA (x = 0.8 − 64), obtained from –50 to 100°C at a heating rate of 10°C min^{-1}.

To reveal the effect of sterically hindered cyanoethoxy group on segmental mobility of the pure polymer and the corresponding electrolytes (x = 0.8 − 64), glass transition temperature (T_g) of PtBuOA, P3CEOA, and corresponding electrolytes were determined by the differential scanning calorimetry (DSC) (**Figure 1.3** The T_g analysis suggests that the (1) hydrogen bond network and (2) dipole interaction within the polymer act as a pseudo-crosslinking and dictates the polymer segmental mobility, which can be significantly

reduced by the introduction of sterically hindered cyanoethoxy groups as well as the addition of Li salt into the system.

The glass transition temperature (T_g) is tied to the polymer segmental mobility, which is one of the critical descriptors to determine the ion transport property for polymer electrolyte[2]. Glass transition temperature of PtBuOA and P3CEOA, obtained from the inflection point of the DSC curve, was 48.4°C and 9.4°C, respectively, both of which were higher than that of polyethylene oxide (–64°C)[3] reported previously. Notably high T_g for PtBuOA and P3CEOA indicates the existence of strong intra/intermolecular interaction, which effectively restricts the polymer bond rotation required for the smooth segmental motion[4]. We here propose that the hydrogen bond network plays a significant role in determining the polymer segmental mobility for PtBuOA and P3CEOA having secondary amide within the structure. The C=O/COC and NH dipoles within the polymer structure act as hydrogen bond acceptors and donors, respectively, which allows it to form a hydrogen bonding network; the oxygen atom can accept, and the NH hydrogen atoms can donate hydrogen bonds[5]. The considerably low T_g for P3CEOA compared to PtBuOA thus suggests the inhibition of the hydrogen bond network formation, probably due to the large steric hindrance of the cyanoethoxy group. Glass transition temperature decreased by adding Li salt in both systems (until x = 32 and x = 2.4 for PtBuOA and P3CEOA systems, respectively); the opposite is usually the case for most of the polymer electrolyte[6]. We here propose that the observed improvement in segmental mobility may arise from the breakage of the hydrogen bond network by Li salt, due to the interaction between polar group and Li/anion. Similar phenomenon was found in the H-bonding SPE systems[7].

Furthermore, considerable T_g difference between polymer and the corresponding electrolyte (ΔT_g) (e.g., ΔT_g = 7.8°C and 26.9°C for PtBuOA and P3CEOA systems, respectively, under x = 16 condition) as well as the continuous decrease of T_g until higher salt concentration (e.g., T_g started to increase at x = 16 for PtBuOA while T_g of P3CEOA electrolyte continued to decrease until x = 2.4) for P3CEOA systems indicates the existence of additional factor improving the segmental mobility. We propose that the relaxation of the dipole interaction, namely CN…CN, by Li salt significantly improves the segmental mobility for the P3CEOA electrolyte. A similar phenomenon has been reported for the polyacrylonitrile (PAN)[8] and polyethylene carbonate (PEC)-based electrolyte[9], where the replacement of the dipole interaction with the relatively loose dipole…Li^+ interaction contributes to the improved segmental mobility of the polymer[9]. Therefore, the introduction of the sterically hindered cyanoethoxy group improves the segmental mobility of polymer electrolyte by inhibiting hydrogen bonding and forming a loosely bound cyano-Li^+ network within the structure.

Intermolecular interaction in pure polymer

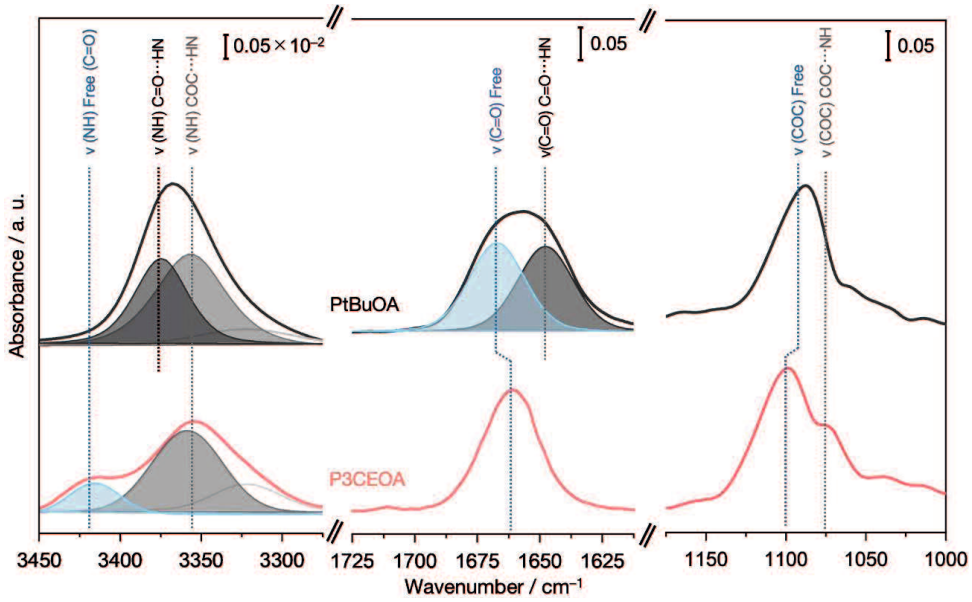

Figure 1.4 Infrared (IR) spectra and typical curve-fitting results of pure PtBuOA (top) and pure P3CEOA (bottom) at room temperature. Peak deconvolution was performed by PeakFit software using pseudo-Voigt functions with a fixed full-width at half-maximum; free peak (Blue), COC…NH (Gray), C=O…NH (Black).

Infrared spectroscopy revealed the intermolecular interaction within pure PtBuOA and P3CEOA, which confirms that the secondary amide group in the side-chain is responsible for forming a hydrogen bond network. The NH group in the PtBuOA side-chain comprises two types of hydrogen bonds (C=O…NH and COC…NH), while the introduction of the cyanoethoxy group selectively inhibits the C=O…NH formation (**Figure 1.4**).

Infrared (IR) spectra of PtBuOA showed a broad peak at *ca.* 3375 cm^{-1}, which can be assigned to the NH stretching vibration (ν(NH)) of PtBuOA[5]. A broad feature indicates

the existence of the multiple intermolecular interactions involving the NH group, which can be deconvoluted into two peaks. We assigned those deconvoluted peaks to the NH group interact with ether oxygen (3357 cm^{-1}) and with carbonyl oxygen (3375 cm^{-1})[10]. Because of the greater electronegativity of an oxygen atom, hydrogen bonds donated from the NH group preferably accepted by the oxygen atom within the ether and carbonyl group. The larger donor number of the ether group than that of the carbonyl group leads to the stronger COC…NH interaction, which may shift the ν(NH) involved in COC…NH interaction to lower wavenumber. An intense peak was observed at the ν(COC) region, which can be assigned to the free ether group and/or ether group interacting with NH, based on the assignment of the ν(NH) region.

The assignment of C=O…NH peak was further supported by the analysis of the peak observed at around 1650 cm^{-1}, which was originated from the C=O stretching vibration (ν(C=O)) of PtBuOA. The C=O stretching peak can be deconvoluted into two peaks, which can be assigned to the free carbonyl group (1670 cm^{-1}) and carbonyl group interact with NH (1648 cm^{-1}). The assignment was supported by analyzing the infrared spectra of PtBuOA dissolved in THF, a condition where most of the intermolecular interaction within the polymer can be relaxed (**Figure 1.5**). The disappearance of the peak at 1648 cm^{-1} was confirmed for PtBuOA dissolved in THF, while the free carbonyl peak at 1670 cm^{-1} remained unchanged (**Figure 1.5(a)**). The selective disappearance of the peak at 1648 cm^{-1} strongly indicates the relaxation of C=O…NH interaction by dissolving PtBuOA in THF. The IR peak analysis confirmed that two types of hydrogen bonds (C=O…NH and COC…NH) were responsible for

the hydrogen bonding network in PtBuOA, which can be the reason for the high T_g of pure PtBuOA.

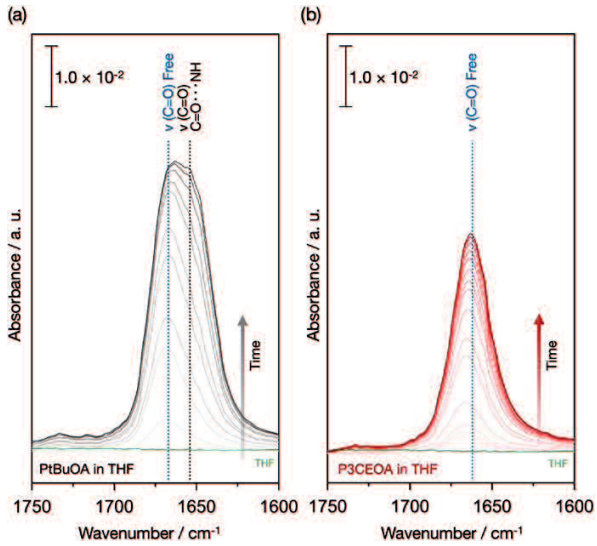

Figure 1.5 Infrared (IR) spectra of C=O stretching for (a) PtBuOA and (b) P3CEOA where the polymer dissolved into THF at room temperature. Each polymer was first completely dissolved into THF (bottom peak), then dried for 1 h under ambient pressure during IR measurement (in order from the bottom to top). IR spectra for THF (green line) is also shown for comparison.

A shouldered peak was observed at *ca.* 3375 cm^{-1} for P3CEOA, which can be originated from the NH stretching vibration (ν(NH)) of P3CEOA (**Figure 1.4**). The deconvoluted peak at 3360 cm^{-1} is ascribable to the NH group interact with the ether group, consistent with the assignment of pure PtBuOA. The deconvoluted peak at a notably high wavenumber of 3423 cm^{-1} was not observed for PtBuOA, and can be assigned to free NH group next to the free C=O[10, 11]. A shouldered peak was observed at the ν(COC) region, indicating the existence of both free ether group and ether group interacting with NH (COC…NH). A sharp peak was observed at 1662 cm^{-1} for

P3CEOA, which can be originated from the C=O stretching vibration (ν(C=O)) of the free carbonyl group in P3CEOA. The assignment was further confirmed by the (i) small full-width at half-maximum (FWHM) value (24 cm^{-1}) as well as (ii) no visible change observed by dissolving P3CEOA in THF (**Figure 1.5(b)**). The observation of free carbonyl (1662 cm^{-1}) and free NH (3423 cm^{-1}) for P3CEOA strongly indicates the effective inhibition of the hydrogen bond formation between C=O and NH by the introduction of bulky cyanoethoxy groups. The improved segmental mobility observed for pure P3CEOA compared to pure PtBuOA (**Figure 1.3**) thus attributable to the partial breakage of the hydrogen bond network by the existence of bulky cyanoethoxy groups.

Intermolecular interaction in polymer electrolytes

Infrared spectra analysis revealed that the addition of Li salt effectively relaxes the intermolecular interactions responsible for the formation of the hydrogen bond network (C=O…NH and COC…NH for PtBuOA and COC…NH for P3CEOA). Furthermore, in the case of the P3CEOA system, dipole interaction between two CN groups was also replaced by the CN…Li^+ interaction, which contributed to the further improvement in the segmental mobility of P3CEOA electrolyte (**Figures 1.6, 1.7**)

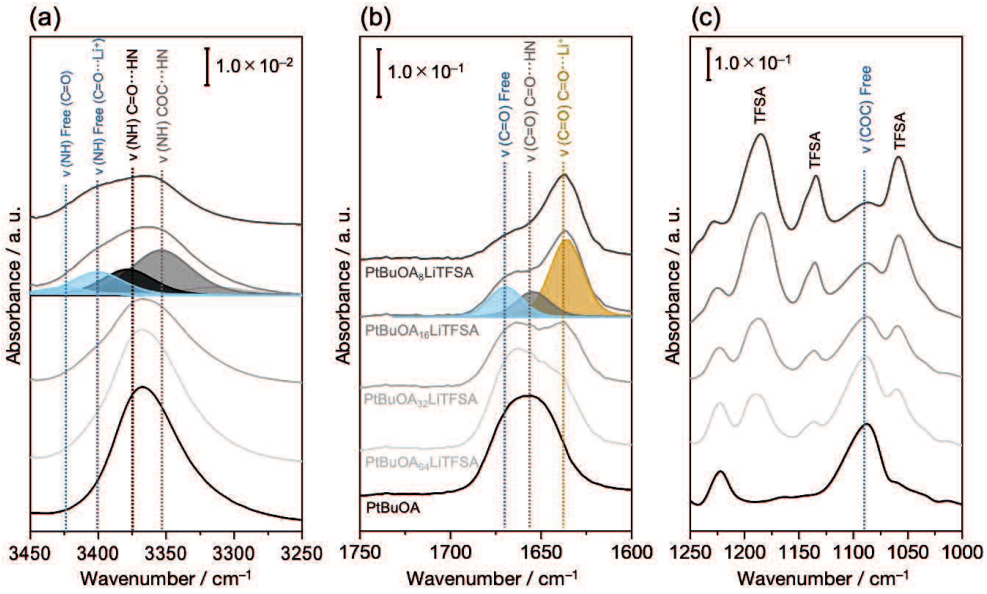

Figure 1.6 Infrared (IR) spectra and typical curve-fitting results of (a) N-H stretching, (b) C=O stretching, and (c) C-O-C stretching region for pure PtBuOA and PtBuOA$_x$LiTFSA (x = 8 − 64) at room temperature. Peak deconvolution was performed by PeakFit software using pseudo-Voigt functions with a fixed half-width at half-maximum; free peak (Blue), COC…NH (Gray), C=O…NH (Black), C=O…Li$^+$ (Yellow).

A broad-shouldered feature at *ca.* 3375cm^{-1} was observed for PtBuOA$_{16}$LiTFSA, which can be deconvoluted into four major peaks (**Figure 1.6(a)**). The peak at *ca.* 3350 cm^{-1} and 3370 cm^{-1} agrees well with the peak observed for pure PtBuOA, which corresponds to the NH interacting with carbonyl oxygen and ether oxygen, respectively. The additional peak at a notably large wavenumber of *ca.* 3400 cm^{-1} can be assigned to free NH next to C=O interact with Li$^+$, since (i) the corresponding peak did not appear in the pure P3CEOA and (ii) the intensity increased with the salt concentration. The small peak at *ca.* 3425 cm^{-1} can be assigned to free NH next to free C=O, which is consistent with the assignment of pure P3CEOA (**Figure 1.4**). The

relative intensity of the free NH peak increased with increasing salt concentration, which implies a partial breakage of the hydrogen bond network (e.g., C=O…NH and COC…NH) by the addition of Li salt.

The breakage of the hydrogen bond network for PtBuOA electrolyte was further supported by the analysis of the C=O stretching region (**Figure 1.6(b)**). The C=O stretching feature of PtBuOA electrolyte showed a shouldered peak consist of three peaks; two of which are ascribable to free carbonyl group (1670 cm^{-1}) and carbonyl group interact with NH (1655 cm^{-1}) based on the assignment of pure PtBuOA. An intense new peak at 1636 cm^{-1} was assigned to carbonyl group bound with Li^+, since oxygen atom with large electronegativity preferably interacts with positively charged Li^+ than non-coordinative $TFSA^-$[12]. The 1636 cm^{-1} peak became the dominant component under high salt concentration conditions ($x < 16$), which agrees well with our assignment. Negligible change in the ν(COC) feature of ether oxygen at *ca.* 1090 cm^{-1} by the addition of Li salt indicated no COC…Li^+ interaction, which confirms the strong preference of Li^+ interacting with carbonyl oxygen instead of ether oxygen (**Figure 1.6(c)**). The GC-MS measurement further supports the existence of C=O…Li^+ interaction (**Figure 1.7**). Thermal stability of the polar group is greatly affected by the interaction with Li^+ due to the weakening of the bond caused by the electron deficiency of the polar group[13]. The decomposition temperature of the amide group indeed decreased for *ca.* 70°C by the addition of Li salt, which confirms the existence of C=O…Li^+ interaction (**Figure 1.7**). We propose that carbonyl oxygen preferably interacts with Li^+ than hydrogen atom in the NH group, decreasing the number of carbonyl group involved in the hydrogen bond network. The breakage of

hydrogen bond network by substituting C=O…NH interaction with C=O…Li^+ thus contributed to the remarkable improvement in the segmental mobility of PtBuOA by the addition of Li salt.

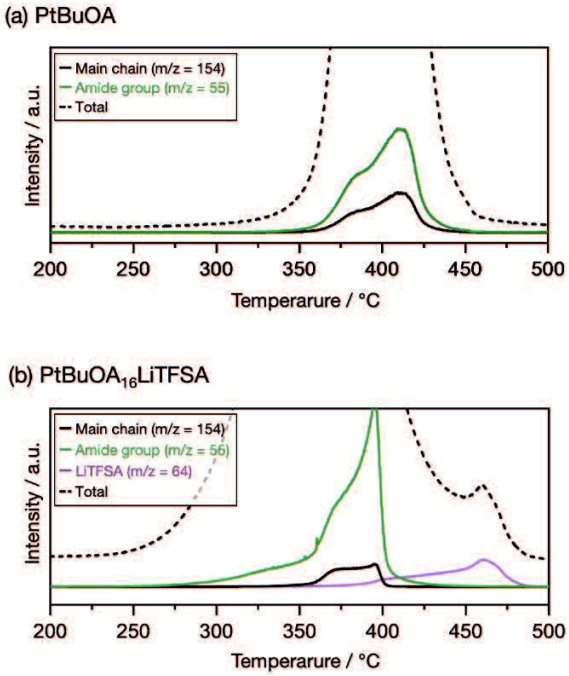

Figure 1.7 Gas chromatography–mass spectrometry (GC-MS) analysis for pristine (a) PtBuOA and (b) $PtBuOA_{16}LiTFSA$ electrolytes. GC-MS curve was obtained by heating from 100°C to 500°C at a heating rate of 20°C min^{-1} under air. A gas chromatography–mass spectrometry (GC-MS) spectra were obtained by a gas chromatograph−mass spectrometer (GCMS-QP2010 Ultra, Shimadzu). A small amount of polymer electrolytes (~5 mg) was put in an aluminum pan. The samples were then pre-heated to 150 °C and held for 10 min to remove the residual water.

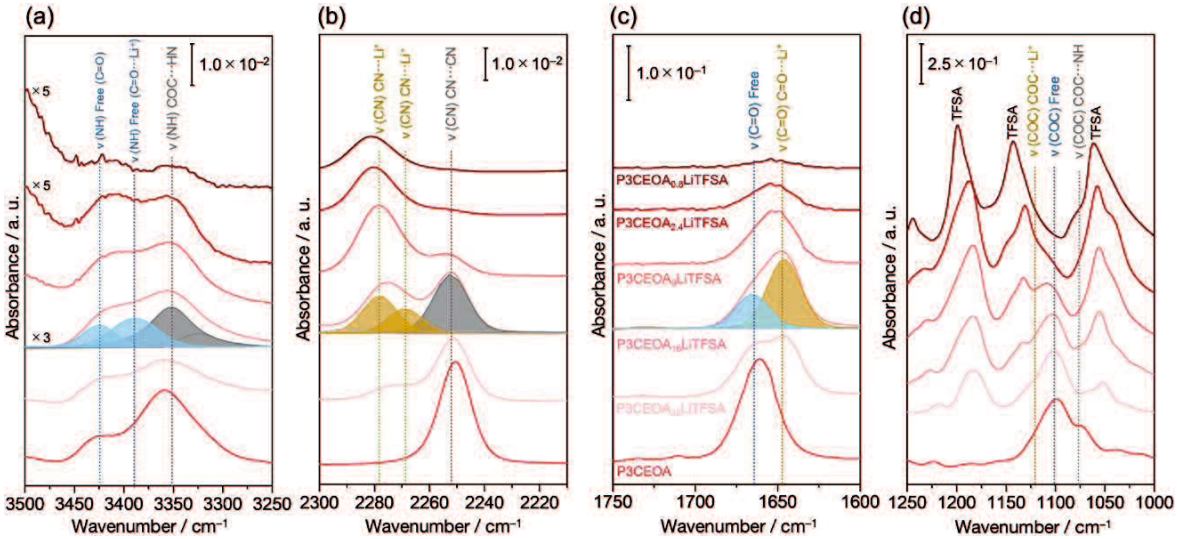

Figure 1.8 Infrared (IR) spectra and typical curve-fitting results of (a) N-H stretching, (b) C≡N stretching, (c) C=O stretching, and (d) C-O-C stretching region for pure P3CEOA and P3CEOA$_x$LiTFSA (x = 0.8 − 32) at room temperature. Peak deconvolution was performed by PeakFit software using pseudo-Voigt functions with a fixed half-width at half-maximum; free peak (Blue), COC…NH (Gray), C=O…NH (Black), C=O/CN…Li$^+$ (Yellow).

The broad ν(NH) peak at *ca.* 3375cm^{-1} for P3CEOA electrolyte can be deconvoluted into three major components at 3350cm^{-1}, 3390 cm^{-1}, and 3425 cm^{-1} (**Figure 1.8(a)**). The peak at 3350 cm^{-1} and 3425 cm^{-1} corresponds to NH interact with ether group and free NH next to free C=O, respectively, which is consistent with the assignment of pure P3CEOA. The peak at 3390 cm^{-1} can be assigned to the free NH attached to C=O interacting with Li$^+$, which is in agreement with the assignment of PtBuOA electrolyte (**Figure 1.6**). The notable increase in the intensities of the peaks of the free NH and the NH interact with Li$^+$ especially at a high salt concentration (x < 16) suggest the breakage of hydrogen bonding network by the addition of LiTFSA in P3CEOA electrolyte, similar to that of PtBuOA. The ν(C=O) peak for P3CEOA electrolyte can

be deconvoluted into two peaks, 1648 cm^{-1} and 1665 cm^{-1}, and the latter agrees well with the free carbonyl peak observed for pure P3CEOA (**Figure 1.8(c)**). The intense peak at *ca.* 1648 cm^{-1} ascribable to the carbonyl group interacting with Li^+, since (i) the intensity of the corresponding peak showed salt concentration dependency as well as (ii) the decrease in the thermal stability was confirmed for $P3CEOA_{16}LiTFSA$ by GC-MS analysis (**Figure 1.9**). The existence of carbonyl group interacting with Li^+ further validates the assignment of ν(NH) region. The analysis of the COC stretching region indicates the breakage of the hydrogen bond network for the P3CEOA electrolyte by substituting COC…NH interaction (ca. 1075 cm^{-1}) with COC…Li^+ interaction (ca. 1170 cm^{-1}) (**Figure 1.8(d)**).

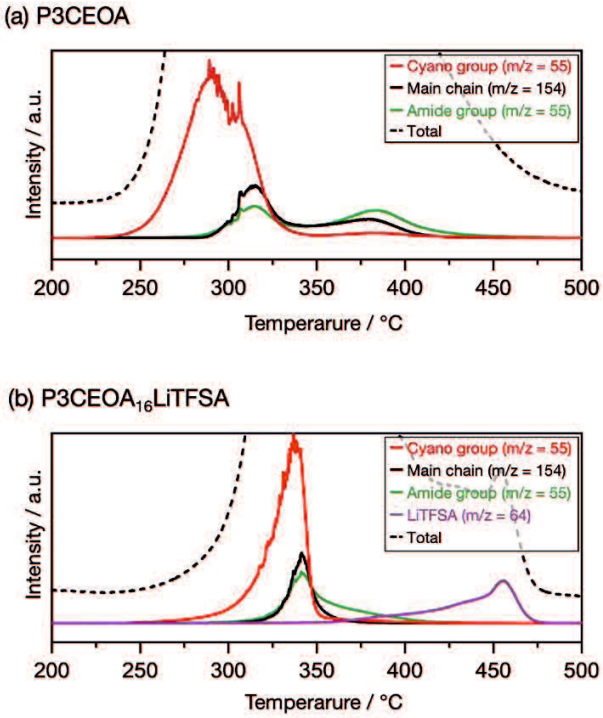

Figure 1.9 Gas chromatography–mass spectrometry (GC-MS) analysis for pristine (a) P3CEOA and (b) P3CEOA$_{16}$LiTFSA. GC-MS curve was obtained by heating from 100°C to 500°C at a heating rate of 20°C min^{-1} under air. A gas chromatography–mass spectrometry (GC-MS) spectra were obtained by a gas chromatograph−mass spectrometer (GCMS-QP2010 Ultra, Shimadzu). A small amount of polymer electrolytes (~5 mg) was put in an aluminum pan. The samples were then pre-heated to 150 °C and held for 10 min to remove the residual water.

A sharp peak at *ca.* 2250 cm^{-1} corresponds to the CN stretching vibration (ν(CN)) of pure P3CEOA[14](**Figure 1.8(b)**). We here assigned the peak at 2250 cm^{-1} to CN interact with CN, based on the previous findings suggesting that the functional group with large dipole moment (e.g., CN) tend to interact with each other, via so-called dipole interaction[15,16]. The substitution of dipole interaction between two cyano groups with CN…Li^+ interaction was suggested by observing a new peak at 2270 and 2278 cm^{-1} for P3CEOA electrolyte, which is originated from CN interacted with Li^+[17]. The assignment was further supported by the GC-MS measurement, where the thermal stability of the cyano group was decreased by the addition of Li salt (**Figure 1.9**).

We propose that the dipole interaction between the polar cyano groups play a significant role in the unique salt concentration dependence of T_g due to the following reasons: The dipole interaction increase the cohesive energy of P3CEOA[18], consistent with its relatively high T_g compared to PEO-counterparts[3]. The replacement of the structurally restricted dipole interaction by more flexible interaction, e.g., CN…Li^+ interaction, can increase the segmental mobility under the existence of Li salt. Our hypothesis is further confirmed by comparing the T_g of P3CEOA with that of the polymer having two cyanoethoxy groups (**Table 1.2**). The T_g for P3CEOA (9.4°C) was higher than that of P2CEOA (0.2°C), suggesting dipole interaction between two cyano groups act as a pseudo-crosslinking, which effectively decreases the segmental mobility of the polymer with a large amount of cyano group within the structure.

We thus conclude that the breakage of the hydrogen bonding network is one of the keys for the characteristic improvement of the segmental mobility under the existence

of Li salt for PtBuOA and P3CEOA systems. The relaxation of dipole interaction between two polar cyano groups by Li^+ contributes to the further improvement in the segmental mobility for P3CEOA electrolytes.

Table 1.2 The T_g value of PtBuOA*x*LiTFSA, P2CEOA*x*LiTFSA and P3CEOA*x*LiTFSA (x = 64–0.8).

x	T_g /°C		
	PtBuOA	P2CEOA	P3CEOA
(pure)	48.4	0.2	9.4
x = 64	31.2	-	-
x = 32	26.2	–0.4	–15.9
x = 16	40.6	–15.8	–17.5
x = 8	57.8	–12.9	–20.9
x = 2.4	-	–24.6	–24.4
x = 0.8	-	-	2.3

Ion transport properties

The ionic conductivity of PtBuOA and P3CEOA electrolytes was obtained by electrochemical impedance spectroscopy (EIS), confirming the introduction of the cyanoethoxy group improved the ionic conductivity (**Figure 1.10**). The improved ionic conductivity can be rationalized by the high segmental mobility (better long-range Li^+ conduction) and optimized stability of the Li^+ coordination structure (better short-range Li^+ conduction) for P3CEOA electrolyte.

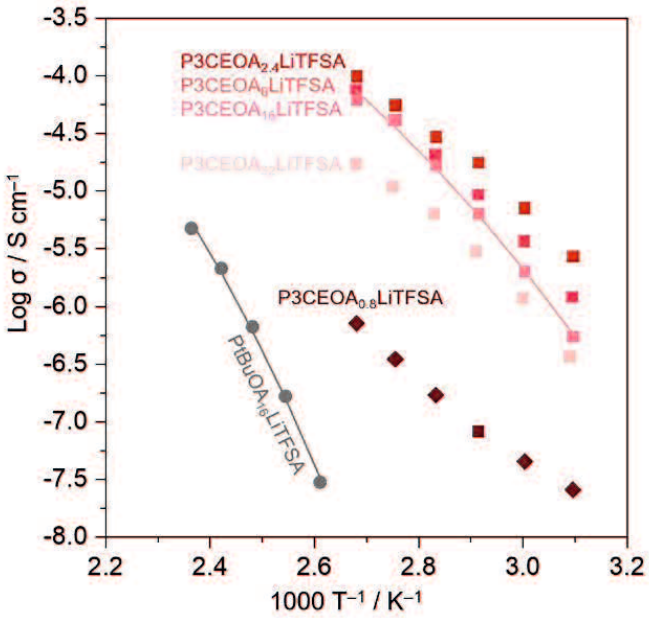

Figure 1.10 Arrhenius plots of the ionic conductivity for $PtBuOA_{16}LiTFSA$ and $P3CEOA_xLiTFSA$ (x = 0.8 − 32). The electrochemical impedance spectroscopy was performed at 110 − 150°C and 50 − 100°C for PtBuOA and P3CEOA systems, respectively, due to the low ionic conductivity of PtBuOA. The solid line represents the Vogel-Tammann-Fulcher (VTF) fitting curves.

The Arrhenius plots of the ionic conductivity for PtBuOA electrolytes confirmed the significantly low ionic conductivity of PtBuOA electrolyte, mainly due to the low segmental mobility (high T_g value of 40.6°C) derived from the hydrogen bond network within the electrolyte (**Figure 1.4**). The ionic conductivity of the P3CEOA electrolyte was much higher than that of PtBuOA$_{16}$LiTFSA throughout the temperature range tested. The salt concentration dependency of the ionic conductivity of P3CEOA electrolyte followed the order of the T_g value (T_g: $x = 32 > x = 16 > x = 8 > x = 2.4$), suggesting that the segmental mobility (T_g) dictates the ionic conductivity of those electrolyte. The Arrhenius plots of each electrolyte indeed well-fitted with Vogel-Tammann- Fulcher (VTF) equation (equation (1)), further indicates that the ionic conductivity in both electrolytes heavily depends on their segmental mobility. The VTF equation can be described as follows.

$$\sigma = AT^{-1/2}\exp\{(-B)/R(T-T_0)\} \quad \ldots \text{Equation (1)}$$

where A is a parameter of the number of charge carriers, B is the pseudo activation energy of ionic transportation, R is the gas constant, and T_0 is an ideal glass transition temperature ($T_0 = T_g - 50$ K [19, 20]).

Table 1.3 The parameters of Vogel-Tammann-Fulcher (VTF) equation (A and B) for PtBuOA$_{16}$LiTFSA and P3CEOA$_{16}$LiTFSA obtained from **Figure 1.10**.

	PtBuOA$_{16}$LiTFSA	P3CEOA$_{16}$LiTFSA
A [S cm^{-1} K$^{1/2}$]	478.7	184.1
B [kJ mol^{-1}]	20.1	16.6

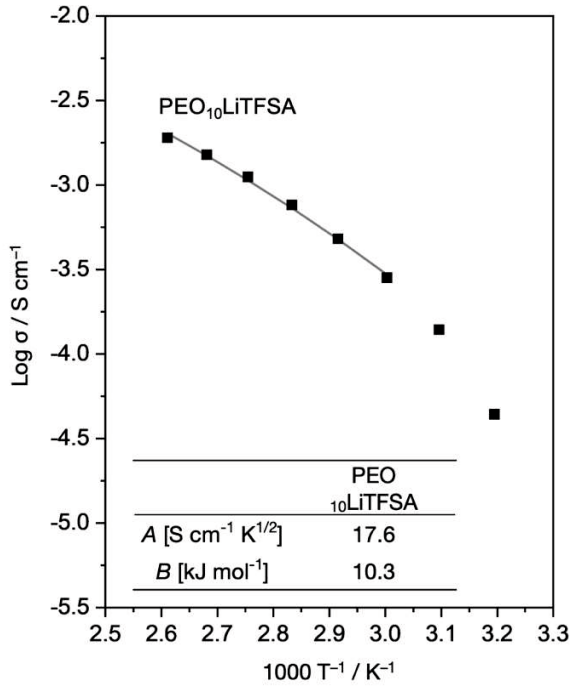

Figure 1.11 Arrhenius plots of the ionic conductivity for PEO_{10}LiTFSA. The electrochemical impedance spectroscopy was performed at 10 – 110°C. The solid line represents the Vogel-Tammann-Fulcher (VTF) fitting curves and the fitting parameters (*A* and *B*) for PEO_{10}LiTFSA were shown in the inset.

The number of charge carriers (*A* values) for $PtBuOA_{16}$LiTFSA (478.7 S cm^{-1} $K^{1/2}$) and $P3CEOA_{16}$LiTFSA (184.1 S cm^{-1} $K^{1/2}$) was higher than that of widely studied PEO electrolytes (17.6 S cm^{-1} $K^{1/2}$) (**Figure 1.11**), suggesting better dissociation of the Li salt in both PtBuOA and P3CEOA electrolytes. The improved salt dissociation for PtBuOA and P3CEOA electrolytes could be originated from the higher dielectric constant of the polymer, which is mainly arisen from the existence of the hydrogen bond network in PtBuOA and P3CEOA. The dielectric constant of the polymer tends to become higher along with the increase of the hydrogen bond network[21]. The number

of charge carriers (*A* values), a simple measure of the salt dissociability, indeed decreased for P3CEOA$_{16}$LiTFSA (184.1 S cm^{-1} K$^{1/2}$) compared to that of PtBuOA$_{16}$LiTFSA (478.7 S cm^{-1} K$^{1/2}$). Relatively low salt dissociation for P3CEOA$_{16}$LiTFSA can be further confirmed by IR measurement, where C-S stretching peaks of P3CEOA started to blueshift at x = 16, suggesting the coordination of Li$^+$ with TFSA (**Figure 1.12**). The above observation suggests the small dielectric constant of P3CEOA compared to that of PtBuOA, which is consistent with the breakage of the hydrogen bond network by the bulky cyanoethoxy group.

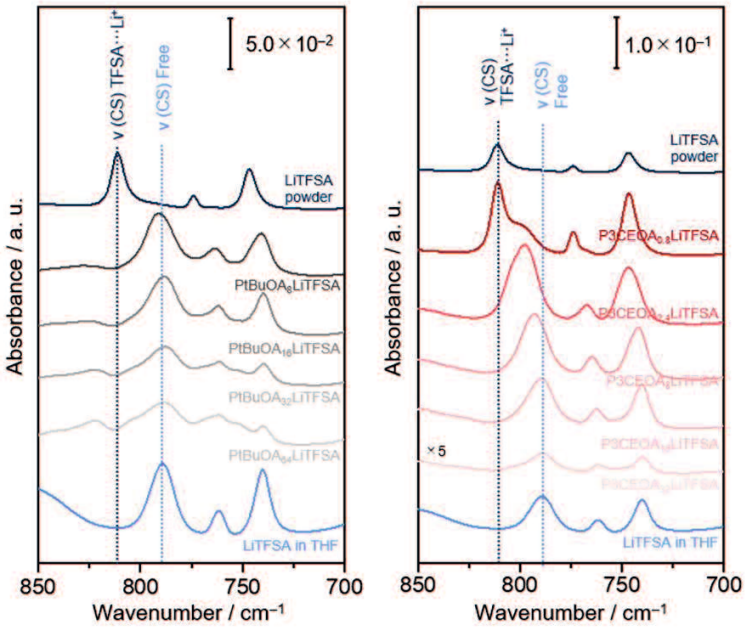

Figure 1.12 Infrared (IR) spectra and typical curve-fitting results of C-S stretching region for (a) pure PtBuOA and PtBuOA$_x$LiTFSA (x = 8 − 64) and (b) pure P3CEOA and P3CEOA$_x$LiTFSA (x = 0.8 − 32) at room temperature. IR spectra for LiTFSA dissolved in THF (bottom) and pure LiTFSA powder (top) is also shown for comparison.

Although the salt dissociability decreased by the introduction of cyanoethoxy side-chain, the pseudo activation energy of ionic transportation (*B* value) of the P3CEOA$_{16}$LiTFSA (16.6 kJ mol^{-1}) was lower than that of PtBuOA$_{16}$LiTFSA (20.1 kJ mol^{-1}), suggesting the improved ion transport in P3CEOA system. According to our previous work, a characteristic co-interaction of the three components (cyano group, ether oxygen, and TFSA anion) with Li^+ play a significant role in accelerating the inter-chain Li^+ transfer (short-range Li^+ conduction)[22] due to the following reasons; The Li^+ coordination structure can be relaxed by a characteristic co-interaction of the cyano group, ether oxygen, and TFSA anion, which stops overly holding onto the Li^+, promoting the inter-chain Li^+ transfer. Furthermore, the characteristic linear structure of the cyano group provide large free volume in the direct vicinity of the Li^+ coordination site, which accelerates intermolecular coordination of Li^+, eventually accelerates Li^+ transfer from one coordination site to another in the presence of an electric field. We confirmed that the Li^+ in P3CEOA system interact with cyano group, ether/carbonyl oxygen, and TFSA anion, which satisfies the aforementioned requirement of accelerating inter-chain Li^+ transfer, resulting in the improved ionic conductivity for P3CEOA electrolytes. Therefore, we confirmed that the introduction of the cyanoethoxy group indeed improves the ionic conductivity due to the high segmental mobility and the optimized Li^+ coordination structure, which contributes to the improved long-range and short-range Li^+ conduction, respectively.

Figure 1.13 summarizes the proposed intermolecular interaction based on the infrared spectra analysis. The hydrogen bond network (consist of C=O…NH and COC…NH interaction) was formed in pure PtBuOA, which strongly inhibit the

segmental motion of the PtBuOA (**Figure 1.13(a)**). The selective substitution of C=O…NH by C=O…Li^+, due to the large dipole of the carbonyl group, partially breaks the hydrogen bond network, leading to improve the segmental motion of the PtBuOA by the addition of Li salt (**Figure 1.13(b)**).

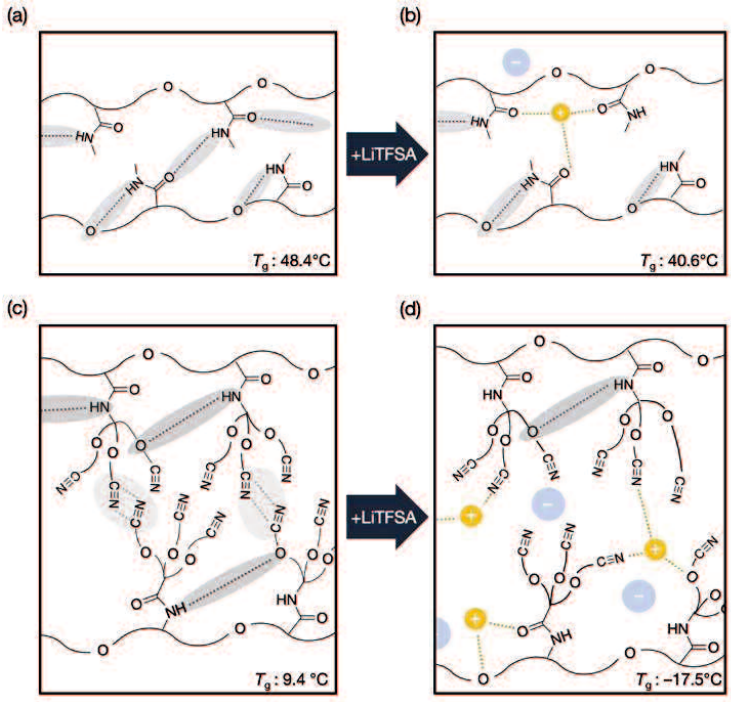

Figure 1.13 Proposed inter/intramolecular interaction within (a) pure PtBuOA, (b) PtBuOA electrolyte, (c) pure P3CEOA, and (d) P3CEOA electrolyte. The large steric hindrance of the cyanoethoxy side-chain effectively suppresses the formation of the hydrogen bond network, by selectively inhibiting the approach of the NH group towards the carbonyl group. The addition of Li salt substitutes both COC…NH and CN…CN interactions (shown in shaded area) by COC… Li^+ and CN… Li^+, respectively, which result in the significant decrease in the T_g.

Two interactions can inhibit the segmental motion of pure P3CEOA; hydrogen bond network via COC…NH interaction and dipole interaction between two polar cyano groups (**Figure 1.13(c)**). The large steric hindrance of the cyanoethoxy side-chain effectively suppresses the formation of C=O…NH, by selectively inhibiting the approach of the NH group towards the carbonyl group. The addition of Li salt substitutes both COC…NH and CN…CN interactions by COC…Li^+ and CN…Li^+, respectively, which result in the significant improvement of the segmental motion (**Figure 1.13(d)**). Furthermore, the Li^+ coordination structure involving cyano group, ether/carbonyl oxygen, and TFSA anion moderately stabilizes the Li^+, which enables smooth transfer of Li^+ between neighboring coordination sites. Therefore, the introduction of the bulky cyanoethoxy group improves the segmental mobility of the polymer by sterically inhibiting the hydrogen bond formation and optimizes the coordination structure of Li^+, both of which contribute to the better ionic conductivity of P3CEOA electrolyte having amide group.

1.4 Conclusions

The effect of introducing branched side-chains with methyl (PtBuOA) and bulky cyanoethoxy group (P3CEOA) on the (electro)chemical properties of polyether-based electrolyte with amide group was elucidated by spectro(electro)chemical analysis. The (1) hydrogen bond network and (2) dipole interaction within the polymer act as a pseudo-crosslinking and dictates the polymer segmental mobility (T_g), which is one of the key descriptors for the ionic conductivity. Infrared spectroscopy revealed that two

types of hydrogen bonds (C=O…NH and COC…NH) were responsible for the high T_g of pure PtBuOA. The introduction of the cyanoethoxy group sterically inhibits the C=O…NH interaction while evoking dipole interaction between two CN groups in pure P3CEOA. Li ion breaks the hydrogen bonding network in PtBuOA and P3CEOA by substituting C=O…NH and/or COC…NH with Li^+-involved interaction (C=O…Li^+ and/or COC…Li^+), which effectively decreases T_g along with the addition of Li salt. Furthermore, the relaxation of CN…CN interaction by Li^+ contributes to further improvement in the segmental mobility of the P3CEOA electrolyte. The ionic conductivity of P3CEOA electrolytes significantly improved compared to that of PtBuOA, which can be fulfilled by the high segmental mobility (better long-range Li^+ conduction) and optimized stability of the Li^+ coordination structure (better short-range Li^+ conduction) derived from the cyanoethoxy group. This work elucidates the effect of the intermolecular interaction network within the polymer on the polymer segmental mobility and the ion transfer properties. Furthermore, the P3CEOA electrolytes achieved unprecedented high conductivity of 10^{-4} S/ cm^{-1} at 100°C for polymers with an amide group, by effectively controlling the intermolecular interaction network via optimizing steric hindrance and selecting the polar group for the side-chains. Therefore, this work emphasizes the importance and the potential of polymers with an amide group as a new class of easy-to-modify electrolyte materials, facilitating the implementation of all-solid lithium-ion batteries.

References

1 Y. Nakano and H. Tsutsumi, *Solid State Ionics*, 2014, **262**, 774–777.

2 M. Armand, *Adv. Mater.*, 1990, **2**, 278–286.

3 J. Y. Song, Y. Y. Wang and C. C. Wan, *J. Power Sources*, 1999, **77**, 183–197.

4 K. Bandzierz, L. Reuvekamp, J. Dryzek, W. Dierkes, A. Blume and D. Bielinski, *Materials*, 2016, **9**, 1–17.

5 M. Digar, S. L. Hung, H. L. Wang, T. C. Wen and A. Gopalan, *Polymer*, 2001, **43**, 681–691.

6 W. H. Meyer, *Adv. Mater.*, 1998, **10**, 439–448.

7 J. Mindemark, B. Sun and D. Brandell, *Polym. Chem.*, 2015, **6**, 4766–4774.

8 Z. Florjańczyk, E. Zygadło-Monikowska, W. Wieczorek, A. Ryszawy, A. Tomaszewska, K. Fredman, D. Golodnitsky, E. Peled and B. Scrosati, *J. Phys. Chem. B*, 2004, **108**, 14907–14914.

9 J. Motomatsu, H. Kodama, T. Furukawa and Y. Tominaga, *Macromol. Chem. Phys.*, 2015, **216**, 1660–1665.

10 E. J. Lee, K. H. Park, Y. H. Lee, K. G. Kim, Y. U. Jeong, S. Y. Kim and H. Do Kim, *J. Appl. Polym. Sci.*, 2017, **134**, 1–9.

11 D. T. McQuade, S. L. McKay, D. R. Powell and S. H. Gellman, *J. Am. Chem. Soc.*, 1997, **119**, 8528–8532.

12 O. Borodin and G. D. Smith, *Macromolecules*, 2006, **39**, 1620–1629.

13 and M. Y. Q. Luigi Costa, Ali M. Gad, Giovanni Camino, G. Gordon Cameron, *Macromolecules*, 1992, **25**, 5512–5518.

14 H. K. Yoon, W. S. Chung and N. J. Jo, *Electrochim. Acta*, 2004, **50**, 289–293.

15 N. Verdier, D. Lepage, R. Zidani, A. Prébé, D. Aymé-Perrot, C. Pellerin, M. Dollé and D. Rochefort, *ACS Appl. Energy Mater.*, 2020, **3**, 1099–1110.

16 R. Sai, K. Ueno, K. Fujii, Y. Nakano and H. Tsutsumi, *RSC Adv.*, 2017, **7**, 37975–37982.

17 B. Huang, *Solid State Ionics*, 1996, **85**, 79–84.

18 R. Sai, K. Ueno, K. Fujii, Y. Nakano, N. Shigaki and H. Tsutsumi, *Phys. Chem. Chem. Phys.*, 2017, **19**, 5185–5194.

19 K. B. M. Isa, Z. Osman, A. K. Arof, L. Othman, N. H. Zainol, S. M. Samin, W. G. Chong and N. Kamarulzaman, *Solid State Ionics*, 2014, **268**, 288–293.

20 Y. Ye and Y. A. Elabd, *Polymer*, 2011, **52**, 1309–1317.

21 M. F. Chaplin, 2007, https://arxiv.org/ abs/0706.1355.

22 R. Matsuoka, M. Shibata, K. Matsuo, R. Sai, H. Tsutsumi, K. Fujii and Y. Katayama, *Macromolecules*, 2020, **53**, 9480−9490.

YAMAGUCHI
UNIVERSITY

Chapter 2

(Electro)chemical processes of poly (ethylene oxide)-based electrolyte on Cu surface during lithium secondary battery operation

2.1 Introduction

The reaction at the electrode and electrolyte interface heavily affects the overall battery performance, including rate capability, cycle life, and safety. The reaction mechanism at the electrode and SPE still remains unclear although its component was partially clarified.

Operando ATR-IR provided the information at the vicinity of the electrode under operating condition, which is considered as the promising tool for understanding the reaction mechanism of electrode/SPE interface. In this work, the reaction of widely used SPE, PEO-LiTFSA electrolyte on the Cu electrode was revealed by combining *operando* ATR-IR and ex-situ XPS. The obtained spectra distinctively showed the decomposed products of not only PEO but also LiTFSA. Furthermore, the correlation between the decomposed species and the surface resistance, the LSV and electrochemical impedance spectroscopy was used. The growth and component change of SEI was confirmed by Nyquist plots obtained at several potential.

2.2 Experimental

Electrolyte preparation

Polymer electrolytes were prepared by mixing poly(ethylene oxide) (PEO, Mn=20,000, Wako Pure Chemical) and 1 M lithium bis(trifluoromethanesulfonyl)amide (LiTFSA, Tokyo Chemical Industry Co., Ltd.) in tetrahydrofuran (THF, Tokyo Chemical Industry Co., Ltd.) at 80°C. The molar ratio of LiTFSA to ether oxygen unit was 1:10 and is represented as

PEO_{10}LiTFSA. The mixtures were subsequently heated at 80°C under a vacuum to remove the THF for over 24 h.

IR spectroscopy

Attenuated total reflection infrared (ATR-IR) spectra of PEO_{10}LiTFSA were obtained on a Nicolet iS50 (Thermo Fisher Scientific) spectrometer with a single-reflection ATR accessory (Smart iTX, Thermo Fisher Scientific). The spectra were acquired in the single-reflection mode equipped with deuterated triglycine sulfate (DTGS) detector at an incident angle of 45 degrees. The spectral resolution was 4 cm^{-1} and 32 scans were averaged. Samples were dropped on the Ge ATR prism and hermetically sealed by a glass plate with a rubber spacer (thickness, 5 mm) in an Ar-filled glovebox.

Operando ATR-IR measurements were conducted during liner sweep voltammetry. The operando ATR-IR spectra were obtained at an incident angle of 67 degrees with a Mercury-Cadmium-Telluride (MCT) detector. The spectral resolution was 4 cm^{-1} and 128 scans were averaged. All spectra were presented in the form of absorbance according to $\log(I_0/I_1)$, where I_0 and I_1 are the spectrum of background (Cu surface without electrolytes) and operando spectrum, respectively. Ge hemisphere (φ22 mm, Pier Optics) was used as the optical prism. Cu thin film (thickness ~ 30 nm) was formed on the flat surface of the Ge hemisphere by vacuum sputtering at ~0.6 nm s^{-1}, and was used as both the working electrode and the current collector. Lithium metal foil was used as a counter electrode. PEO_{10}LiTFSA were dropped on the Cu surface, and separated by a poly(propylene) ring spacer (inner diameter, 5.3 mm).

Electrochemical measurement

The electrochemical behavior of the electrodes was confirmed by cyclic voltammetry (CV) in CR2032-type coin cells. All electrochemical measurements were performed on a potentiogalvanostat (SP-150, Bio-Logic). Sputtered Cu (thickness, 100 nm) film and lithium foil (φ10 mm) were used as working electrodes and reference/counter electrodes, respectively. Assembled cells except for operando ATR-IR measurements in this work were thermally annealed for 12 h at 70°C to obtain good contact with electrolyte and electrodes before each

electrochemical measurement. All electrochemical cells were assembled in an argon-filled glovebox (<0.1 ppm of H_2O). CV measurements were performed between 2.8 V_{Li} and -1.0 V_{Li} at a rate of 1 mV/s at 25°C. The formation and growth of the SEI-like layer on the Cu surface were confirmed by LSV and electrochemical impedance spectroscopy. The EIS spectra were collected with an AC amplitude of 10 mV and frequency range of 1 MHz – 1 Hz in two electrode coin-cell (Cu/SPE/Li).

XPS measurements

The X-ray photoelectron spectroscopy (XPS) of the electrode before and after the electrochemical measurement was performed on K-Alpha (Thermo Scientific). A pass energy of 23.5 eV was used, and adventitious carbon at 284.8 eV (C1s spectra) was used to calibrate all XPS spectra. After subtracting a Shirley-type background, the photoemission lines were fitted using combined Gaussian-Lorentzian functions.

To form a decent amount of SEI on the Cu surface, chronoamperometry measurement was carried out in the same cell configuration and procedure as CV measurement. Each cell was held at 1.9, 1.0, 0.8, and 0 V_{Li} for 12 h. The samples were prepared by carefully disassembling the cells in an Ar-filled glove box and then transferring them to the XPS spectrometer with a transfer vessel to avoid contact with moisture and air. Residual electrolytes were washed off from the Cu electrode.

2.3 Results and discussion

Electrochemical reaction of PEO_{10}LiTFSA on Cu electrode

We performed cyclic voltammetry coupled with electrochemical impedance spectroscopy to clarify the reduction behavior of the PEO_{10}LiTFSA and corresponding SEI growth on the Cu surface (**Figure 2.1**). A large reduction and oxidation current observed at around 0 V_{Li} in both 1st and 3rd cycle corresponds to the reversible lithium deposition/dissolution reaction (**Figure 2.1a**).[1, 2] The three reduction current were observed at around 2.1-1.9 V_{Li} (peak at

ca. 2.0 V_{Li}; first peak), 1.9-0.8 V_{Li} (peak at ca. 1.3 V_{Li}; second peak), and 0.8-0 V_{Li} (peak at ca. 0.3 V_{Li}; third peak), which can be corresponded to the reduction of electrolytes, e.g. PEO and/or LiTFSA. Note that the first and second reduction peaks (peaks at 2.0 and 1.3 V_{Li}) disappeared at the second and third cycles, suggesting the corresponding reduction reaction was completely suppressed after 1st cycle. Based on the previous findings[3], we hypothesize that the SEI-like film was formed on the Cu surface via multiple reduction reactions of the electrolyte, preventing the subsequent reduction reaction (2.0 and 1.3 V_{Li}). On the other hand, the reduction peak at 0.3 V_{Li} was not completely suppressed after 1st cycle, suggesting a different origin of the reaction, which proceeds even after the formation of the SEI-like film.

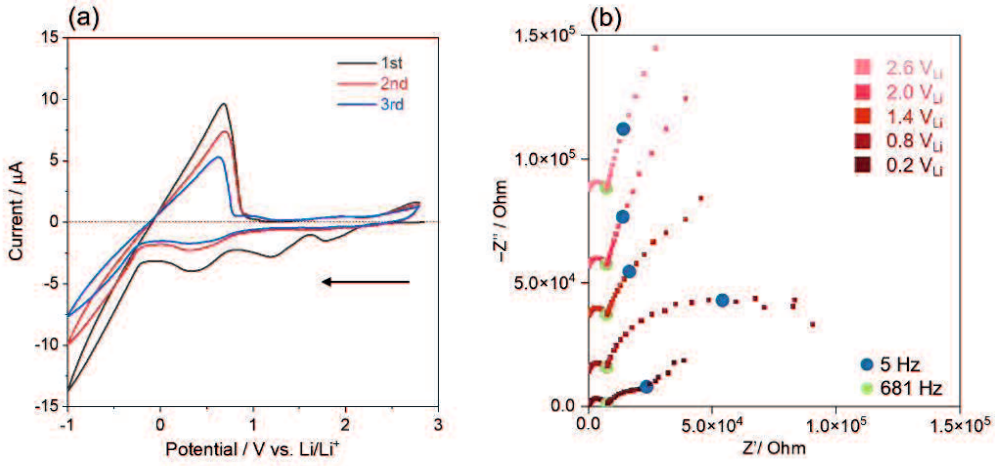

Figure 2.1 (a) Cyclic voltammetry of Cu electrode in PEO_{10}LiTFSA using 2032-type coin cell at a scanning rate of 1 mV/s. Distinct reduction peaks were observed at 2.0 V_{Li}, 1.3 V_{Li}, and 0.4 V_{Li} in the 1st cycle, which is derived from the decomposition of PEO_{10}LiTFSA electrolyte. (b) Nyquist plot of Cu/PEO_{10}LiTFSA/Li cell (area of each electrode: 0.21 cm^2) recorded from OCV (~2.6 V_{Li}) to 0.2 V_{Li} during an initial cathodic sweep of the LSV. The LSV curve obtained for the electrochemical impedance spectroscopy is shown in Figure 2.2, observing the comparable reduction peak. All the measurements were conducted at room temperature. Li foil was used as a reference and counter electrode.

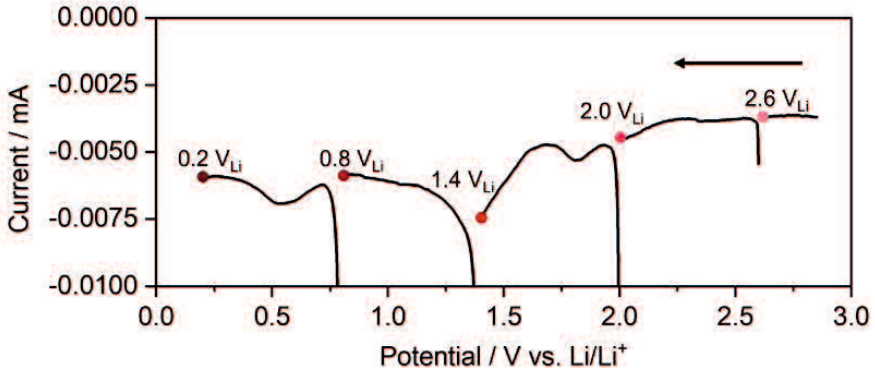

Figure 2.2 LSV curve for PEO_{10}LiTFSA on Cu electrode at room temperature for EIS measurement. EIS measurements were performed at 2.6 V_{Li}, 2.0 V_{Li}, 1.4 V_{Li}, 0.8 V_{Li}, and 0.2 V_{Li}.

The formation of the SEI-like film on the Cu surface was confirmed by electrochemical impedance spectroscopy (**Figure 2.1b**). The Nyquist plots at an open circuit voltage (OCV ~2.6 V_{Li}) consist of a semicircle at high frequencies (>1 kHz) and a slanted line at low frequencies, which corresponds to the lithium-ion migration in the electrolyte and the transfer reactions and diffusion of the lithium-ion occurs within the electrode, respectively. The diameter of a semicircle at a high-frequency region was almost the same throughout the potential range tested, further validating the assignment. A slanted line at the low-frequency region of OCV (~2.6 V_{Li}) and 2.0 V_{Li} looks almost the same, suggesting no change in the interfacial resistance. The shape of the low-frequency region slightly changed at 1.4 V_{Li}, where the first reduction process was completed. At 0.8 V_{Li}, a new semicircle was observed at the low-frequency region, which can be attributed to the charge transfer and surface layer resistance (R_{int}).[4] The increase of R_{int} observed at 0.8 V_{Li} can be correlated with the reduction products from the first (2.1-1.9 V_{Li}) and second (1.9-0.8 V_{Li}) reduction reactions, which likely formed a resistive layer on the Cu surface, passivating the surface and impeding charge transfer. The diameter of the low-frequency semicircle at 0.2 V_{Li} was smaller than that at 0.8 V_{Li}, suggesting the decrease in the R_{int} after the third reduction reaction at 0.8-0 V_{Li}. We hypothesize that the decreased R_{int} is attributed to the change in the SEI-like layer component and/or partial dissolution of the SEI-like layer into the electrolyte.

Cyclic voltammetry and impedance spectroscopy revealed that the three reduction peaks observed during the initial cathodic scan sequentially formed a resistive SEI-like layer on the Cu surface, affecting the charge transfer and surface layer resistance. Furthermore, we found that the surface resistance reached its maximum value at 0.8 V_{Li} and decreased at a further reductive condition, such as 0.2 V_{Li}, indicating the characteristics of the SEI-like layer depend on the potential. To understand the detail of the reduction mechanism of PEO_{10}LiTFSA electrolyte and the potential-dependent SEI component, we performed the *operando* attenuated total reflection infrared (ATR-IR) spectroscopy and *ex situ* XPS measurement.

Surface analysis on Cu electrode

Operando ATR-IR spectroscopy coupled with ex-situ XPS measurement successfully revealed the surface (electro)chemistry on the Cu surface during the lithium secondary battery operation, where LiTFSA reduced at ca. 2.0 V_{Li} to form LiF on the surface, followed by the PEO reduction reaction below 1.9 V_{Li} (**Figures 2.3**).

The CF_3 bending region (1160 cm^{-1} to 1240 cm^{-1}) of the *operando* ATR-IR spectra shows distinct peaks at 1199 cm^{-1} throughout the potential range tested (**Figure 2.3a**). We assigned the peak to the CF_3 bending of the TFSA anion[5], supported by the observation of a similar feature at 1188 cm^{-1} for bulk PEO_{10}LiTFSA electrolyte (Green). Note that the CF_3 bending peak of operando ATR-IR spectra was slightly (~11 cm^{-1}) shifted to the lower wavenumber than that of bulk spectra. The observed peak shift might suggest the weak interaction between the Cu surface and TFSA anion. To further understand the TFSA-related components in the SEI-like layer, we performed ex-situ XPS for the Cu surface after maintaining the potential at OCV, 1.9 V, 1.0 V, and 0 V (vs. Li/Li^+) for 12 h (**Figure 2.3b**).

The CF_3 bending region (1160 cm^{-1} to 1240 cm^{-1}) of the *operando* ATR-IR spectra shows distinct peaks at 1199 cm^{-1} throughout the potential range tested (**Figure 2.3a**). We assigned the peak to the CF_3 bending of the TFSA anion[5], supported by the observation of a similar feature at 1188 cm^{-1} for bulk PEO_{10}LiTFSA electrolyte (Green). Note that the CF_3 bending

peak of operando ATR-IR spectra was slightly (~11 cm^{-1}) shifted to the lower wavenumber than that of bulk spectra. The observed peak shift might suggest the weak interaction between the Cu surface and TFSA anion. To further understand the TFSA-related components in the SEI-like layer, we performed ex-situ XPS for the Cu surface after maintaining the potential at OCV, 1.9 V, 1.0 V, and 0 V (vs. Li/Li^+) for 12 h (**Figure 2.3b**).

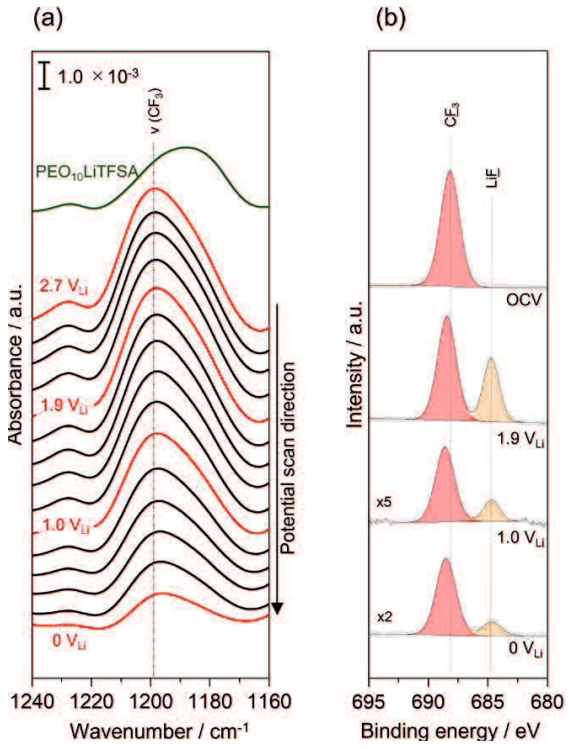

Figure 2.3 (a) CF_3 bending region of the *operando* ATR-IR spectra for Cu electrode surface in $PEO_{10}LiTFSA$ electrolyte at a potential range from 2.7 V_{Li} to 0 V_{Li}. ATR spectra (green) for $PEO_{10}LiTFSA$ electrolytes were shown for comparison. LSV curve obtained using the *operando* cell (shown in Figure 2.4) shows almost the same irreversible reduction peaks at 2.0 V_{Li}, 1.3 V_{Li}, and 0.4 V_{Li}, observed in Figure 2.1a, confirming that the reaction that occurred in these cells are comparable. (b) XPS spectra of the F1s photoemission lines of Cu electrode maintained at OCV, 1.9 V, 1.0 V, and 0 V (vs. Li/Li^+) for 12 h in $PEO_{10}LiTFSA$.

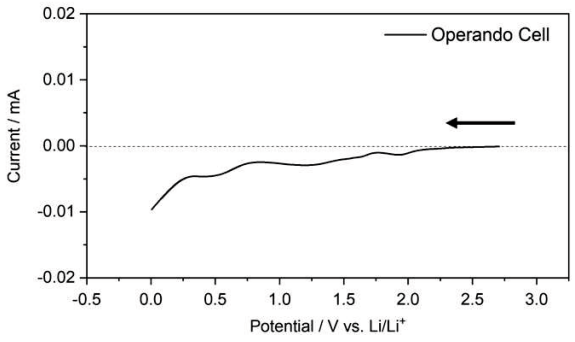

Figure 2.4 Liner sweep voltammetry of Cu electrodes in $PEO_{10}LiTFSA$ using *operando* ATR-IR cell at room temperature.

A sharp peak was observed at 688.4 eV at OCV, originating from the fluorine of the CF_3 of LiTFSA.[6, 7] In addition to CF_3, a new peak was observed at 684.8 eV in the spectra obtained at 1.9 V_{Li}, 1.0 V_{Li}, and 0 V_{Li}, which can be assigned to LiF formed via the reduction reaction of LiTFSA[8, 9] The observation suggests that the cathodic peak at around 2.0 V_{Li} (**Figure 2.1a**) corresponds to the reduction of LiTFSA, forming LiF on the Cu electrode. Our hypothesis was supported by the following arguments: Negligible change was observed in C1s and O1s regions at 1.9 V_{Li} compared to the OCV (**Figure 2.6b**), suggesting negligible decomposition of the PEO component was involved at 1.9 V_{Li}. To further validate our assignment, we conducted CV measurement in $PEO_{10}LiClO_4$ electrolyte on Cu electrode instead of $PEO_{10}LiTFSA$ (**Figure 2.5**). Although we found the same reduction peaks at 1.2 V_{Li} and 0.4 V_{Li} as for $PEO_{10}LiTFSA$, the distinctive reduction peak at around 2.0 V_{Li} disappeared for $PEO_{10}LiClO_4$. The result confirms that LiTFSA started to reduce at 2.0 V_{Li} to form LiF on the Cu electrode.

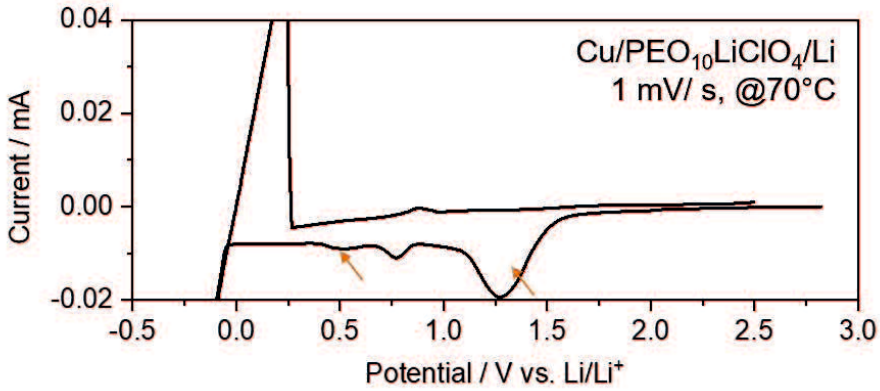

Figure 2.5 CV curve for $PEO_{10}LiClO_4$ on Cu electrode measured at 70°C. The peaks at around 1.3 V_{Li} and 0.5 V_{Li}, which is consistent with the reduction peaks observed for PEO-LiTFSA (1.3 V_{Li} and 0.3 V_{Li}). The peak at around 0.8 V_{Li}, which was not confirmed for the PEO-LiTFSA, is thought to be originated from the reaction of $LiClO_4$.

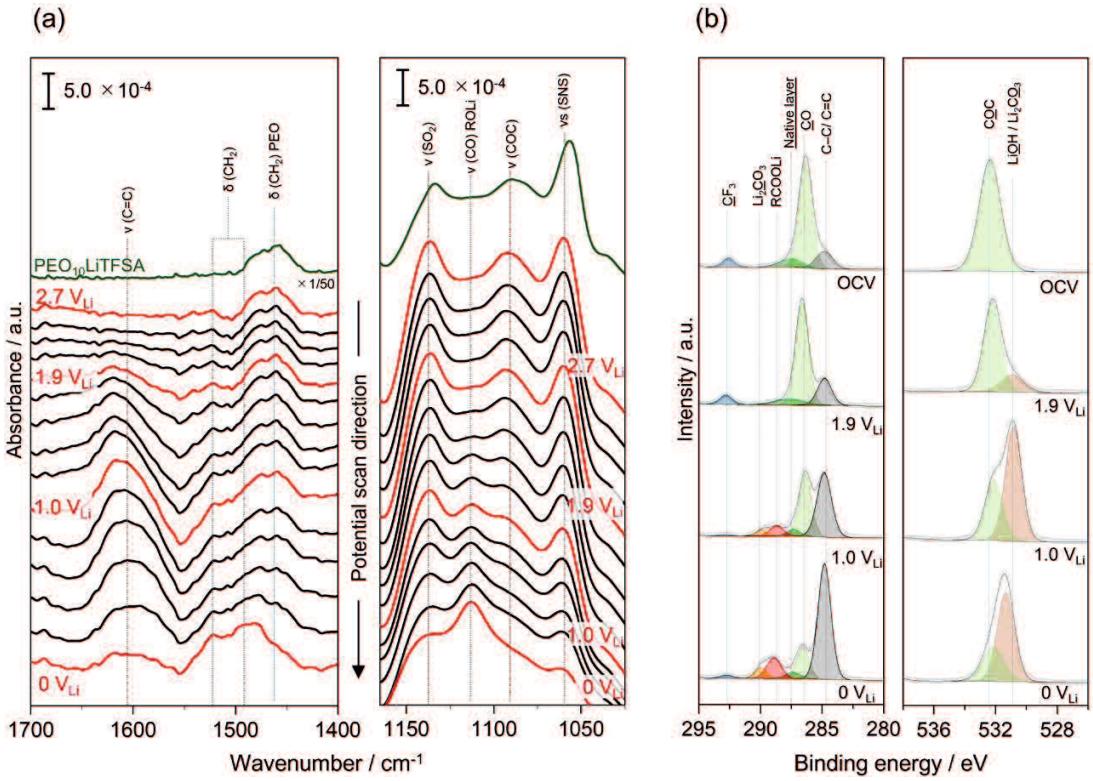

Figure 2.6 (a) CH_2 bending and CO stretching region of the *operando* ATR-IR spectra for Cu electrode surface in PEO_{10}LiTFSA electrolyte at a potential range from 2.7 V_{Li} to 0 V_{Li}. ATR spectra (green) for PEO_{10}LiTFSA electrolytes were shown for comparison. (b) XPS spectra of the C1s and O1s photoemission lines of the Cu electrode maintained at OCV, 1.9 V, 1.0 V, and 0 V (vs. Li/Li^+) for 12 h in PEO_{10}LiTFSA.

CH_2 bending and CO stretching region of the *operando* ATR-IR spectra and C1s and O1s region of the XPS spectra can capture characteristic peaks from PEO (**Figure 2.6**). The *operando* ATR-IR spectra collected at OCV (2.7 V_{Li}) show almost the same feature as the bulk PEO_{10}LiTFSA spectra (shown in green line), where we observe peaks at ca. 1092 cm^{-1} and ca. 1460 cm^{-1}, which can be assigned to C-O stretching and CH_2 bending mode, respectively.[10, 11, 12] The only difference between the OCV and bulk spectra is the shift in the TFSA-related peaks, e.g., 1060 cm^{-1} and 1137 cm^{-1}, attributed to SNS stretching and SO_2 symmetric stretching mode, respectively.[13, 14, 15] The observed slight peak shift for TFSA-

related peaks is consistent with the aforementioned interaction between the Cu surface and TFSA anion, suggested by the CF_3 bending mode (**Figure 2.3a**).

In the C1s region of the XPS spectra at OCV (2.7 V_{Li}), we observed one strong feature at around 285 eV and a small feature at 292.8 eV; the former feature can be interpreted as the adventitious electrolyte, including hydrocarbon (284.8 eV), C-O in PEO (286.4 eV).[9, 16] Although the peak at 287.5 eV is usually assigned to C=O[17, 18], we assigned the peak to the native layer on the Cu electrode since the same feature was also found in the bare Cu electrode (**Figure 2.7**). The latter feature can be assigned to the CF_3 in TFSA anion (292.6 eV), which agrees well with the observation in the F1s region in **Figure 2.3b**. The observation in O1s spectra at OCV (2.7 V_{Li}) was in line with that for C1s, where we observed a sharp peak at 532.4 eV assigned to C-O in PEO.[9, 19, 20] Therefore, we conclude that negligible chemical processes occurred at OCV, and PEO_{10}LiTFSA can stably exist on the Cu surface.

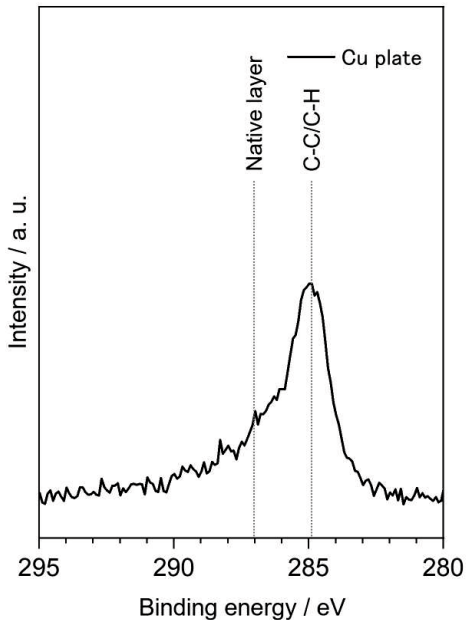

Figure 2.7 XPS spectra of the C1s photoemission line of the bare Cu electrode surface.

Operando ATR-IR spectra collected from 2.7 V_{Li} to 1.9 V_{Li} showed negligible change in all wavenumber ranges, suggesting PEO is electrochemically stable in this potential region. We observed several new peaks at 531.1 eV in the O1s region of the XPS spectra at 1.9 V_{Li}, which corresponds to the Li_2CO_3/LiOH , respectively. [21,22,23,24] The observation of Li_2CO_3 is in good agreement with the C1s spectra, strengthening our proposed assignment. Although LiOH is considered not a major product in the SEI formed in a carbonate-based electrolyte, a small amount of LiOH was formed in the PEO_{10}LiTFSA electrolyte. The observation may be due to the relatively high concentration of H_2O contamination in the polymer electrolytes compared to liquid electrolytes, promoting LiOH formation via the reduction of H_2O.[9] The slight difference in the observed component in *operando* ATR-IR and ex situ XPS can be due to the different electrochemical procedures (LSV for operando ATR-IR and chronoamperometry for 12 h for ex situ XPS) to obtain the sample, which may affect the amount of surface species formed on the electrode (more surface species accumulated on ex situ XPS sample).

In the potential region from 1.9 V_{Li} to 1.0 V_{Li}, growth of peaks at around 1113 cm^{-1} and 1610 cm^{-1} was observed in *operando* ATR-IR spectra, which were assigned to C-O stretching mode of Li alkoxide and C=C stretching mode of PEO-decomposed species, respectively. [25,26,27,28,29] The consistent observation was seen in ex situ XPS spectra, where a significant decrease in the CO-related peaks (286.4 eV and 532.4 eV) from PEO structure together with the increase in the C=C/C-C (284.8 eV), Li_2CO_3/LiOH (289.9 eV and 531.2 eV), and RCOOLi (288.7 eV). The observation indicates that the decomposition of PEO at 1.9 V_{Li} - 1.0 V_{Li}, leads to forming Li alkoxide and PEO-decomposed species with C=C components.

In *operando* ATR-IR spectra, the intensity of the C=C stretching peak (1610 cm^{-1}) reached a maximum value at 0.6 V_{Li} and decreased with the potential decreasing below 0.6 V_{Li}. Meanwhile, a new peak at ca. 1520 cm^{-1}, assigned to CH_2 bending, started to grow from 0.6 V_{Li} in accordance with the decrease in the intensity of the C=C stretching peak at 1610 cm^{-1}. Therefore, we propose a further reduction of C=C containing surface species and/or breakage of C=C bond to form various alkyl species occurring in the potentials 1.0-0.7 V_{Li}.

At 0 V_{Li}, C=C stretching peak (1610 cm^{-1}) and CO stretching peak from PEO (1092 cm^{-1}) almost disappeared while the Li alkoxide peak (1113 cm^{-1}) and alkyl peaks (around 1520 cm^{-1}) became more dominant, suggesting the further reduction of PEO and C=C components to LiOR and saturated hydrocarbon species. The ex-situ XPS supports our hypothesis, where the CO-related peaks from PEO (286.4 eV and 532.4 eV) became significantly small, and the intensity of hydrocarbon peaks (284.8 eV) gradually increased at 0 V_{Li} compared to 1.0 V_{Li}, suggesting the decomposition of PEO structure as well as the increased amount of saturated hydrocarbon on Cu surface potential at 0 V_{Li}. Furthermore, the increase in the Li_2CO_3 peak intensity at 531.1 eV was observed at 0 V_{Li}, suggesting the formation of Li_2CO_3 at around 1.0-0 V_{Li}.

Reduction mechanism of PEO_{10}LiTFSA and the correlation between SEI components and its resistance

We here summarize a surface (electro)chemical process on the Cu electrode in PEO_{10}LiTFSA based on the *operando* ATR-IR and ex-situ XPS, as well as its effect on the characteristics of the SEI-like layer probed by the electrochemical impedance spectroscopy (**Figure 2.8**). The negligible chemical processes occurred at OCV (~2.7 V_{Li}), and PEO_{10}LiTFSA can stably exist on the Cu surface. At around 1.9 V_{Li}, LiTFSA is started to reduce and form the inorganic SEI-like layer with LiF component. The experimental observation also suggested the existence of residual H_2O and CO_2, which could also be reduced at around 1.9 V_{Li}, and was responsible for forming a trace amount of LiOH and Li_2CO_3, respectively.[30, 31, 32, 33] The inorganic SEI-like layer did not increase the interfacial resistance as seen in the Nyquist plots at 1.4 V_{Li}, suggesting that the SEI-like layer originated from the TFSA anion has a negligible effect on the surface charge transfer kinetics.

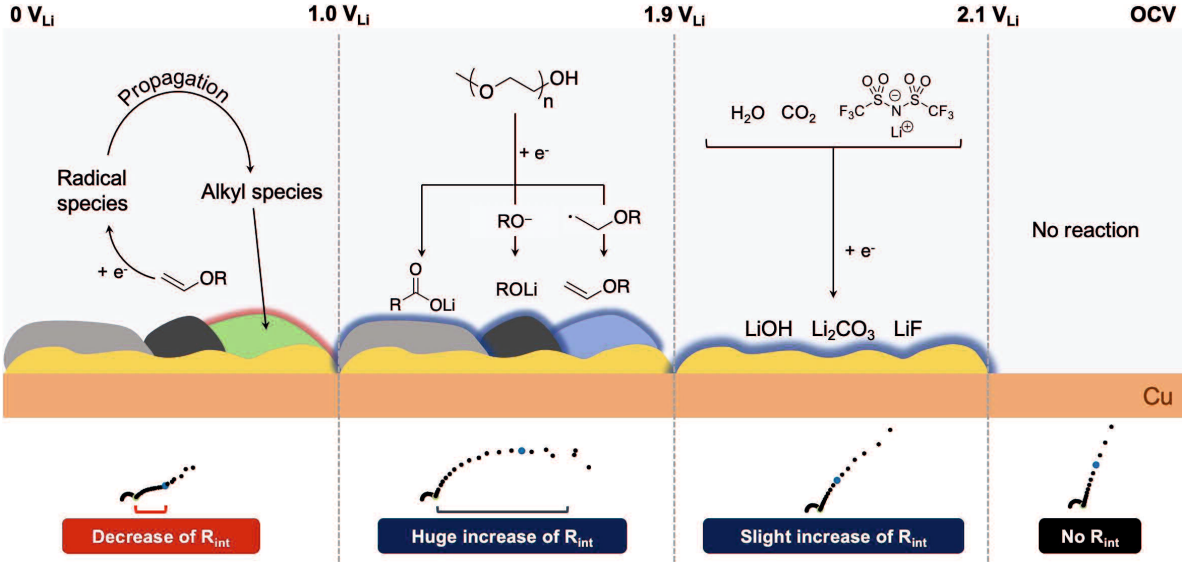

Figure 2.8 Proposed surface (electro)chemical process on the Cu electrode in PEO_{10}LiTFSA. Almost no (electro)chemical reaction occurred at OCV (~2.7 V_{Li})-2.1 V_{Li}; LiTFSA and residual H_2O and CO_2 reduced and formed an inorganic SEI-like layer at 2.1-1.9 V_{Li}; PEO matrix reduced and form lithium alkoxide (LiOR), PEO-decomposed species with C=C components (vinyl ether), and RCOOLi via radical formation at 1.9-1.0 V_{Li}; PEO-decomposed species with C=C components (vinyl ether) further reduced to short-chain polymer with low molecular weight at 1.0-0 V_{Li}.

After forming the TFSA-related SEI-like layer at 1.9 V_{Li}, the PEO matrix reduced in the potential range from 1.9 V_{Li} to 1.0 V_{Li} in the following mechanism. The C-O bond in PEO broke and became several components, including an alkoxide fragment (lithium alkoxide, LiOR) and an alkyl radical. It should be noted that the formation of radicals can hardly be observed in this work since radical species are highly-reactive intermediates with a significantly short lifetime than the experimental time resolution. The alkyl radical with an electron on the carbon atom undergoes subsequent reaction resulting in the formation of the PEO-decomposed species with C=C components (vinyl ether) and RCOOLi, which we confirmed in both *operando* ATR-IR and XPS. The R_{int} became significantly larger from 1.4 V_{Li} to 0.8 V_{Li}, which may attribute to the existence of non-polar vinyl ether in the SEI-like layer and/or the thickened SEI-like layer.

Operando ATR-IR measurement revealed that PEO-decomposed species with C=C components (vinyl ether) in the SEI were further reduced below 0.6 V_{Li}. Although the exact reaction is still unclear, we propose that the PEO-decomposed species with C=C components can be further reduced to radical fragment, and breaks the PEO chain into various alkyl species via propagation of radicals. The R_{int} at around 0.2 V_{Li} became considerably smaller than that of 0.8 V_{Li}. The significant decrease of R_{int} emphasizes the negative impact of having unsaturated hydrocarbons in the SEI as well as the formation of a short-chain polymer with low molecular weight via the reduction of C=C components.[34, 35]

2.4 Conclusions

The surface (electro)chemical process of the PEO_{10}LiTFSA electrolyte on the Cu electrode and its effects on the interfacial resistance were elucidated using *operando* ATR-IR and ex-situ XPS techniques. At the Cu electrode and PEO_{10}LiTFSA electrolyte interface, the SEI-like layer formation involves three reduction steps at around 2.1-1.9 V_{Li}, 1.9-0.8 V_{Li}, and 0.8-0 V_{Li}. LiTFSA is first reduced at ca. 2.0 V_{Li}, forming an inorganic SEI-like layer with LiF component. Furthermore, in the same potential range, residual H_2O and CO_2 were reduced to form a trace amount of LiOH and Li_2CO_3. Electrochemical impedance spectroscopy revealed that the inorganic SEI-like layer did not affect the interfacial resistance. In the potential below 1.9 V_{Li}, the C-O bond of PEO is broken, and forms decomposed products, such as lithium alkoxide, PEO-decomposed species with C=C components, and RCOOLi. The most resistive SEI-like layer was found at 0.8 V_{Li}, when the SEI consists of LiOH, Li_2CO_3, RCOOLi, ROLi, and PEO-decomposed species with C=C components, suggesting the large negative effect of having non-polar unsaturated hydrocarbons in the SEI-like layer and/or the thickened SEI-like layer on the interfacial resistance. At potentials below 0.8 V_{Li}, the PEO-decomposed species with C=C components were further reduced into various alkyl-related species. The observed change in the component of the SEI-like layer coincides with the significant reduction of the interfacial resistance value, suggesting that the component of the SEI-like layer dictates its resistance. This study not only sheds light on the surface

(electro)chemical process at the polymer electrolyte-Cu electrode interface but also emphasizes the importance of tuning the components of the SEI-like layer formed in a polymer electrolyte system.

References

1 L. F. Li, D. Totir, Y. Gofer, G. S. Chottiner and D. A. Scherson, *Electrochim. Acta*, 1998, **44**, 949–955.

2 M. Zhao, S. Kariuki, H. D. Dewald, F. R. Lemke, R. J. Staniewicz, E. J. Plichta and R. A. Marsh, *J. Electrochem. Soc.*, 2000, **147**, 2874.

3 Z.-C. Wang, J. Xu, W.-H. Yao, Y.-W. Yao, Y. Yang, *ECS Trans.* 2012, **41**, 29.

4 R. Tatara, P. Karayaylali, Y. Yu, Y. Zhang, L. Giordano, F. Maglia, R. Jung, J. P. Schmidt, I. Lund and Y. Shao-Horn, *J. Electrochem. Soc.*, 2019, **166**, A5090–A5098.

5 E. E. Ushakova, A. V. Sergeev, A. Morzhukhin, F. S. Napolskiy, O. Kristavchuk, A. V. Chertovich, L. V. Yashina and D. M. Itkis, *RSC Adv.*, 2020, **10**, 16118–16124.

6 H. Sonoki, M. Matsui and N. Imanishi, *J. Electrochem. Soc.*, 2019, **166**, A3593–A3598.

7 S. Jiao, X. Ren, R. Cao, M. H. Engelhard, Y. Liu, D. Hu, D. Mei, J. Zheng, W. Zhao, Q. Li, N. Liu, B. D. Adams, C. Ma, J. Liu, J.-G. Zhang, W. Xu, *Nat. Energy*, 2018, **3**, 739.

8 L. Suo, D. Oh, Y. Lin, Z. Zhuo, O. Borodin, T. Gao, F. Wang, A. Kushima, Z. Wang, H. C. Kim, Y. Qi, W. Yang, F. Pan, J. Li, K. Xu and C. Wang, *J. Electrochem. Soc.*, 2017, **14**, 5630–5637.

9 C. Xu, B. Sun, T. Gustafsson, K. Edström, D. Brandell and M. Hahlin, *J. Mater. Chem. A*, 2014, **2**, 7256–7264.

10 W. Wieczorek, D. Raducha, A. Zalewska and J. R. Stevens, *J. Phys. Chem. B*, 1998,

102, 8725–8731.

11 I. S. Elashmawi and L. H. Gaabour, *Results Phys.*, 2015, **5**, 105–110.

12 E. M. Abdelrazek, A. M. Abdelghany, S. I. Badr and M. A. Morsi, *Res. J. Pharm. Biol. Chem. Sci.*, 2016, **7**, 1877–1890.

13 S. Jeschke, M. Mutke, Z. Jiang, B. Alt and H. D. Wiemhöfer, *ChemPhysChem*, 2014, **15**, 1761–1771.

14 A. Narita, W. Shibayama and H. Ohno, *J. Mater. Chem.*, 2006, **16**, 1475–1482.

15 I. Rey, J. C. Lassègues, J. Grondin and L. Servant, *Electrochim. Acta*, 1998, **43**, 1505–1510.

16 V. Sharova, A. Moretti, T. Diemant, A. Varzi, R. J. Behm and S. Passerini, *J. Power Sources*, 2018, **375**, 43-52.

17 M. Nie, J. Demeaux, B. T. Young, D. R. Heskett, Y. Chen, A. Bose, J. C. Woicik and B. L. Lucht, *J. Electrochem. Soc.*, 2015, **162**, A7008–A7014.

18 L. El Ouatani, R. Dedryvère, C. Siret, P. Biensan, S. Reynaud, P. Iratçabal and D. Gonbeau, *J. Electrochem. Soc.*, 2009, **156**, A103.

19 B. Sun, C. Xu, J. Mindemark, T. Gustafsson, K. Edström and D. Brandell, *J. Mater. Chem. A*, 2015, **3**, 13994–14000.

20 A. M. Andersson and K. Edström, *J. Electrochem. Soc.*, 2001, **148**, A1100.

21 K. Kanamura, H. Tamura, S. Shiraishi and Z. ichiro Takehara, *J. Electroanal. Chem.*, 1995, **394**, 49–62.

22 K. I. Morigaki and A. Ohta, *J. Power Sources*, 1998, **76**, 159–166.

23 D. Bar-Tow, E. Peled and L. Burstein, *J. Electrochem. Soc.*, 1999, **146**, 824–832.

24 N. D. Phillip, C. Daniel and G. M. Veith, *J. Electrochem. Soc.*, 2020, **167**, 040521.

25 T. Ichino, B. D. Cahan and D. A. Scherson, *J. Electrochem. Soc.*, 1991, **138**, L59–L61.

26 D. Aurbach, M. Daroux, P. Faguy and E. Yeager, *J. Electroanal. Chem.*, 1991, **297**, 225–244.

27 J. Wang, Z. Li, S. Li, W. Qi, P. Liu, F. Liu, Y. Ye, L. Wu, L. Wang and W. Wu, *PLoS One*, 2013 , **8**, e72475.

28 L. Zhong and K. Yun, *Int. J. Nanomedicine*, 2015, **10**, 79–92.

29 D. Aurbach and E. Granot, *Electrochim. Acta*, 1997, **42**, 697–718.

30 K. U. Schwenke, S. Solchenbach, J. Demeaux, B. L. Lucht and H. A. Gasteiger, *J. Electrochem. Soc.*, 2019, **166**, A2035–A2047.

31 R. Bernhard, M. Metzger, H. A. Gasteiger, *J. Electrochem. Soc.* 2015, **162**, A1984.

32 G. V. Zhuang and P. N. Ross, *Electrochem. Solid-State Lett.*, 2003, **6**, 136–139.

33 S. J. An, J. Li, C. Daniel, D. Mohanty, S. Nagpure and D. L. Wood, *Carbon N. Y.*, 2016, **105**, 52–76.

34 K. Timachova, H. Watanabe and N. P. Balsara, *Macromolecules*, 2015, **48**, 7882–7888.

35 D. Devaux, R. Bouchet, D. Glé and R. Denoyel, *Solid State Ionics*, 2012, **227**, 119–127.

YAMAGUCHI
UNIVERSITY

Chapter 3

Sulfur-inserted polymer-anchored edge exfoliated graphite for durable positive electrodes for lithium–sulfur batteries

3.1 Introduction

Among researchers in recent years are attracted by Li-S battery , which have extremely high specific capacity and natural abundance. The main obstacle for commercialization of Li-S battery is capacity fading during early cycle, caused by the destruction of carbon material the volume expansion of sulfur during charge/ discharge. To address the obstacle, we propose a new carbon material anchored flexible polymer within the interlayer of carbon, aiming to accommodate the significant volume expansion of sulfur. The polymer-anchored edge-exfoliated graphite (PPG-EExG) was prepared by radical reaction and evaluated their electrochemical performance by comparing conventional carbon-sulfur cathodes, i.e., graphite (G-S) with layered structure, expanded graphite (ExG-S), ketjen black (KB-S) with hollow structure, and PEG-anchored edge-exfoliated graphite (PEG-EExG-S). To confirm the introduction of sulfur into carbon material, thermo gravimetry (TG), scanning electron microscopy (SEM) and X-ray diffraction (XRD) were performed. The galvanostatic charge–discharge measurement was used to compare the electrochemical performance of various carbon-sulfur cathodes. The Gas chromatography–mass spectrometry was performed to measure the cyclability of sulfur on the carbon-sulfur cathode after galvanostatic measurement. Finally, the mechanism of the capacity loss for each cathode was revealed and illustrated.

3.2 Experimental

Electrocatalyst preparation

Polymer-anchored Edge-exfoliated graphite (Polymer-EExG) was synthesized following the previously reported method.[1] Polypropylene glycol (PPG, Sanyo Chemical) and Polyethylene glycol (PEG, Sanyo Chemical) were selected as an anchoring polymer and decorated at the edge portion of the expanded graphite (PF8, Toyo Tanso) by radical trapping and subsequent heat treatment. The excess polymer was removed by treated the resultant composite at 500ºC for 120 min.

The mechanically mixed carbon-sulfur composite (denoted as G-S(mix), ExG-S(mix), and PPG-EExG(mix)) was obtained by mixing carbon (Graphite (G, Wako Pure Chemicals), exfoliated graphite (ExG, Toyo Carbon), and Polymer-EExG) with S_8 (Kishida) in a 1: 2 weight ratios using a mortar for 10 min.

The simple acid-base reaction between sodium thiosulfate (Wako Pure Chemical) and hydrochloric acid (Wako Pure Chemical) was employed to obtain carbon-sulfur composite.[2] The solution containing 0.1 g of carbon (G and ExG), 1.7 g of sodium thiosulfate, and 20 mL of deionized water was mixed with 1.2 mL of hydrochloric acid dropwise at 60ºC and stirred for 5 min. The resulting solid product is then filtered and rinsed with deionized water and dried in vacuum at 60°C for 12 h. The corresponding polymer-EExG-sulfur composite was synthesized in a similar manner, except for having a pre-dispersion process of ultrasonic dispersion in 10 mL of tetrahydrofuran (THF, Wako Pure Chemical) for 3 h. The dispersed liquid added to the solution consists of 1.6 g of sodium thiosulfate and 10 mL of deionized water. The acid-base reaction was carried out following the procedure described above.

Characterization methods

The microstructure of the electrocatalysts was analysed by a scanning electron microscope (SEM, JSM-7600F, JEOL Ltd.) equipped with an energy dispersive X-ray spectrometer (EDS, JMS-7600F, JEOL Ltd.). SEM was performed on an accelerating voltage of 5 kV. The X-ray diffraction (XRD) patterns of the electrocatalysts were obtained using an X-ray diffractometer (Rigaku Ultima IV) with Cu Kα radiation. Thermogravimetric analysis (TGA) was performed using a Thermo Plus EVO II (Rigaku) from room temperature to 500 ºC, at a heating rate of 20 ºC min^{-1} under helium atmosphere. Thermal decomposition temperature (T_d) was defined as the temperature at which 5% weight loss took place in TGA. The gas chromatography-mass spectroscopy (GC-MS) of the electrode before and after the galvanostatic measurement was performed on GCMS-QP2010Ultra (Shimadzu). After reaching the end-of-charge potential, the CR2032-type coin cell was immediately disassembled in Ar-filled glovebox and dried in the Ar atmosphere before the measurement.

Electrochemical methods

The electrochemical behaviour of the electrodes was confirmed by galvanostatic measurements and cyclic voltammetry (CV) in two-electrodes cells (CR2032-type coin cells). Cells were assembled in an Ar-filled glovebox and comprised of a Li metal foil (Honjo Metal) as the negative electrode, separated by glass filter separator (Advantec). The positive electrode was obtained by mixing carbon-sulfur composite and sodium alginate (Kishida) in a 10: 1 weight ratio with ultrapure water. The slurry was further stirred for 15 mins, followed by deforming for 3 mins by electric mixer (AR-100, Thinky). The resultant slurry was

deposited on the carbon paper (TGP-H-060, Toray) and dried at 60°C for 24 h. Subsequently, positive electrodes were cut into a round with a diameter of 10 mm. 100 μL of electrolyte (1 M lithium bis(trifluoromethanesulfonyl)imide (LiTFSA, Kishida) in a 1:1 volume ratio 1,2-dimethoxyethane (DME, Kishida) : 1,3-dioxolane (DOL, Kishida) with 0.1 M $LiNO_3$ (Wako pure Chemicals) additive) was impregnated to the glass filter separator.

Galvanostatic charge-discharge measurements were performed in the potential range of 1.7−3.3 V at 30°C using an automatic charge/discharge instrument (HJ1001SD8, Hokuto Denko). Cells were charged at a rate of 0.05 C (around 0.065 mA cm^{-2}) for all the electrodes, based on the theoretical capacity calculated based on the mass of sulfur obtained by TG measurement. Specific capacity was calculated based on the mass of sulfur (mAh g_{sulfur}^{-1}) unless otherwise noted. An SP-150 Potentiostat (Bio-Logic) was employed to conduct the cyclic voltammetry (CV) with the CR2032-type coin cell. Lithium metals were used as a counter electrode as well as a quasi-reference electrode. Potential is converted to Li/Li^+ scale (V_{Li}) unless otherwise noted.

3.3 Results and discussion

Effect of sulfur at the graphene interlayer on Li-S battery performances

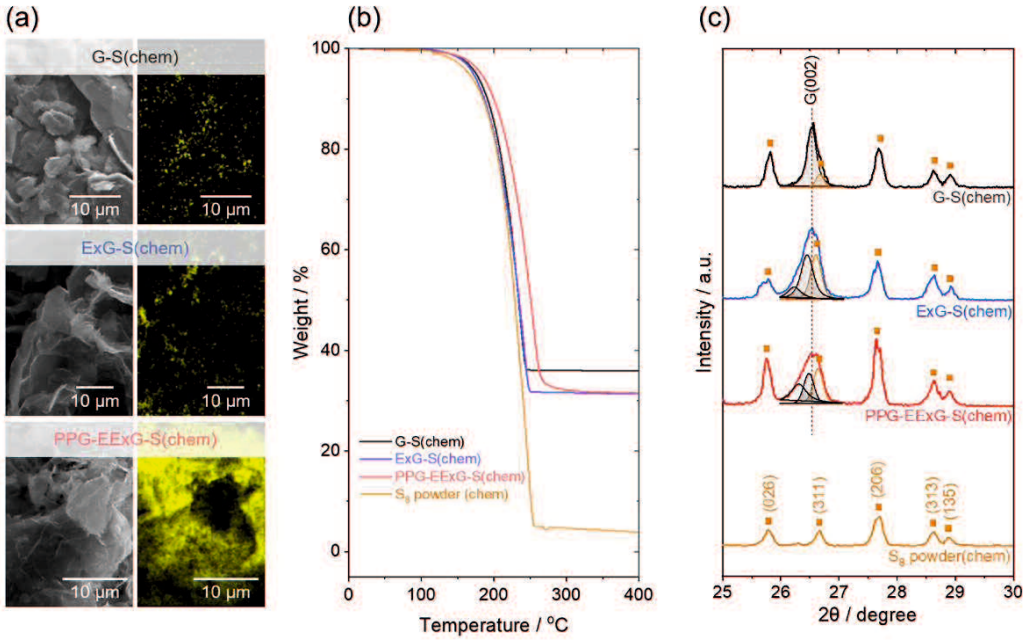

Figure 3.1 Characterization of the G-S(chem), ExG-S(chem), and PPG-EExG-S(chem) synthesized via chemical incorporation of sulfur. (a) SEM images (left) and corresponding EDS mapping (right) for G-S(chem), ExG-S(chem), and PPG-EExG-S(chem) electrodes. (b) Thermogravimetric curves for G-S(chem), ExG-S(chem), and PPG-EExG-S(chem) obtained under He atmosphere at a heating rate of 20°C min^{-1}. Thermogravimetric curve for chemically synthesized S_8 powder is also shown for comparison. (c) X-ray diffraction patterns of G-S(chem), ExG-S(chem), and PPG-EExG-S(chem). X-ray diffraction patterns of chemically synthesized S_8 powder is also shown for comparison.

Chemical incorporation of sulfur to the polymer-anchored Edge-exfoliated graphite (Polymer-EExG), based on a simple acid-base reaction, introduces sulfur uniformly into the interlayer space of graphene sheets without bulk sulfur formation (**Figure 3.1**).

Scanning electron microscopy (SEM) image (**Figure 3.1a**) and the corresponding elemental mapping of sulfur (**Figure 3.1a**) from energy dispersive spectrometer (EDS) analysis confirmed that the sulfur uniformly dispersed on the graphene surface with negligible bulk sulfur for all the electrodes tested in this study. The significantly improved dispersion of sulfur was observed for the PPG-EExG-S(chem), reflecting the excellent dispersibility of PPG-EExG in the THF-contained aqueous solution for the sulfur deposition reaction.

The amount of sulfur in G-S(chem), ExG-S(chem), and PPG-EExG-S(chem) electrodes were almost the same (~65 wt.%), according to the TG analysis (**Figure 3.1b**). All the electrode showed the weight loss at *ca.* 150°C, which corresponds to the evaporation of S_8[3]. The onset temperature of the weight loss for PPG-EExG-S(chem) was slightly higher (*ca.* 200°C) than bare S_8 particle (*ca.* 180°C) synthesized by the same method (noted as S_8(chem)), which indicates the stabilization of sulfur by the strong interaction with support materials[4]. The slight shift of the evaporation temperature for PPG-EExG-S(chem) thus suggests the introduction of S_8 into more confined spaces, *e.g.*, interlayer space of graphene sheets, where S_8 can strongly interact with graphene due to a short contact distance between the S atoms to the graphene sheet. Our hypothesis was supported by the XRD analysis (**Figure 3.1c**), where the diffraction peak corresponds to graphite (002) peak negatively shifted for PPG-EExG-S(chem) compared to G-S(chem) and ExG-S(chem). The decrease in the 2θ value corresponds to the expansion of the average graphene layer distance (calculated from 2θ of (002) peaks by Bragg's equation)[5], indicating the introduction of S_8 into the interlayer space of graphene sheets.

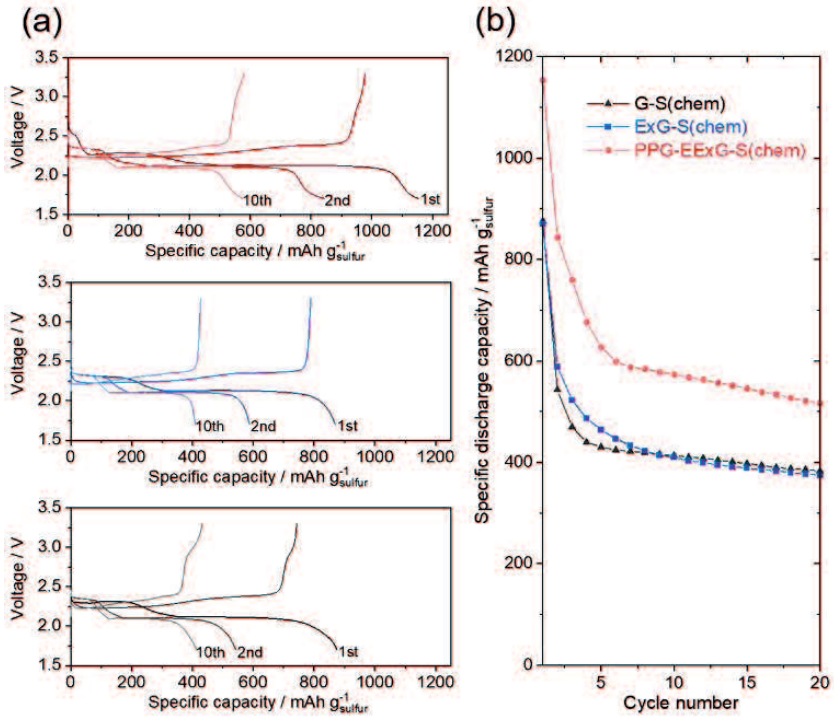

Figure 3.2 Electrochemical performance of G-S(chem), ExG-S(chem), and PPG-EExG-S(chem) synthesized via chemical incorporation of sulfur. (a) Galvanostatic charge-discharge curves at a rate of 0.05 C. Specific capacity was calculated according to the mass of S_8 obtained by TG analysis. (b) Cycle dependence of the specific discharge capacity for G-S(chem), ExG-S(chem), and PPG-EExG-S(chem) electrode calculated from galvanostatic charge-discharge measurement at a rate of 0.05 C.

We then evaluated the electrochemical Li storage capability of these carbon-sulfur composites as potential positive electrode materials for Li-S batteries. The PPG-EExG-S(chem) electrode exhibits higher initial capacity as well as cyclability compared with the G-S(chem) and ExG-S(chem), suggesting high sulfur efficiency and less dissolution of intermediates (*e.g.*, polysulfides) for PPG-EExG-S(chem) electrode (**Figure 3.2**). The notable improvement of overall electrochemical performance for the PPG-EExG-S(chem) electrode suggests the critical role of sulfur at the interlayer space of graphene sheets.

Discharge and charge voltage profiles for the carbon-sulfur composites (G-S(chem), ExG-S(chem), and PPG-EExG-S(chem)) containing ~65 wt.% sulfur confirms the same pattern of discharge and charge plateaus for all the carbon-sulfur composites at various cycles (**Figure 3.2a**). The discharge curves exhibited typical two-plateau behaviour of a sulfur positive electrode, corresponding to the formation of long-chain polysulfides (Li_2S_x, $x > 4$) at 2.3 V and short-chain polysulfides (Li_2S_2 and Li_2S) at 2.1 V[6]. Flat plateau for the latter process suggests a uniform deposition of Li_2S with small kinetic barriers. The initial specific capacity (calculated according to the mass of sulfur) was in the order of PPG-EExG-S(chem) (1154 mAh g_{sulfur}^{-1}) > G-S(chem) (876 mAh g_{sulfur}^{-1}) = ExG-S(chem) (870 mAh g_{sulfur}^{-1}), suggesting improved sulfur efficiency for PPG-EExG-S(chem). Furthermore, superior cyclability was confirmed for PPG-EExG-S(chem) electrode compared to the G-S(chem) and ExG-S(chem) electrodes (**Figure 3.2b**). PPG-EExG-S(chem) electrode delivers a reversible capacity of 517 mA h g_{sulfur}^{-1} after 20 cycles with the capacity retention of 45%. The G-S(chem) and ExG-S(chem) electrodes, on the contrary, exhibits a reversible capacity of only 382 mA h g_{sulfur}^{-1} and 374 mA h g_{sulfur}^{-1}, respectively, after 20 cycles. Based on the above experimental findings, we hypothesize that the introduction of sulfur into the interlayer space of graphene sheets plays a pivotal role in the improved initial capacity and cyclability of the PPG-EExG-S(chem) electrode.

Our hypothesis was supported by the evaluation of Li-S battery performance for the corresponding carbon-sulfur composites synthesized via mechanical mixing, where no improvement on Li-S battery performance was observed for PPG-EExG-derived electrodes without sulfur at the interlayer space of graphene sheets (**Figure 3.3**).

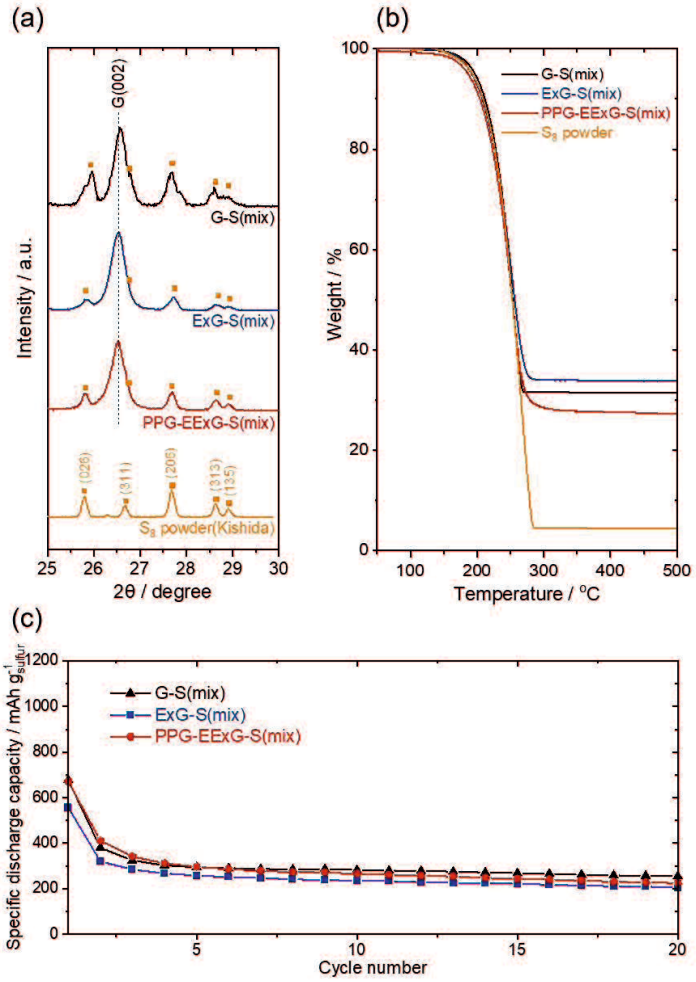

Figure 3.3 Characterization and electrochemical performance of the G-S(mix), ExG-S(mix), and PPG-EExG-S(mix) electrodes synthesized via mechanical mixing. (a) X-ray diffraction patterns of G-S(mix), ExG-S(mix), and PPG-EExG-S(mix). X-ray diffraction patterns of commercially available S_8 powder is also shown for comparison. (b) Thermogravimetric curves for G-S(mix), ExG-S(mix), and PPG-EExG-S(mix) obtained under He atmosphere at a heating rate of 20°C min^{-1}. Thermogravimetric curve for commercially available S_8 powder is also shown for comparison. (c) Cycle dependence of the specific discharge capacity for G-S(mix), ExG-S(mix), and PPG-EExG-S(mix) electrode calculated from galvanostatic charge-discharge measurement at a rate of 0.05 C.

The XRD patterns of the mechanically mixed carbon-sulfur composites (denoted as G-S(mix), ExG-S(mix), and PPG-EExG-S(mix)) showed negligible change in graphite (002) peak at 26.4 degree, suggesting almost no sulfur was introduced into the interlayer space of graphene sheets via mechanical mixing, unlike the chemical incorporation of sulfur (**Figure 3.3a**). Thermogravimetric curves for all the mechanically mixed carbon-sulfur composites overlapped with the TG curve of sulfur powder, further confirms no introduction of sulfur into the interlayer space of graphene occurred via mechanical mixing (**Figure 3.3b**). The XRD and TG analysis thus confirm that all the mechanically mixed carbon-sulfur composites, including PPG-EExG-S(mix), have a negligible amount of sulfur at the interlayer space of graphene sheet. Initial specific capacity and cyclability for the G-S(mix), ExG-S(mix), and PPG-EExG-S(mix) electrodes were almost the same (**Figure 3.3c**), indicating the distinctive improvement in initial capacity and cyclability of the PPG-EExG-S(chem) electrode was mainly achieved by the sulfur at the interlayer space of graphene sheet.

Sulfur redox at the graphene interlayer

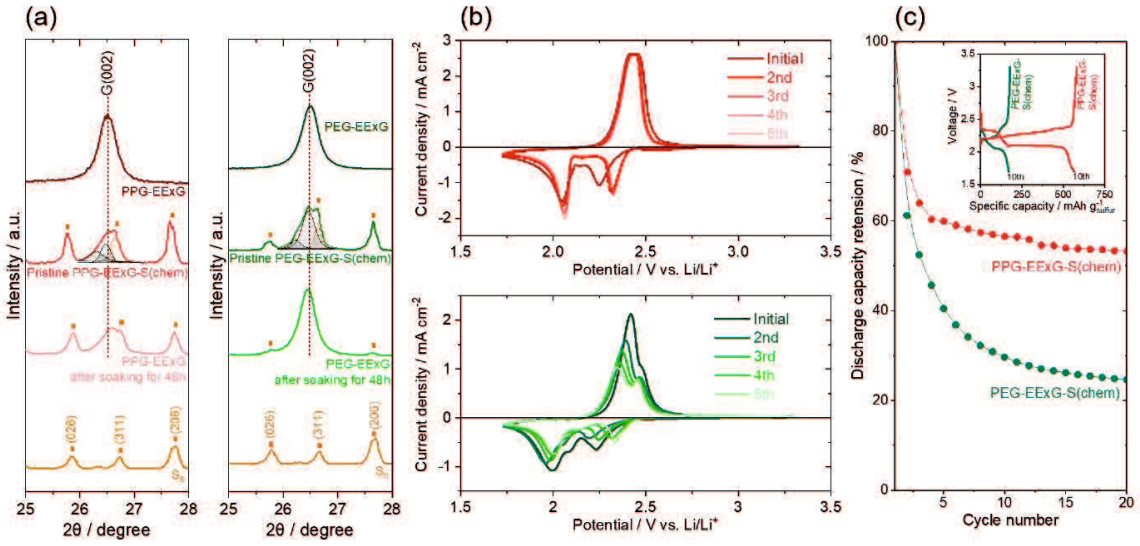

Figure 3.4 Comparison between PPG-EExG-S(chem) and PEG-EExG-S(chem) electrodes. (a) X-ray diffraction patterns of PPG-EExG-S(chem) (left) and PEG-EExG-S(chem) (right). X-ray diffraction patterns of chemically synthesized S_8 powder is also shown for comparison. (b) Cyclic voltammograms of PPG-EExG-S(chem) (top) and PEG- EExG-S(chem) (bottom) at a scan rate of 0.1 mV s^{-1}. (c) Cycle dependence of the specific discharge capacity for PPG-EExG-S(chem) and PEG-EExG-S(chem) electrode calculated from galvanostatic charge-discharge measurement at a rate of 0.05 C. Inset shows the corresponding charge-discharge curve at 20th cycle.

In order to understand the details of the sulfur redox reaction at the confined space between the graphene sheet, we compared the electrochemical behaviour of PPG-EExG-S(chem) and PEG-EExG-S(chem), having different polymer to anchor the graphene sheet (**Figure 3.4**). The result confirms that the sulfur at graphene interlayer indeed contributes to the high initial capacity, and preserving the layered structure is the key to the improved cyclability.

We selected two different polymer anchors, PPG and polyethylene glycol (PEG), having slightly different chemical structure to highlight the importance of the polymer anchor and polymer-anchored graphene interlayer on the electrochemical performance. X-ray diffraction pattern confirms the introduction of sulfur into the graphene interlayer for both PPG-EExG-S(chem) and PEG-EExG-S(chem) electrode, suggesting the comparable initial state of the sulfur for those electrodes (**Figure 3.4a**). The shape of graphene (002) peak of PEG-EExG-S(chem) electrode changed significantly after soaked in LiTFSA-DME/DOL electrolyte for 48 h, suggesting the breakage of stacked graphene structure due to the dissolution of PEG-anchor (**Figure 3.4a**). Therefore, PEG-EExG-S(chem) can highlight the effect of the sulfur at the interlayer space on its redox behaviour, since it has the sulfur at the graphene interlayer in the beginning but cannot maintain the stacked graphene structure in the electrochemical condition for a certain time (< 48 h). Initial cycle of the cyclic voltammogram was similar for those two electrodes (**Figure 3.4b**); first reduction peak was observed at *ca.* 2.3 V_{Li} followed by the second reduction peak at *ca.* 2.1 V_{Li}, which correlates with the formation of long-chain polysulfides and short-chain polysulfides, respectively. The large oxidation peak corresponds to S_8 formation was observed at *ca.* 2.4 V_{Li}, which gave oxidation current density of 2.5 mA cm^{-2} for PPG-EExG-S(chem) and 2.3 mA cm^{-2} for PEG-EExG-S(chem). The equivalent sulfur redox behaviour for PPG-EExG-S(chem) and PEG-EExG-S(chem) electrode in the initial cycle confirms the participation of sulfur at the graphene interlayer in the electrochemical processes, at least in the very beginning.

On the other hand, the cycle dependence of the cyclic voltammogram separates the two electrodes, and only PEG-EExG-S(chem) electrode showed a significant decrease in sulfur redox current by potential cycling (**Figure 3.4b**). Discharge capacity retention, calculated

from charge-discharge measurement, was consistent with the cyclic voltammetry, which confirmed the inferior cyclability for PEG-EExG-S(chem) electrode (**Figure 3.4c**). The poor cyclability of the PEG-EExG-S(chem) electrode highlights the crucial role of the graphene interlayer to maintain high capacity. We propose that the strong interfacial attraction between sulfur and graphene at the interlayer, suggested by TG (**Figure 3.1b**), improves the sulfur efficiency and the trapping of sulfur in the confined space inhibits the dissolution and/or diffusion of the polysulfide into the electrolyte. The dissolution of the PEG anchor during the electrochemical measurement gradually ruins the graphene interlayer structure; thus, the large capacity retention was observed for PEG-EExG-S(chem) compared to PPG-EExG-S(chem), while showing the similar sulfur redox behaviour in the beginning.

The preferable nature of the polymer-anchored graphene interlayer as a reaction field of a sulfur redox reaction is further clarified by comparing electrochemical performance with conventional carbon-sulfur composite electrode using porous/conductive carbon black (denoted as KB-S(chem)) (**Figure 3.5**). We here propose that the reaction kinetics, as well as the reversibility of the sulfur redox reaction, is enhanced at the polymer-anchored graphene interlayer, due to a short and rapid transport pathway for both electrons and Li ions derived from the unique layered structure and its superior electrical conductivity.

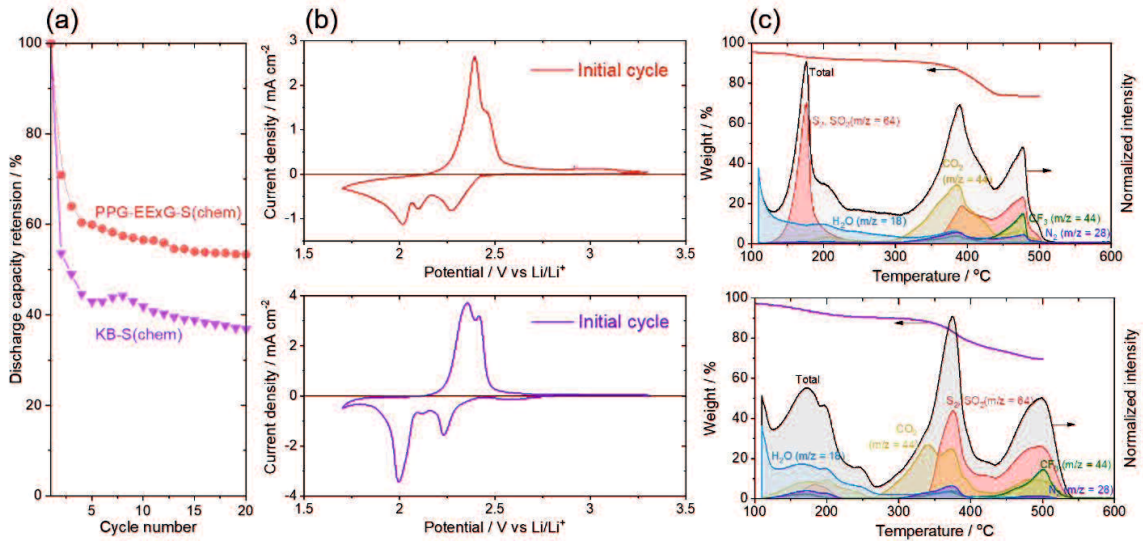

Figure 3.5 Comparison between PPG-EExG-S(chem) and KB-S(chem) electrodes. (a) Cycle dependence of the discharge capacity retention for PPG-EExG-S(chem) and KB-S(chem) electrode calculated from galvanostatic charge-discharge measurement at a rate of 0.05 C. (b) Cyclic voltammograms of PPG-EExG-S(chem) (top) and KB-S(chem) (bottom) at the initial cycle obtained at a scan rate of 0.1 mV s^{-1}. (c) Gas chromatography-mass spectroscopy (GC-MS) curves for M/S = 64 of PPG-EExG-S(chem) (top) and KB-S(chem) (bottom) after 5th charge of galvanostatic charge-discharge measurement. The corresponding thermogravimetric curve is also shown.

The initial discharge capacity of both PPG-EExG-S(chem) and KB-S(chem) showed the similar value (1153 mAh g_{sulfur}^{-1} for PPG-EExG-S(chem) and 1272 mAh g_{sulfur}^{-1} for KB-S(chem)) (**Figure 3.5a**), suggested the high sulfur efficiency accomplished for both electrodes by impregnating sulfur into graphene interlayer and mesopore (2 nm < D < 50 nm)[7,8], respectively, which gave the intimate contact between sulfur and the conductive carbon substrate. However, the significant capacity retention was observed for KB-S(chem) with 37 % compared to 45 % for PPG-EExG-S(chem) at 20 cycles. One of the reasons for the rapid decrease in KB-S(chem) capacity is the destruction of the mesopores for absorbing

the sulfur, which is essential for limiting polysulfide dissolution, due to the significant volume change of sulfur during the redox processes[9]. The PPG-EExG-S(chem), on the other hand, maintains its unique graphene interlayer structure owing to the flexible nature of polymer anchor, which can accommodate the volume expansion of sulfur.

Further detailed analysis of cyclic voltammogram revealed that the reaction reversibility, mainly Li_2S_x ($x > 4$) ↔ S_8 redox, was improved for PPG-EExG-S(chem) electrode (**Figure 3.5b**). The onset potentials of the first S_8 reduction (S_8 →Li_2S_x ($x > 4$)) shifted to more positive potential (2.4 V_{Li}) for PPG-EExG-S(chem) than KB-S(chem) (2.3 V_{Li}), suggesting the promotion of the S_8 reduction reaction on PPG-EExG-S(chem). The enhancement of the initial S_8 reduction reaction probably relates to the higher electrical conductivity of the graphene layer (241 S cm^{-1} for PPG-EExG, **Table 3.1**) than the carbon particles (15.2 S cm^{-1} for KB, **Table 3.1**). No potential shift was observed for the subsequent reduction reaction at *ca.* 2.0 V_{Li}, further highlights the contribution of high electrical conductivity on the electrochemical reduction of insulating S_8 particles.

Table 3.1 Electrical conductivity of KB, G, ExG, and PPG-EExG.

	Electrical conductivity / S cm^{-1}
KB	15.16
G	466.4
ExG	1777
PPG-EExG	240.7

The surface product analysis of the PPG-EExG-S(chem) and KB-S(chem) electrodes after a 5th charge, as deduced from GC-MS experiments, further supports the improved reaction reversibility for PPG-EExG-S(chem) electrode (**Figure 3.5c**). The GC-MS curve of M/S = 64 (corresponds to S_2 and SO_2) clearly showed distinctive features at *ca.* 180 ºC, *ca.* 390 ºC, and > 450 ºC, which can be assigned to S_8, short-chain polysulfides, and TFSI anion, respectively (**Figure 3.6**). The intensity ratio of S_8 peak and the peak for short-chain polysulfides was notably larger for PPG-EExG-S(chem) than KB-S(chem), which strongly indicates that more S_8 was formed on the PPG-EExG-S(chem) electrode after a 5th charge. The *ex-situ* reaction product analysis confirms that the PPG-EExG-S(chem) surface is capable of completely oxidize sulfur polysulfides to the last oxidation product (namely S_8) efficiently, even after 5th charge, which can contribute to the improved cyclability of PPG-EExG-S(chem) electrode.

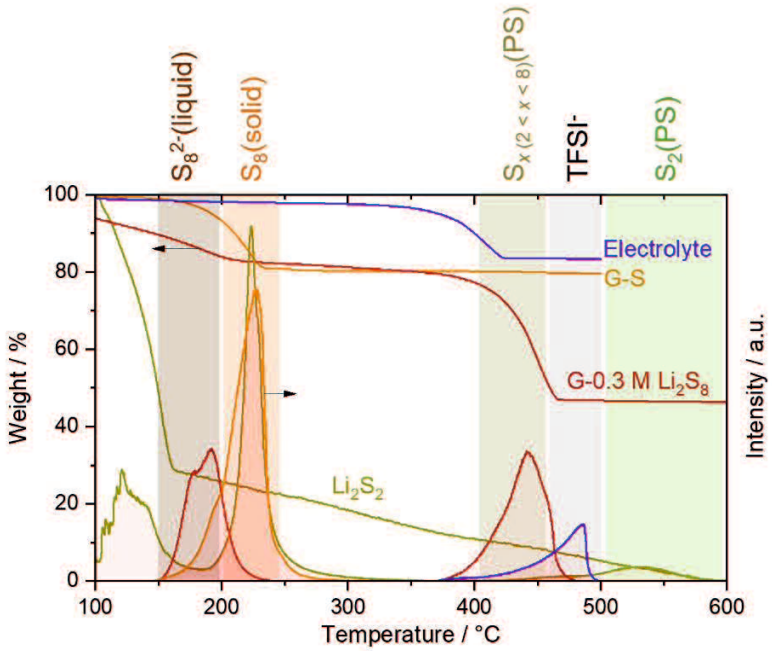

Figure 3.6 Gas chromatography-mass spectroscopy (GC-MS) curves for M/S = 64 of pure electrolyte (1 M LiTFSA in DME/DOL solution with 0.1 M $LiNO_3$ additive), G-S, G-0.3 M Li_2S_8 (0.3 M Li_2S_8 solution impregnated graphite electrode), and Li_2S_2. The corresponding thermogravimetric curve is also shown.

Mechanistic discussion

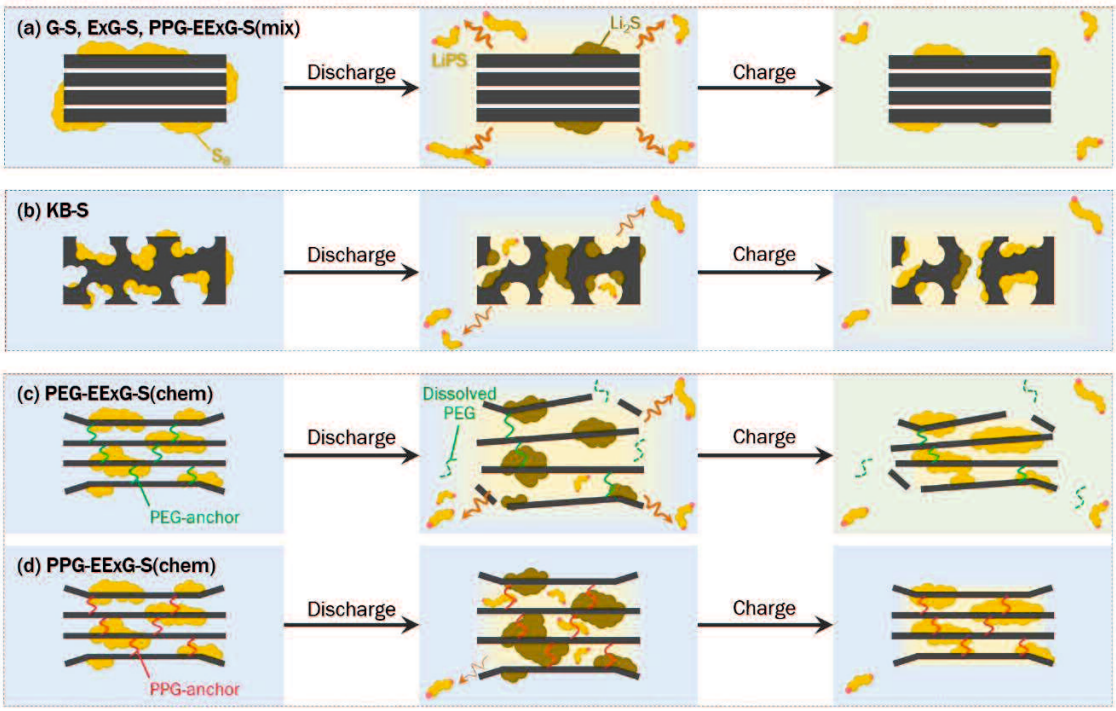

Scheme 3.1 Comparison of the proposed mechanisms during Li-S battery operation. (a) Proposed mechanisms for G-S, ExG-S, and PPG-EExG-S(mix) electrodes, showing the dissolution and/or diffusion of the lithium polysulfide to the electrolyte. (b) Proposed mechanisms for KB-S(chem) electrode, illustrating the gradual change in the electrode morphology due to the volume expansion of sulfur during charge-discharge. Proposed mechanisms for (c) PEG-EExG-S(chem) and (d) PPG-EExG-S(chem) electrode, where chemically stable and flexible PPG-anchor help maintaining the unique layered structure throughout the Li-S battery operation, resulting the improved initial capacity and cyclability for electrode.

We propose that the introduction of sulfur into the interlayer space of graphene sheets plays a pivotal role in the improved initial capacity and cyclability of the PPG-EExG-S(chem) electrode (**Scheme 3.1**).

For G-S, ExG-S, and PPG-EExG-S(mix) electrodes, elemental sulfur is mainly deposited on the surface, not in the graphene interlayer, which cannot promise rapid charge transfer and prevent sulfur being dissolved into the electrolyte (**Scheme 3.1a**). Although KB-S(chem) efficiently utilizes the sulfur in the initial discharge owing to its porous structure[10], the electrode morphology gradually ruins by the significant volume change of sulfur active materials, leading to a considerable decrease in capacity after several cycles (**Scheme 3.1b**).

The unique structure of PPG-EExG-S(chem) with superior electrical conductivity of graphene sheets provides a short and rapid transport pathway for both electrons and Li ions to achieve improved reaction kinetics (**Scheme 3.1d**). The large surface area (**Table 3.2**), provided by the efficient use of the graphene interlayer, contributes to the intimate contact between sulfur and graphene. Furthermore, sulfur at the interlayer space may possess a strong interfacial attraction between sulfur and graphene due to a short contact distance from the S atoms to the graphene sheet. The strong sulfur-support interaction promises rapid charge transfer and prevents sulfur from being dissolved into the electrolyte. Besides, the polymer anchor, which holds the graphene sheet, provides structural flexibility to accommodate the significant volume changes for sulfur during the redox processes and helps to preserve the morphology of the electrodes. PEG-EExG-S(chem), with chemically unstable PEG-anchor, showed high initial capacity but failed to show the excellent cyclability, mainly due to the destruction of the unique layered structure upon further charge-discharge cycle (**Scheme 3.1c**).

Table 3.2 Brunauer-Emmett-Teller (BET) surface area of KB, G, ExG, and PPG-EExG.

	BET surface area / $m^2 g^{-1}$
KB	1226
G	7.256
ExG	27.34
PPG-EExG	151.5

3.4 Conclusions

In summary, a sulfur-inserted polymer-anchored edge exfoliated graphite material (PPG-EExG-S(chem)) was introduced as a positive electrode for lithium-sulfur battery with high discharge capacity as well as improved cyclability. The chemical incorporation based on a simple acid-base reaction enables the insertion of elemental sulfur in the graphene interlayer, anchored by PPG polymer. The strong interfacial attraction between sulfur and highly conductive graphene sheet at the confined interlayer space enables rapid charge transfer and limits the dissolution of sulfur into the electrolyte, which improves the redox reaction reversibility and sulfur efficiency. The structural flexibility derived from PPG-anchor is a key to maintain the initial capacity over the cycles, by accommodating the significant volume changes of sulfur during the redox processes without destroying the unique structure. The substantial improvement in lithium-sulfur battery performance by PPG-EExG-S(chem) is thus achieved by the characteristic consistency of sulfur trapping within the confined and rigid structure while having certain structural flexibility to deal with the volume change during the reaction. This work proposes one of the promising design strategies of electrode materials for the next-generation lithium-sulfur batteries, which enables further improvement in the initial capacity as well as the cyclability.

References

1 Z. Li, H. Bin Wu and X. W. Lou, *Energy Environ. Sci.*, 2016, **9**, 3061–3070.

2 S. Nozato, A. Nakasuga, T. Wada, H. Yoshitani and H. Ihara, *RSC Adv.*, 2016, **6**, 25776–25779.

3 C. Liang, N. J. Dudney and J. Y. Howe, *Chem. Mater.*, 2009, **21**, 4724–4730.

4 D. LangeNA, *McGraw-Hill (edr), New York*.

5 J. S. Park, M. H. Lee, I. Y. Jeon, H. S. Park, J. B. Baek and H. K. Song, *ACS Nano*, 2012, **6**, 10770–10775.

6 J. Kim, D. J. Lee, H. G. Jung, Y. K. Sun, J. Hassoun and B. Scrosati, *Adv. Funct. Mater.*, 2013, **23**, 1076–1080.

7 N. Jiang, G. Jiang, D. Niu, J. Mao, M. Chen, K. Li and Y. Li, *J. Energy Chem.*, 2020, **51**, 207–215.

8 G. He, C. J. Hart, X. Liang, A. Garsuch and L. F. Nazar, *ACS Appl. Mater. Interfaces*, 2014, **6**, 10917–10923.

9 R. Demir-Cakan, M. Morcrette, Gangulibabu, A. Guéguen, R. Dedryvère and J. M. Tarascon, *Energy Environ. Sci.*, 2013, **6**, 176–182.

10 J. S. Yeon, S. H. Park, J. Suk, H. Lee and H. S. Park, *Chem. Eng. J.*, 2020, **382**, 122946.

YAMAGUCHI
UNIVERSITY

General conclusions

In this work, in order to improve the battery performance of LIBs, i.e., safety, controlling interfacial reaction, and capacity, we focused on adapting polyether-based materials with high electrochemical stability, sufficient mechanical strength, and flexibility to the electrolyte and the electrode. Our findings are as follows.

- The amide group, with a relatively high dielectric constant, improves the dissociability of lithium salt. We confirmed more than three orders of magnitude improvement in ionic conductivity by introducing cyanoethoxy side-chain, compared to that of PtBuOA electrolyte with a methyl side-chain.

- *Operando* ATR-IR revealed that the SEI at Cu/ PEO-LiTFSA was formed via several reduction reactions, i.e., reduction reaction of PEO, LiTFSA, and impurities. Most resistive SEI is observed at 0.8 V_{Li}, which consists of ROLi, alkyl vinyl ether, RCOOLi, LiOH, Li_2CO_3, and a small amount of LiF. Moreover, alkyl vinyl ether is further reduced to form other alkyl ether via radical propagation, which leads to relatively low SEI resistance.

- The strong interfacial attraction between sulfur and highly-conductive graphene sheets at the confined interlayer space enables rapid charge transfer and effectively inhibits the polysulfide dissolution, resulting in improved redox reaction reversibility and sulfur efficiency. More importantly, the structural flexibility of layered structure, derived from polymer-anchor, guarantees the stable cycling by accommodating the significant volume expansion of sulfur active materials.

Those knowledges will hopefully help the improvement of battery performance of lithium-ion battery and/ or future battery with polymer materials, including polyether.

Publication list

Chapter 1

Improved ionic conductivity for amide-containing electrolytes by tuning intermolecular interaction: the effect of branched side-chains with cyanoethoxy groups

Koki Yamada, Shohei Yuasa, Riho Matsuoka, Ryansu Sai, Yu Katayama and Hiromori Tsutsumi, *Physical Chemistry Chemical Physics*, **2021**, 16, 10070-10080.

Chapter 2

(Electro)Chemical Processes of Poly (Ethylene Oxide)-Based Electrolyte on Cu Surface during Lithium Secondary Battery Operation

Koki Yamada, Hiromori Tsutsumi, and Yu Katayama, *Energy Technology*

Chapter 3

Sulfur-inserted polymer-anchored edge exfoliated graphite for durable positive electrodes for lithium–sulfur batteries

Nanami Uesugi, Natsuho Kazahaya, **Koki Yamada**, Hiroshi Yoshitani, Takuya Wada, Hiroji Fukui, Shoji Nozato, Yu Katayama and Hiromori Tsutsumi, *RSC Advance*, **2021**, 29, 18093-18102.

Acknowledgements

Those studies were done during 2017−2023 at Tsutsumi laboratory, Division of Life Science, Graduate School of Sciences and Technology for Innovation, Yamaguchi University.

I wish to express my sincere gratitude to *Professor Hiromori Tsutsumi*, Graduate School of Sciences and Technology for Innovation, Yamaguchi University, my main supervisor.

I greatly appreciate *Assistant professor Yu Katayama*, SANKEN (The Institute of Scientific and Industrial Research), Osaka University, Ibaraki 567-0047 Osaka, Japan.

Thanks to all supporting me until now.

This work was supported by JST SPRING, Grant Number JPMJSP2110.

Koki Yamada

2023